New aspects of quantum light generation and propagation in quantum dots

A thesis submitted by

Samit Kumar Hazra

to

Indian Institute of Technology Guwahati

in partial fulfillment of the requirements for the degree of

Doctor of Philosophy in Physics

Under the Supervision of

Prof. Tarak Nath Dey

Department of Physics
Indian Institute of Technology Guwahati
Guwahati - 781039, Assam, India

January 6, 2025

Dedicated

to

my family

Declaration

Samit Kumar Hazra
Roll No. 176121009
Department of Physics
Indian Institute of Technology, Guwahati
Guwahati, India
E-mail: samit176121009@iitg.ac.in

I hereby declare that works presented in the thesis entitled "**New aspects of quantum light generation and propagation in quantum dots**" has been carried out by me under the supervision of Prof. Tarak Nath Dey at the Department of Physics, Indian Institute of Technology Guwahati, India. The thesis has not been submitted anywhere else for any degree. Works presented in the thesis are all my own unless referenced to the contrary in the thesis.

Date: January 6, 2025 **Samit Kumar Hazra**

Certificate

Prof. Tarak Nath Dey
Professor
Department of Physics
Indian Institute of Technology, Guwahati
Guwahati, India
E-mail: tarak.dey@iitg.ac.in

It is certified that the work contained in the thesis entitled "**New aspects of quantum light generation and propagation in quantum dots**" by Mr. Samit Kumar Hazra (Roll No - 176121009), a Ph.D. student in the Department of Physics, Indian Institute of Technology, Guwahati is carried out under my supervision and has not been submitted elsewhere for the award of any other degree.

Date: January 6, 2025 **Prof. Tarak Nath Dey**

Acknowledgements

First and foremost, I would like to convey my sincere gratitude toward my supervisor, Prof. Tarak Nath Dey, for his constant support, guidance, and advice throughout my Ph.D. journey. I am truly privileged to have him as my supervisor, as he has not only assisted me academically but also consistently kept me motivated, especially during challenging times. His suggestions on becoming a proficient speaker have always aided me in refining my presentation skills. I genuinely appreciate his understanding and patience in accommodating my limitations. With him, it has indeed been a profoundly enriching learning experience for me.

I am indebted to Dr. Pradyumna Kumar Pathak for his insightful guidance throughout my Ph.D. journey. His expertise has been invaluable in shaping my research and academic growth.

I am grateful to my doctoral committee members Prof. Amarendra Kumar Sarma, Prof. Gagan Kumar, and Prof. Aditya N. Panda, for their valuable comments and suggestions during the yearly evaluation of my research work.

I sincerely thank all academic and non-academic staff of the physics department and IIT Guwahati for their kind cooperation at all stages. I give special thanks to MHRD for financial assistance, which helped me complete my research work successfully.

I thank my collaborator and co-author, Lavakumar Addepalli, for his excellent contribution to the numerical coding required in my thesis work.

I would like to thank my group members Dr. Sandeep Sharma, Dr. Nawaz Sarif Mallick, Dr. Nilamoni Daloi, Sanket Das, Partha Das, Madan Mohan Mahana, and Gunjan Yadav for their insightful discussions on different research topics.

I am thankful to my colleagues cum friends Arghyajit Datta, Pronoy Dutta, Surojit Dalui, Riajul Haque, Nasim Ahammad Khan, Suryakanta Mishra, Tathagata Gupta, Devabrat Mahanta, Devender Kumar, Subrata Biswas, Ipsita Ray, Madhurima Chakraborty, KM Dhriti, Neda Shamin, Pragya Gupta, Prajna Paramita Mohapatra, Manisha Srivastava, Nitu, Shinjini Das for their encouragement, endless heated discussion on academic as well as nonacademic topic and entertaining company during my Ph.D. period.

I am grateful to the IITG SPIE student chapter member S. S. Goutam Buddha, Sumit Goswami, Karuna S. Malik, Nagendra Kumar, Dipti Kanika Mahato, Rajnandan C. Das, Akanshu Chauhan, Sampreet Kalita for their crucial guidance and support to enhance my leadership and teamwork capability.

My heartfelt love and appreciation to the after-dinner street walk group members Sayan Lahiri, Rakesh Sarkar, Rajesh Karmakar, Rony Boral, Swarup Kanti Sarkar, Subhrajyoti Ghosh, Soumen Kumar Manna, Amit Kumar, Avishek Sarkar, Sahabub Jahedi, Gargi Sen, Niloy Mondal, Arpita Deb Singha for making lots of fun, I doubt hardly any topic in the world left in those discussions.

I also take the opportunity to thank my hostel members, Araghni Bhattacharya, Prantik Sarmah, Subhashish Maity, and Snehasish Das, for various stimulated debates during food time.

I thank the other juniors, Jyotirmoi Borah, Gajendra Singh Bisht, Suresh Chand, Shilpi Roy, Sumit Dey, Suruj Jyoti Das, Mandira Das, Golam Masud Karim, Sujit Kumar Deb, Chinmoy Dey, Shantanu Sahoo for various exciting conversation during the Ph.D. period.

The list of acknowledgments would be incomplete without mentioning all my previous teachers, master's degree hostel friends Kartik Panda, Abhik Ghosh Moulick, Pradeepta Kumar Ghose, Arpan Chatterjee, Aniruddha Chakraborty, college friends Dipankar Sahoo, Koustav Mandal, Arnab Kanti Karan, Tanushree Basu Roy whom I am indebted.

I want to thank the late legendary Indian singer KK, who assisted me in providing mental peace during my Ph.D. time with his evergreen songs.

Finally, I wish to express my deepest gratitude to my parents, uncle, elder brother and sister-in-law for their enduring love, invaluable support, and unwavering understanding that have been pillars of strength throughout my life.

Abstract

This thesis addresses three research problems based on quantum light propagation and generation, suitable for advanced integrated photonics. We have chosen the quantum dots(QDs) as a quantum emitter platform to observe the light-matter interaction. The properties of the QD also satisfy various requirements, such as robust fabrication, tiny footprint, and low power consumption for scalable quantum photonic circuits required for quantum computation and information.

In Chapter 1, we present the basic theories, elementary concepts, and fundamental definitions of various topics required for the thesis work. We start with the classical and quantum descriptions of the electromagnetic radiation. Then, we discuss the concept of artificial atoms and quantum dots and their quantized energy levels, which are similar to those of atoms. The radiation-matter and electron-phonon interaction Hamiltonian is derived from the fundamental principle. To study any interacting quantum systems, the density matrix formalism is introduced and discussed for a two-level system. We also describe the pulse propagation equation inside a medium derived from the Maxwell equations. Further, we thoroughly analyze the four-wave mixing process and associated nonlinear optical effects. Additionally, we display the definition of the vector beams in terms of Laguerre-Gaussian(LG) modes. After that, the full quantum theory of radiation-matter interaction describes the quantum theory of laser and rate equation. Finally, we introduce the concept of quantum entanglement and the Duan-Giedke-Cirac-Zoller (DGCZ) criterion.

In Chapter 2, we demonstrate the self-induced transparency (SIT) in an inhomogeneously broadened semiconductor QD medium at ultra-low temperatures. In the SIT process, an optical pulse can propagate through the two-level absorbing medium without experiencing any deformation in its pulse shape. Selecting the high biexciton binding energy, we make an effective two-level QD system with additional phonon interaction corresponding to the crystal vibration. Our calculation relies on the recently developed Polaron master equation, which includes all orders of phonon interaction. We search for suitable input pulse parameters by analyzing the phonon-induced decay rates, temperature-dependent pulse area, excited state population, and medium susceptibility. We discuss the SIT process by observing the spatiotemporal variation of the input pulse in terms of peak intensity and broadening. We illustrate the effect of various system and bath parameters on the SIT dynamics, such as inhomogenous broadening, environment temperature, and electron-phonon coupling strength. We also examine the higher input pulse area and pulse breakup phenomena in this scheme.

In Chapter 3, we propose a simple model for arbitrary vector beam (VB) generation in a thin QD medium. The medium has four energy levels in a diamond configuration with alternating left and right circularly polarized transitions. We apply a weak probe field and two relatively strong control orbital angular momentum (OAM) carrying fields to the three consecutive transitions started with left circular polarisation. In this scenario, a four-wave mixing (FWM) field generation is possible with transferred OAM in the presence of the medium's third-order nonlinearity. We study the applied probe field and generated field intensity along the propagation length. A comparison of these two orthogonally polarised components reveals the suitable propagation distance

for lemon vector beam generation. Next, we discuss the various full Poincare and cylindrical VB generations by plotting the intensity and polarisation in a transverse plane with the help of Stokes parameters. During the VB generation process, we show the additional polarisation rotation control as a function of the relative control field phase. In the end, we explore the effect of phonon bath temperatures on the VB generation process.

In Chapter 4, we address the feasibility of nondegenerate two-photon lasing and two-mode entanglement in a single QD placed inside a two-mode microcavity. The two cavity modes are coupled to the vertically polarised transitions from biexciton to ground states. Subsequently, the other two horizontally polarised transitions from the ground state to the biexciton state are considered for optical pumping to achieve population inversion in the system. We inspect the results regarding the QD population and cavity parameters for incoherent and coherent pumping. For incoherent pumping, we display the variation of the earlier-mentioned parameters as a function of both detuning and pumping rates. We compare single- and two-photon emission rates for two different temperatures. We follow a similar analysis except for the pumping rate variation for coherent pumping. To explain the coherent pumping result, we introduce the dressed state analysis for coherent light-matter interaction. We also mentioned the possibility of two-mode entanglement generation under two-photon pumping conditions. We find a specific parameter range for nondegenerate two-photon lasing and two-mode entanglements.

In Chapter 5, we make an overall conclusion of the whole thesis. Then, we also mentioned some of our unfinished ongoing work and potential future plans.

Publications included in this thesis :

- **Samit Kumar Hazra**, P. K. Pathak, and Tarak Nath Dey, "Self-induced transparency in a semiconductor quantum dot medium at ultracold temperatures," Phys. Rev. B **107**, 235409 (2023).
- **Samit Kumar Hazra**, P. K. Pathak, and Tarak Nath Dey, "Arbitrary vector beam generation in semiconductor quantum dots," arXiv:2407.05756 [quant-ph]. (**Accepted in PRB**)
- **Samit Kumar Hazra**, Lavakumar Addepalli, P. K. Pathak, and Tarak Nath Dey, "Nondegenerate two-photon lasing in a single quantum dot," Phys. Rev. B **109**, 155428 (2024).

School/Conference/Workshop attended :

- SERB school on frontiers in quantum optics, IIT Guwahati, India, 01-19 December 2017.
- IEEE Workshop on recent advances in photonics, IIT Guwahati, India, 13-14 December 2019.
- Summer School on Quantum Information and Quantum Technologies, IISER Kolkata, India, 01 June-05 July 2022.
- Raman Conference on Light and Matter Physics, RRI, India, 14-18 August 2023.
- Frontiers in Optics + Laser Science, Colorado Convention Center, Denver, Colorado, USA, 23-26 September 2024.

Contents

List of Figures

Chapter 1

Introduction

Light has been wondering humanity from ancient to modern times. Various natural optical phenomena attract ancient philosophers, artists, mathematicians, and astronomers such as Euclid, Ptolemy, Ibn Sahl, and Ibn al-Haytham. Their contribution leads to a better understanding of light's reflection, refraction, and transmission with other optical elements such as curved mirrors and lenses[1, 2]. In early modern times, Kepler discovered the presence of atmospheric refraction during the study of both lunar and solar eclipses[3]. Later, Willebrord Snellius found the mathematical construction of the refraction of light, popularly known as Snell's Law[4]. Christiaan Huygens first introduced the wave theory of light to understand the rectilinear propagation of light and diffraction [5]. In the meantime, Newton demonstrated that a prism could decompose white light into a broad spectrum of colors[6]. He also designed the Newton ring experiment to produce a superior dispersionless telescope. Subsequently, he pioneered predicting the corpuscular nature of the light [6]. Thomas Young has carried out further development by introducing his double slit experiment to observe the interference effect between two closely spaced secondary light sources [7]. Fraunhofer and Fresnel carried out the concrete study and mathematical formalism of diffraction [8, 9]. In the nineteenth century, Maxwell combined four different electric and magnetic equations to describe the properties of light, named Maxwell's equations [10]. Maxwell's equation explains all the previously mentioned phenomena of light and, in general, electromagnetic radiation. A few decades later, Max Planck introduced the concept of quantized light or photon to explain blackbody radiation [11]. This foundation leads to the beginning of modern quantum optics. In the twentieth century, Albert Einstein used the concept of photons to explain the photoelectric effect and was awarded the Nobel Prize in physics [12]. Willis Lamb adopted the new quantum treatment of light and explained the radiative level shifts of atoms, commonly known as Lamb shifts [13]. Weisskopf and Wigner predicted the exponential decay of the excited state by analyzing the spontaneous emission and resonance fluorescence under the quantum theory of light [14]. Optical coherence has been investigated in the context of stellar interferometry by Hanbury Brown and Twiss [15, 16]. This experiment led to the definition of first- and second-order correlation functions and various photon statistics. The invention of the maser and laser provide a major breakthrough in the field of optics [17, 18]. The quantum theory of laser was also developed under cavity quantum electrodynamics [19].

In quantum optics, we mainly study the radiation-matter interaction. The matter

always has discreet quantized energy levels. Depending on the classical or quantum description of radiation, the analysis of the mentioned interaction is called "semiclassical" or "fully quantum" theory. The semiclassical theory is mostly used to describe the medium's optical properties. At the same time, full quantum theory is beneficial in investigating photon statistics, quantum correlation, and laser. The simplest radiation-matter interaction model is a two-level atom interacting with the continuous wave(CW) laser field. Such a system shows significant light absorption in the medium under resonance conditions. McCall and Hahn discovered that an optical pulse can propagate through the medium without changing intensity or shape at resonance conditions. This phenomenon is popularly known as self-induced transparency (SIT) [20, 21]. Motivated by this work, we study SIT behavior in the quantum dot medium, which offers an excellent advantage for making a quantum communication channel. The system becomes more interesting when a three-level system interacts with two light fields. In this consideration, lambda (Λ), vee(V), and cascade (Ξ) are the three main studied configurations. They exhibit several new quantum phenomena, such as electromagnetically induced transparency (EIT) [22], coherent population trapping (CPT) [23], lasing without inversion (LWI) [24], slow light [25], storage and retrival of a light pulse [26]. In the EIT process, the medium becomes transparent for a weak probe field by manipulating the medium susceptibility property depending on the control field parameters. Including more energy levels in the system offers higher-order nonlinear susceptibility in the medium. This consideration opens up the scope for multiple optical field matter interactions and nonlinear optics. Among all the multilevel systems, N-type, diamond, and tripod configurations are the some widely used four-level systems considered for light-matter interaction. These four-level systems provide various new possibilities by playing with the multiple interacting electric field parameters. Some of the prominently observed nonlinear optical processes are the new harmonic generation [27], optical parametric amplification (OPA) [28], parametric down-conversion (PDC) [29], four-wave mixing (FWM) [30], self-phase modulation (SPM) [31], and self-focusing [32]. Motivated by the FWM process in a four-level diamond system, we have investigated the arbitrary vector beam generation in a QD. The vector beams are generated by the vector superposition of two orthogonally polarised Laguerre-Gaussian modes. These modes are the solution of the paraxial wave equation and can carry orbital angular momentum (OAM). Quantum light generation always requires light-matter interaction in a closed environment, such as an optical cavity resonator. Various low-mode volume and high-quality cavities such as toroidal, micropillar, and photonic crystal cavities have been fabricated recently with advanced nanotechnology. The efficient fabrication of artificial atoms also gained research interest for scalable quantum emitters. Motivated by these findings, we have investigated the feasibility of a nondegenerate two-photon laser in a single QD-cavity system. Such lasers have tiny footprints and ultralow threshold power, which is suitable for future quantum photonic circuits.

Outline of the thesis

In this thesis, we have investigated optical pulse propagation and various quantum light generations in a QD medium. The thesis consists of five chapters.

In Chapter 1, we have presented the introduction of our final research work. This chapter consists of the preliminary topic, definition, and basic theory. We started with

the classical and quantum theory of EM-field. Then, we introduce the concept of artificial atom, more precisely, quantum dot. Subsequently, we derived the mathematical form of the radiation-matter and the electron-phonon interaction. Further, we have studied the density matrix formalism to find the dynamics of a two-level quantum system. We have also understood the light pulse propagation in a medium. Furthermore, we have investigated the origin of four-wave mixing in a nonlinear medium. After that, we defined the vector beam by using Laguerre-Gaussian modes. Finally, we will mention the quantum theory of laser and quantum entanglement.

In Chapter 2, we will study the self-induced transparency in a quantum dot medium at ultracold temperatures. We started with a brief introduction showcasing the literature survey and existing work on SIT. Next, we will establish the problem under the phonon environment and discuss it in the model system section. In the result section, we analyzed the various phonon-induced scattering rates and the pulse area theorem. Further, we explored the SIT phenomena thoroughly by observing the effect of phonon bath parameters and environmental temperature. Finally, we make a conclusion at the end of the chapter.

In Chapter 3, we proposed a scheme for arbitrary vector beam generation in a thin disc shape QD medium. We start with the background theory of the vector beam and introduce some relevant published work. Then, we describe the model system of a four-level QD system interacting with the three OAM-carrying optical fields. Later, we displayed the intensities and polarisation of six different vector beams in a transverse plane. Additionally, we show that the generated vector beam polarisation rotation depends on the control field relative phase. We also discussed the effect of temperature on VB generation. Finally, we conclude the work.

In Chapter 4, we inspect the feasibility of nondegenerate two-photon laser and two-mode entanglement in a single QD-cavity system. First, we mention the earlier development of the microlaser papers in the introduction. After that, we specify the model of a four-level QD embedded inside the two-mode microcavity. Then, we make a detailed analysis of both incoherent and coherent pumping mechanisms for two-photon laser generation. Additionally, we have discussed the two-mode entanglement generation in a specific pumping condition. Finally, we concluded this work's outcome.

In Chapter 5, we delineated the conclusion of the thesis. We will also discuss some of the incompleted problems and their difficulty. We would like to express some views on the possible extensions of our work. Finally, we describe the future plans.

1.1 Fundamentals of electromagnetic radiation

This section presents the fundamental theory for classical and quantum description of electromagnetic(EM) radiation. The classical EM radiation theory started with Maxwell's equation in free space [10]. Solving these four equations, we reach a general mathematical form of the EM radiation with all the characteristic parameters. After that, we discuss the EM radiation with periodic boundary conditions, which leads to quantization. Here, we mainly focus on the quantized EM radiation inside an optical cavity resonator.

1.1.1 Classical description of electromagnetic radiation

The four fundamental Maxwell's equations can fully describe all the classical phenomena of EM radiation [10, 33]. Therefore, we write down the Maxwell's equations in SI unit as

$$\vec{\nabla} \cdot \vec{D} = \rho, \qquad \text{(Gauss's Law)} \tag{1.1}$$

$$\vec{\nabla} \cdot \vec{B} = 0, \tag{1.2}$$

$$\vec{\nabla} \times \vec{E} = -\frac{\partial \vec{B}}{\partial t}, \qquad \text{(Faraday's Law)} \tag{1.3}$$

$$\vec{\nabla} \times \vec{H} = \vec{J} + \frac{\partial \vec{D}}{\partial t}, \qquad \text{(Ampere's Law)} \tag{1.4}$$

where $\vec{E}$ and $\vec{H}$ represent the electric and magnetic field at some space-time coordinate ($\vec{r}$, t). The right-hand side source terms ρ, $\vec{J}$ stand for the free charge density and current density, respectively. Other induced quantity electric displacement $\vec{D}$ and magnetic induction $\vec{B}$ depends on the fields given by

$$\vec{D} = \epsilon_0 \vec{E} + \vec{P} \tag{1.5}$$

$$\vec{B} = \mu_0(\vec{H} + \vec{M}) \tag{1.6}$$

where $\vec{P}$ and $\vec{M}$ are the electric and magnetic polarization inside the medium. The free space permeability and permittivity are also denoted by ϵ_0, μ_0 respectively. In this subsection, we only study the behavior of the EM radiation in a free space. Therefore, all the source terms, free charge ρ, and current $\vec{J}$ in equations are zero. Subsequently, free space does not carry any electric ($\vec{P}$) or magnetic ($\vec{M}$) polarisation due to the nonconducting and non-magnetic properties. Thus, Maxwell's equation in free space is written as

$$\vec{\nabla} \cdot \vec{E} = 0, \tag{1.7}$$

$$\vec{\nabla} \cdot \vec{B} = 0, \tag{1.8}$$

$$\vec{\nabla} \times \vec{E} = -\frac{\partial \vec{B}}{\partial t}, \tag{1.9}$$

$$\vec{\nabla} \times \vec{B} = \frac{1}{c^2}\frac{\partial \vec{E}}{\partial t}, \tag{1.10}$$

where we have used the identity $\vec{D} = \epsilon_0 \vec{E}$, $\vec{B} = \mu_0 \vec{H}$, $\mu_0 \epsilon_0 = 1/c^2$ and c is the speed of light in free space. For the first time, we notice that the Maxwell equations express the connection with the light exhibiting the physical constant c. To understand this connection in more detail, we take the curl of Eq. 1.9 and use Eq. 1.10 given below:

$$\vec{\nabla} \times \left(\vec{\nabla} \times \vec{E}\right) = -\frac{\partial}{\partial t}(\nabla \times \vec{B}), \tag{1.11}$$

$$\vec{\nabla} \times \left(\vec{\nabla} \times \vec{E}\right) = -\frac{1}{c^2}\frac{\partial^2 \vec{E}}{\partial t^2}. \tag{1.12}$$

Now, using vector field identity $\vec{\nabla} \times \left(\vec{\nabla} \times \vec{E}\right) = \vec{\nabla}\left(\vec{\nabla} \cdot \vec{E}\right) - \nabla^2 \vec{E}$ in the previous equation we obtain

$$\nabla^2 \vec{E} - \frac{1}{c^2}\frac{\partial^2 \vec{E}}{\partial t^2} = 0. \tag{1.13}$$

The structure of the above equation looks like a well-known wave equation. Therefore, the general solution of this kind of equation traveling along the z direction takes the form

$$\vec{E}(z,t) = \vec{E}_1(z - ct) + \vec{E}_2(z + ct), \tag{1.14}$$

where $\vec{E}_1$ and $\vec{E}_2$ are arbitrary functions. These electric field components $\vec{E}_1$, $\vec{E}_2$ represent the wave traveling along positive and negative directions with the speed of light. We consider an electromagnetic plane wave solution, with polarization along the $\hat{x}$ having frequency ω and wave vector $\vec{k} = k\hat{z}$. These parameters satisfy the condition $\omega/k = c$. The general form of the electric field for an EM-wave can be described by

$$\vec{E}(z,t) = \hat{x}\mathcal{E}_0(z,t)e^{i(kz-\omega t)} + c.c. \tag{1.15}$$

By using the Maxwell's equation, we find the expression for the magnetic field given by

$$\vec{B}(z,t) = \frac{k}{w}(\hat{z} \times \vec{E}(z,t)) \tag{1.16}$$

$$\vec{B}(z,t) = \frac{k}{w}(\hat{z} \times \hat{x})\mathcal{E}_0(z,t)e^{i(kz-\omega t)} + c.c. \tag{1.17}$$

$$\vec{B}(z,t) = \hat{y}\mathcal{B}_0(z,t)e^{i(kz-\omega t)} + c.c. \tag{1.18}$$

Now, it is clear from this study that the electric field, magnetic field, and propagation vector are perpendicular to each other. We have demonstrated the traveling EM wave in free space in Fig. 1.1. An EM wave's electric and magnetic fields oscillate in space

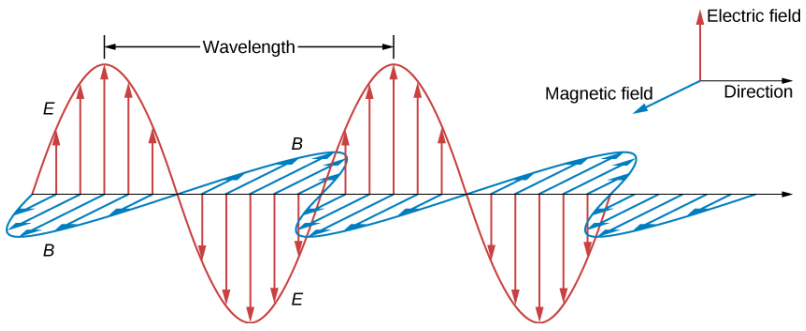

Figure 1.1: The figure illustrates a classical description of the EM wave propagation in free space [34].

and time. The closest distance between two peak intensities of the electric or magnetic field is known as the wavelength. The visible light is an EM wave with a narrow wavelength range from 400 - 700 nm. However, the EM wave theory applies to any wavelength range, including visible light. In this analysis, we understand the various important parameters of light, such as amplitude $\mathcal{E}_0$, frequency ω, wavelength λ, wave

number k, and polarization. The EM theory explains all the classical phenomena of light, such as reflection, refraction, and transmission, which we will not discuss here. Interested readers can find the complete theory in any standard electrodynamics book. The classical Hamiltonian of the EM field in free space is

$$H = \int_V \left(\frac{1}{2}\epsilon_0 E^2 + \frac{1}{\mu_0} B^2 \right) dV \tag{1.19}$$

where V is the enclosed volume. Alternatively, this Hamiltonian represents the total energy of the EM radiation inside the specified volume.

1.1.2 Quantum description of electromagnetic radiation

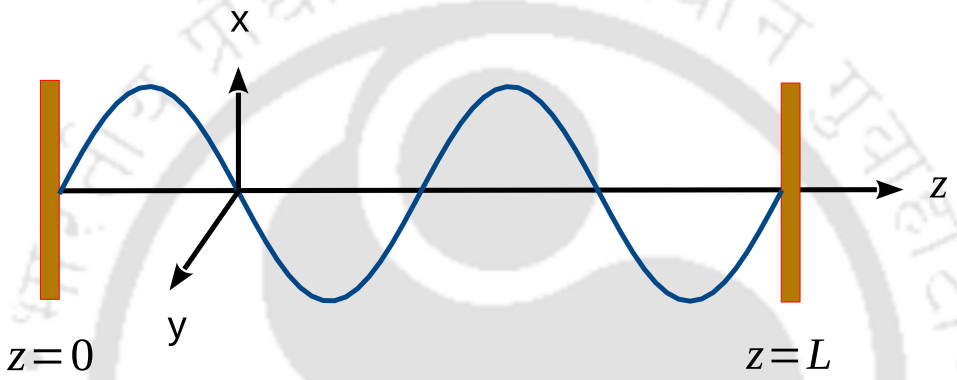

Figure 1.2: Schematic diagram of a one-dimensional cavity resonator made of two plane mirrors having length L. The electric field polarisation is assumed to be in the x-direction.

In this subsection, we started with a simple one-dimensional cavity resonator along the z-axis with two perfectly reflecting mirrors placed at $z = 0$ and $z = \mathrm{L}$, as shown in Fig. 1.2 [35, 36]. For both ends of the cavity, the electric field will vanish because of the mirrors and form a standing wave inside the cavity. We assume there are no sources of charge or current inside the cavity. As mentioned in the previous subsection, the EM wave's electric field is considered linearly polarised in the x-direction. The boundary condition of the cavity leads to an infinite number of normal mode solutions with amplitude q_j, frequency $\omega_j = j\pi c/L$ and wave vector $k = j\pi/L$ where j = 1,2,... In analogy with the harmonic oscillator, the electric field of the single mode cavity in terms of normal mode can be written as

$$E_x(z,t) = \left(\frac{2\omega^2 m}{V\epsilon_0} \right)^{1/2} q(t)\sin(kz), \tag{1.20}$$

where m is the mass of the oscillator, and V is the effective volume of the cavity. We also find the expression for the magnetic field by using the Maxwell equation as

$$B_y(z,t) = \left(\frac{\mu_0\epsilon_0}{k} \right) \left(\frac{2\omega^2 m}{V\epsilon_0} \right)^{1/2} \dot{q}(t)\cos(kz). \tag{1.21}$$

These two expressions show that $q(t)$ and $p(t) = m\dot{q}(t)$ act as a canonical position and momentum present in the electric and magnetic fields, respectively. Now, we recall

the classical Hamiltonian in Eq. 1.19 and put these fields together to find

$$H = \int_V \left(\frac{1}{2}\epsilon_0 E_x^2 + \frac{1}{\mu_0} B_y^2\right) dV \tag{1.22}$$

$$H = \frac{1}{2}\left(\frac{p^2}{m} + m\omega^2 q^2\right). \tag{1.23}$$

In the case of a harmonic oscillator system, the canonical variable pair and the Poisson bracket should be replaced by the two operators and the commutator bracket to quantize the system. Following this method, we introduce the position and momentum operators as $\hat{q}$ and $\hat{p}$ satisfying the relation $[\hat{q}, \hat{p}] = i\hbar$. To make the final Hamiltonian more compact, traditionally, a pair of conjugate operators named annihilation (a) and creation ($a^\dagger$) has been introduced. These new operators can be expressed in terms of the canonical operator pair as [35, 36]

$$a = \frac{1}{\sqrt{2m\hbar\omega}}(m\omega\hat{q} + i\hat{p}) \tag{1.24}$$

$$a^\dagger = \frac{1}{\sqrt{2m\hbar\omega}}(m\omega\hat{q} - i\hat{p}). \tag{1.25}$$

Using Eq. 1.24−1.25, we find the expression for the electric and magnetic field operator in terms of a and $a^\dagger$, which are

$$\hat{E}_x(z,t) = \mathcal{E}_0(a + a^\dagger)\sin(kz) \tag{1.26}$$

$$\hat{B}_y(z,t) = -i\mathcal{B}_0(a - a^\dagger)\cos(kz) \tag{1.27}$$

where $\mathcal{E}_0 = (\hbar\omega/\epsilon_0 V)^{1/2}$ and $\mathcal{B}_0 = (1/c)(\hbar\omega/\epsilon_0 V)^{1/2}$. The relation between annihilation and creation operator satisfies the commutation relation as follows

$$[a, a^\dagger] = 1. \tag{1.28}$$

Therefore, the Hamiltonian of the quantized EM radiation in operator form

$$H = \hbar\omega\left(a^\dagger a + \frac{1}{2}\right). \tag{1.29}$$

In general, the electric and magnetic field inside a three-dimensional cavity with many modes is described by

$$\hat{\vec{E}}(\vec{r}, t) = \sum_k \hat{\epsilon}_k \mathcal{E}_k a_k e^{i(\vec{k}\cdot\vec{r} - \omega_k t)} + H.c., \tag{1.30}$$

$$\hat{\vec{B}}(\vec{r}, t) = \sum_k \left(\frac{\vec{k} \times \hat{\epsilon}_k}{\omega_k}\right) \mathcal{E}_k a_k e^{i(\vec{k}\cdot\vec{r} - \omega_k t)} + H.c. \tag{1.31}$$

In this case, the free Hamiltonian of the quantized EM radiation by including the sum over all cavity modes given below

$$H = \hbar \sum_k \omega_k \left(a_k^\dagger a_k + \frac{1}{2}\right). \tag{1.32}$$

1.2 Quantum theory of matter

In the macroscopic world, Newton's law of motion completely describes the dynamics of a particle. It raises concerns in the physics community whether this theory can apply to a microscopic particle's dynamics. By reducing the size of a particle, we reach the fundamental unit of matter, which has all the characteristics called an atom. Several natural phenomena with the atom have been observed that could not be explained by Newton's Law. A giant leap takes place in the quantum theory of matter when De Broglie first introduces the concept of the wave nature of matter [37] concerning the known wave-particle duality of light. Bohr predicted the correct continuous orbit of an electron in an atom, which produces discreet energy levels [38]. Subsequently, the Bohr- Sommerfeld model best describes the electronic energy levels of the atoms [39]. In the meantime, Heisenberg introduced his famous uncertainty principle, where the measurement of two canonical observables with complete accuracy is prohibited in the quantum theory [40]. With all the development, Schrödinger published his renowned equation to find the dynamics of a quantum particle and give birth to quantum mechanics [41]. In a microscopic system, the Schrödinger equation describes the dynamics of a quantum particle, similar to Newton's law in classical mechanics. Dirac introduces relativity in quantum mechanics to find the more general relativistic quantum theory for the dynamics of electrons [42]. Max Born discovered the intrinsic probabilistic nature of quantum mechanics [43]. He also introduced the probability density function and, then, with Heisenberg, developed the matrix formalism of quantum mechanics [44]. This section discusses the Bohr-Sommerfeld model of quantized energy levels of atoms. Then, we discuss the preliminary theory of artificial atoms and their classification. Finally, we explore the characteristics of the quantum dots(QDs) in detail.

1.2.1 Atom

The fundamental unit of matter which decides the bulk chemical and physical properties is known as the atom. Generally, an atom consists of a nucleus of protons and neutrons surrounded by many orbiting electrons. To study the atomic structure, we consider the simplest possible atom with one proton and one electron, which is referred to as a hydrogen atom. Before the discovery of quantum mechanics, Rydberg and Balmer find an empirical formula for the visible spectral lines of the hydrogen atom by investigating atomic spectra [45]. However, no one understood the reason for the presence of such specific spectral lines at that time. To understand the discreet energy level of the hydrogen atom in more detail, we apply the quantum mechanical approach [46, 47]. An electron inside the atom is bound to the nucleus by the electromagnetic interaction. Therefore, the potential energy of the electron with charge e in the center of mass coordinate is given by

$$V = -\frac{e^2}{4\pi\epsilon_0 r} \tag{1.33}$$

where r is the amplitude of the radial vector in spherical polar coordinates. In the center of the mass frame, the mass of proton m_p and mass of electron m_e can transformed into a reduced mass $\mu = m_e m_p/(m_e + m_p) \approx m_e$ as $m_p \gg m_e$. The Hamiltonian of a

hydrogen atom at rest can be written as

$$H = \frac{p^2}{2\mu} - \frac{e^2}{4\pi\epsilon_0 r} = -\frac{\hbar^2}{2\mu}\nabla^2 - \frac{e^2}{4\pi\epsilon_0 r}. \tag{1.34}$$

The Schrödinger equation for the hydrogen wavefunction $\Psi(\vec{r}, t)$ can be written as

$$H\Psi(\vec{r}, t) = i\hbar\frac{\partial\Psi(\vec{r}, t)}{\partial t}. \tag{1.35}$$

After separating the temporal part from the total wavefunction, we get

$$H\psi(\vec{r}) = E\psi(\vec{r}). \tag{1.36}$$

where E is the eigenenergy of the wave function. We solve Eq. 1.36 in the spherical polar coordinate in order to get the eigenfunction with the corresponding eigenenergy as

$$\psi_{n\ell m}(r, \theta, \varphi) = \sqrt{\left(\frac{2}{na_0^*}\right)^3 \frac{(n-\ell-1)!}{2n(n+\ell)!}} e^{-\rho/2}\rho^\ell L_{n-\ell-1}^{2\ell+1}(\rho) Y_\ell^m(\theta, \varphi) \tag{1.37}$$

$$E_n = -\frac{\mu}{2}\left(\frac{e^2}{4\pi\varepsilon_0\hbar}\right)^2 \frac{1}{n^2} \tag{1.38}$$

where $\rho = 2r/na_0^*$, reduced Bohr radius $a_0^* = \frac{4\pi\varepsilon_0\hbar^2}{\mu e^2}$, generalised Laguerre polynomial $L_{n-\ell-1}^{2\ell+1}(\rho)$ and spherical harmonic function $Y_\ell^m(\theta, \varphi)$. We observed that the wavefunction depends on the three integer numbers, denominated as the principal quantum number n, the azimuthal quantum number ℓ, and magnetic quantum number m. The system's energy depends only on the principal quantum number n with an integer value. According to quantum mechanics, if a particle is confined in a tiny region of space, then the particle's energy gets quantized. In this case, potential energy bound the electron in a Bohr radius $a_0 = \frac{4\pi\varepsilon_0\hbar^2}{m_e e^2} = 0.5$ Å, which is responsible for these discrete energy levels. In earlier calculations with infinite nucleus mass, Rydberg energy (Ry) for the hydrogen atom was 13.6 eV. Thus, the hydrogen atom energy in terms of the Rydberg energy has this form

$$E_n = -Ry\frac{1}{n^2} = -\frac{13.6\,eV}{n^2}. \tag{1.39}$$

According to the Bohr model, the electron revolves in certain stable orbits around the nucleus without radiating any energy. It can only gain or lose energy by jumping from one allowed orbit to another, absorbing or emitting electromagnetic radiation [38]. The energy difference between the initial and final level determines the absorbed or emitted photon frequency, following the relation $h\nu = E_2 - E_1$. The Rydberg formula best estimates the emitted photon wavelength

$$\frac{1}{\lambda} = R_{\mathrm{H}}\left(\frac{1}{n_1^2} - \frac{1}{n_2^2}\right), \tag{1.40}$$

where R_H is the Rydberg constant and n_1, n_2 are principal quantum numbers of lower, higher energy levels. In Fig. 1.3, we have displayed the various energy levels of the hydrogen atom. Looking at the figure, it is clear that increasing the value of n results

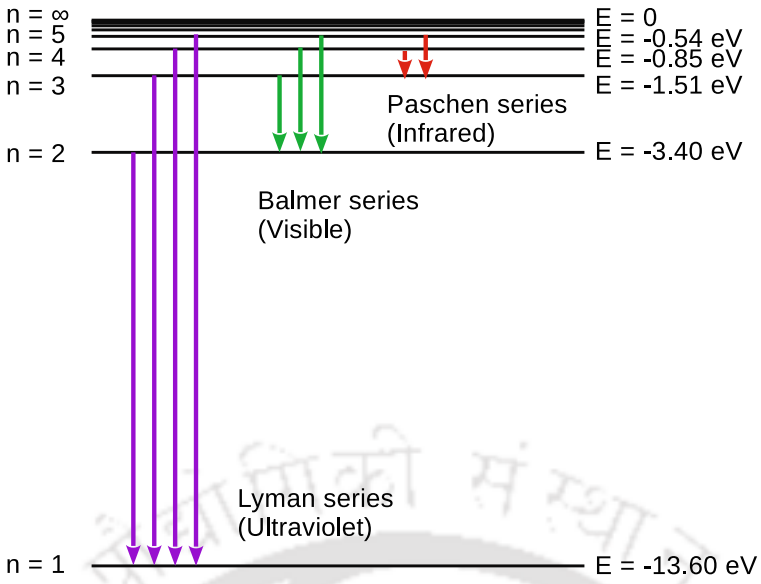

Figure 1.3: Energy level diagram for the hydrogen atom with their corresponding transitions.

in a smaller energy difference, and for $n \to \infty$, the electron energy approaches zero. This zero energy indicates that the atom can no longer bind the electron. Therefore, the electron moves freely, which turns the atom into an ion. All the excited state electron transitions to a lower energy level produce a series of spectral lines. Some of the series are Lyman ($n = 1$), Balmer ($n = 2$), and Paschen ($n = 3$), with the wavelength range in the ultraviolet, visible, and infrared regions, respectively. Though this model successfully shows the atom's quantized energy level, applying the magnetic field can split these energy levels into more sublevels due to the Zeeman effect. A convenient method of spectroscopic notation has been invented to identify all these hyperfine states. In modern times, those spectroscopic notations are widely used to specify an atomic energy level. The exploration of the quantized matter started with a hydrogen atom. Later, the interest shifted to the low-mass alkali atoms like lithium (Li), sodium(Na), and Potassium(K). Currently, researchers are working on heavy-mass alkali atoms, such as Rubidium (Rb) and Caesium(Cs).

1.2.2 Artificial Atom

In the previous subsection, we understand the formation of the discrete energy levels in an atom. These atoms can come together to form a molecule. According to the molecular orbital theory, the individual energy levels of atoms overlap to form closely spaced hybrid energy levels [48]. Furthermore, a collection of atoms or molecules produces the bulk matter with continuous energy bands separated by the forbidden energy(band gap). Depending on the forbidden energy, the matter is classified into three categories. These are metals, semiconductors, and insulators with band gap energy zero, moderate, and practically infinite, respectively. Bulk matter can exist in gaseous, liquid, and solid forms. The periodic arrangements of atoms or molecules are responsible for crystal structure formation in a solid. This subsection only discusses solid-state semiconductor crystal nanostructures and their properties. The term nanostructure refers to any material with a nanometer dimension. Starting with the bulk matter, one can reduce the length of one particular dimension to a nanometer scale known as con-

finement. A low-bandgap semiconductor nanostructure placed inside a high-bandgap host material can produce such electronic confinement. This confinement effect determines the properties of a nanostructure because of the modified degrees of freedom of the carrier. Generally, any material structure confined in one or more dimensions produces a discretized energy level called an artificial atom. The artificial atoms are made of semiconductor materials with confinement in one, two, or three dimensions, making them 2D, 1D, and 0D objects, denoted as the quantum well (QW), quantum wire (QWR), and quantum dots (QDs), respectively [49]. The confinement effect on the system energy is best described by the density of state (DOS), defined as

$$\rho(E) = \frac{\partial N}{\partial E}, \tag{1.41}$$

where N is the total number of states per unit volume, and E is the energy. The expression of the DOS in various dimensions calculated from the previous formula is given by

$$\rho_{3D}(E) = \frac{1}{\pi^2}\left(\frac{m^*}{\hbar^2}\right)^{3/2}\sqrt{2E}, \tag{1.42}$$

$$\rho_{2D}(E) = \frac{m^*}{\pi\hbar^2}\sum_{n_x}\Theta(E - E_{n_x}), \tag{1.43}$$

$$\rho_{1D}(E) = \frac{1}{\pi\hbar}\sqrt{2m^*}\sum_{n_x,n_y}\Theta(E - E_{n_x,n_y})^{-1/2}, \tag{1.44}$$

$$\rho_{0D}(E) = 2\sum_{n_x,n_y,n_z}\delta(E - E_{n_x,n_y,n_z}), \tag{1.45}$$

where m^* is the effective mass, $\Theta(E)$ is the step function, E is the energy of the particular state, E_{n_i} with $i = x, y, z$ is the quantized energy of the particular confinement direction.

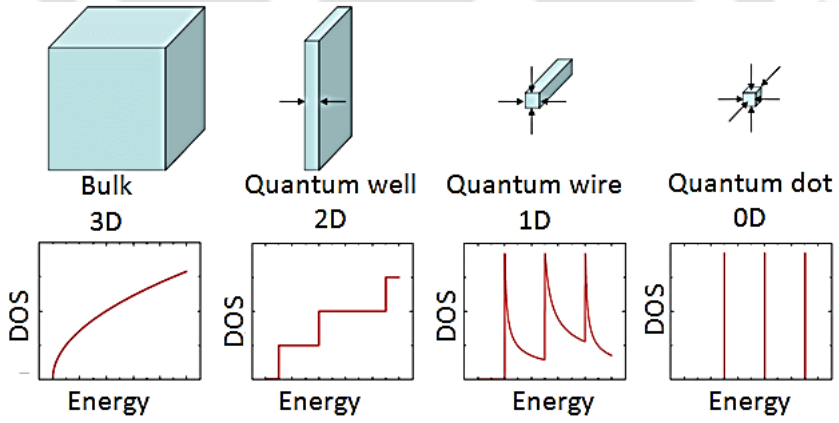

Figure 1.4: The figure displayed the density of state variation with energy and nanostructure dimensions for various artificial atoms [50].

In Fig. 1.4, we have depicted the variation of DOS with the system energy for various artificial atom nanostructures. We observed that balk material produces a continuous energy distribution. However, a quantum well with confinement in one dimension shows step function behavior. Subsequently, a quantum wire with confinement in two dimensions provides a spike-like distribution with a broader tail. Finally,

quantum dots with confinement in all three dimensions produce a delta function-like distribution similar to the discrete atomic energy levels. Among all other structures, we mainly focus on quantum dots due to their well-separated quantized energy levels.

1.2.3 Quantum Dot

The quantum dot is a few nanometer semiconductor heterostructures made of several atoms that show discrete energy levels like atoms due to the strong carrier confinements. Modern and advanced impurity-free fabrication technology is required to build such a nanoscale object [51]. Although older-generation fabrication technology lacks the requirements to make a practical integrated photonic circuit, thanks to the rapidly growing current nanotechnology for making it possible. According to the properties and preparation techniques, the QDs are mainly classified into the following three types: (i) self-assembled quantum dots [52], (ii) nanocrystals or colloidal quantum dots [53], and (iii) electrically defined quantum dots [54]. Among these three types of QDs, the self-assembled QDs are suitable candidates for strong light-matter interaction and semiconductor fabrication [55]. Therefore, we will discuss the properties of self-assembled QDs here. Various modern techniques are applied to generate high-quality QDs in the laboratory. The most common techniques are crystal-growth procedures, epitaxial methods, electron-beam lithography, etching, and deposition. In this thesis, our investigation of the QDs is limited to the family of InGaAs/GaAs under the group III-V semiconductors. One of the best methods for generating InGaAs quantum dots is the Stranski-Krastanov method [56]. In this method, a thin layer of InGaAs is deposited on top of the host GaAs matrix with a 7% larger lattice constant of InGaAs compared to that of GaAs. Due to the lattice parameter mismatch, the strain relaxation process produces self-assembled nucleation of quantum dots in the form of randomly positioned islands. Another emerging growth technique, the droplet epitaxy, relies on the saturation of gallium droplets with arsenic, resulting in relatively large and low-density GaAs quantum dots in AlGaAs [57]. For both cases, a substrate capping layer is grown atop the QDs to prevent all kinds of damage.

Now, we will study the energy level configuration of a QD and various possible transitions among them [58]. Like an atom, one electron from the valance band can jump to the conduction band by absorbing the bandgap energy in a QD. In a semiconductor, the valance band is normally filled with electrons; hence, this jump creates a hole inside the valance band. This correlated electron-hole pair forms a bound state via direct or exchange Coulomb interactions to create fundamental optical excitation called exciton. Generally, the QD with an aspect ratio larger than unity lifts the valance band degeneracy: the heavy-hole and light-hole bands. Neglecting the light-hole band is often a good approximation for the nearly spherical QD to access the lowest energy level in the valance band. Further, the crystal growth direction, strain, and annealing also play an essential role in the energy level structure. After taking some practical approximations, the researchers observed that a simple two-band effective mass model could describe QD dynamics very well. We will stick with this model for the entire thesis. We also work on a QD size with larger energy-level spacing than the Coulomb energy. This consideration ensures that the motion of the carriers in the valance and conduction bands are independent, also known as a strong confinement regime. To determine the interaction strength between light and QD energy levels, it is necessary to compute the transition matrix elements expressed in transition dipole moments.

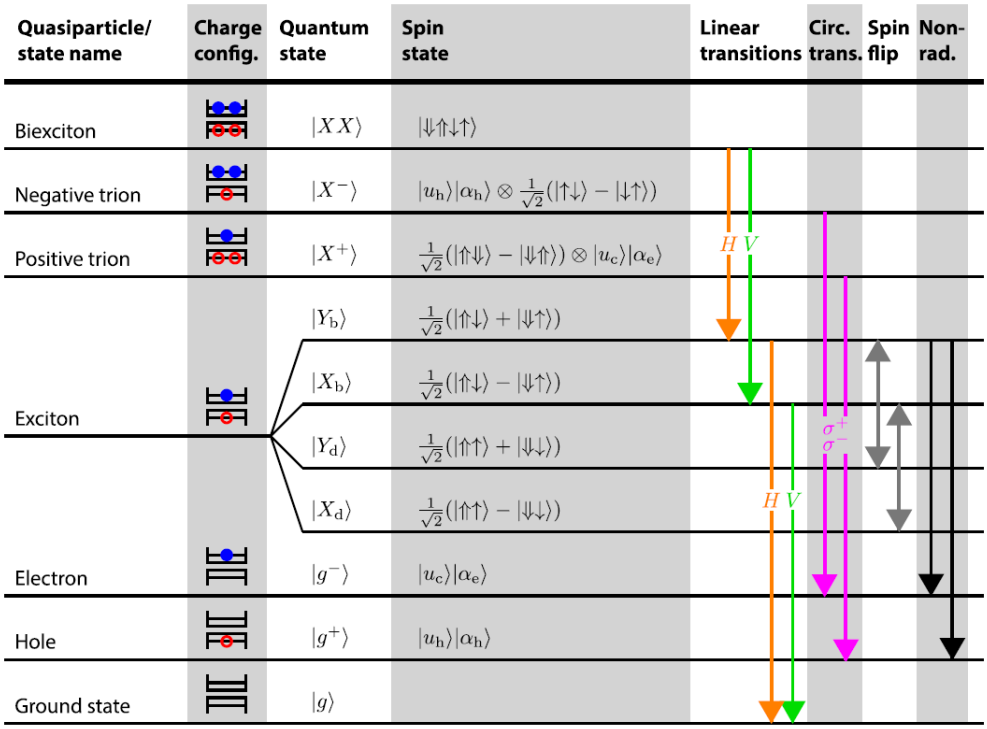

Figure 1.5: The lowest-energy confined states in quantum dots and the transitions between them. The full (empty) circles indicate the electron (hole) configuration in the conduction (valence) band s shells of the quantum dot. The biexciton may decay to one of the two bright exciton states by emission of a horizontally (H) or vertically (V) polarized photon. The negative (positive) trion decays to a single electron (hole) by emission of circularly polarized light with the helicity depending on the additional carrier. Furthermore, spin-flip processes (gray arrows) couple bright and dark excitons. Nonradiative processes (black arrows) of the bright excitons are indicated explicitly [58].

The QD energy levels and their corresponding envelope wavefunction for conduction or valance band $F_{c/v}$ satisfies the effective-mass Schrödinger equation given below

$$-\frac{\hbar^2}{2m_0}\nabla\cdot\left(\frac{1}{m^*(\mathbf{r})}\nabla F_{c/v}(\mathbf{r})\right)+V_{c/v}(\mathbf{r})F_{c/v}(\mathbf{r})=(E-E_{c/v})F_{c/v}(\mathbf{r}), \tag{1.46}$$

where m_0 is the electron rest mass and $m^*(\mathbf{r})$ is the anisotropic effective mass. $V_{c/v}(\mathbf{r})$ is the confinement potential, E is the electron eigenenergy, and $E_{c/v}$ is the band-edge energy. The complete wave function of an electron in the conduction band(c) or valance band(v) has this form,

$$|\Psi_{c/v}\rangle = |F_{c/v}\rangle|u_{c/v}\rangle|\alpha_{c/v}\rangle, \tag{1.47}$$

where $|u_{c/v}\rangle$, and $|\alpha_{c/v}\rangle$ are the the electronic Bloch function evaluated at the Γ point of the band structure and the spin state, respectively. The Γ point has the special advantage for defining a Bloch function as the new cell length is three times the unit cell. The dipole transition element matrix for spontaneous emission between any two QD states is defined as

$$\vec{P} = \langle\Psi_v|\vec{p}|\Psi_c\rangle \tag{1.48}$$
$$= \langle F_v|F_c\rangle\langle u_v|\vec{p}|u_c\rangle_{uc}\langle\alpha_v|\alpha_c\rangle, \tag{1.49}$$

where $\vec{p}$ dipole moment vector operator and uc represent unit cell. In semiconductor materials, electronic states are commonly expressed in equivalent electron-hole pictures. Therefore, the valance band states transformed into a hole picture by defining $|F_h\rangle = |F_v\rangle^*$, $|u_h\rangle = |u_v\rangle^*$, and $|\alpha_h\rangle = |\alpha_v\rangle^*$. We define electron and hole pseudospin in terms of total angular momentum of Bloch function and spin as $|\uparrow\rangle = |u_c\rangle|\uparrow_e\rangle$, $|\downarrow\rangle = |u_c\rangle|\downarrow_e\rangle$, $|\Uparrow\rangle = |u_h\rangle|\uparrow_h\rangle$, $|\Downarrow\rangle = |u_h\rangle|\downarrow_h\rangle$. The QD with a maximum number of two electrons and two holes produces several eigenstates in terms of the above basis states and their optically active dipole transitions presented in Fig. 1.5.

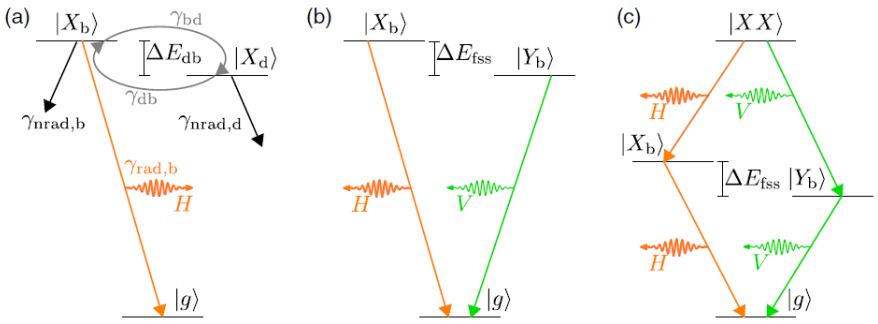

Figure 1.6: Examples of excitonic level schemes in quantum dots of relevance for quantum-optics experiments. (a) The most basic two-level optical transition scheme of a single bright exciton $|X_b\rangle$ decay to the ground state $|g\rangle$ along with nonradiative coupling to the dark exciton state $|X_d\rangle$ through spin-flip processes. (b) Optical V scheme formed by the two bright exciton states that decay to the ground state. The two orthogonally polarized bright excitons are split by the fine-structure splitting ΔE_{fss}. (c) Four-level scheme formed by the biexciton level, the two bright exciton levels, and the ground state. The biexciton decays through a cascaded process of either emitting two horizontally or two vertically polarized photons [58].

The simplest possible states, which show linearly polarized optical transitions, are bright excitons formed by pairing one electron and a hole. The dark excitons do not show any optical transition, but they can flip the spin and go to the bright state. The biexciton state has two perpendicularly polarised optically allowed transitions to the two bright exciton states. The Biexiton state is formed by the bound state of two excitons or a pair of electrons and holes. In Fig. 1.6, we show some simple possible optically active electronic level diagrams of a semiconductor QD usually considered in quantum optics [58]. In this thesis, we will consider the level system shown in Fig. 1.6 (a) and (c) for various problems.

1.3 Radiation-matter interaction

According to classical electrodynamics, a charged particle under the electric and magnetic field experiences Lorentz force. For an electron with charge $-e$ and velocity $\vec{v}$ under the electric field $\vec{E}$ and magnetic field $\vec{B}$ experience a Lorentz force $\vec{F} = -e(\vec{E} + \vec{v} \times \vec{B})$ [10]. As the particle experiences some force, there must be some potential associated with it. Investigation suggests that the electric and magnetic field can be expressed in terms of the scalar and vector potential $\phi(\vec{r}, t)$ and

$\vec{A}(\vec{r},t)$ as

$$\vec{E} = -\vec{\nabla}\phi - \frac{\partial \vec{A}}{\partial t} \tag{1.50}$$

$$\vec{B} = \vec{\nabla} \times \vec{A}. \tag{1.51}$$

Surprisingly, these potentials are not uniquely defined; they represent a group of potentials with an additional arbitrary function called gauge function. It is essential to mention that these potentials should transform in such a way that the observable electric and magnetic fields remain the same. Then, the expression for the scalar and vector potential in terms of the gauge function $\chi(\vec{r},t)$ will be

$$\phi(\vec{r},t) \rightarrow \phi^{'}(\vec{r},t) = \phi(\vec{r},t) + \frac{\hbar}{e}\frac{\partial \chi(\vec{r},t)}{\partial t}, \tag{1.52}$$

$$\vec{A}(\vec{r},t) \rightarrow \vec{A}^{'}(\vec{r},t) = \vec{A}(\vec{r},t) - \frac{\hbar}{e}\vec{\nabla}\chi(\vec{r},t), \tag{1.53}$$

where the constant factor $-\frac{\hbar}{e}$ taken on purpose and will be discussed later. Up to this point, we have only considered a single electron moving under the electromagnetic field. Now, we can think about hydrogen-like atoms where a havey nucleus bounds one outer shell electron through the Coulomb potential. Consequently, most of the properties of the atom are decided by the single electron instead of the immobile nucleus. In this consideration, we can write the classical Lagrangian of the system in terms of these two potentials. Then, the Hamiltonian of the system is obtained from the Lagrangian using the Legendre transformation. The classical electromagnetic interaction Hamiltonian described by

$$H_{cl} = \frac{1}{2m}[\vec{p} + e\vec{A}(\vec{r},t)]^2 - e\phi(\vec{r},t) + V(r). \tag{1.54}$$

where $\vec{p}$ and $V(r)$ are the canonical momentum and Coulomb potential respectively. Let's jump from the classical to the quantum picture by replacing the physical quantity with quantum mechanical operators such as $\vec{p} \rightarrow -i\hbar\vec{\nabla}$ [35, 36]. Then, the free Hamiltonian of the atom is given by

$$H = -\frac{\hbar^2}{2m}\nabla^2 + V(r). \tag{1.55}$$

The Schrödinger equation for the system with a probabilistic wavefunction $\psi(\vec{r},t)$ is written as

$$H\psi(\vec{r},t) = i\hbar\frac{\partial \psi(\vec{r},t)}{\partial t}, \tag{1.56}$$

$$\left[-\frac{\hbar^2}{2m}\nabla^2 + V(r)\right]\psi(\vec{r},t) = i\hbar\frac{\partial \psi(\vec{r},t)}{\partial t}. \tag{1.57}$$

Solution of the Schorindenger equation gives the wavefunction $\psi(\vec{r},t)$ and hence corresponding probability $|\psi(\vec{r},t)|^2$ of finding an electron at a position $\vec{r}$ and time t. If $\psi(\vec{r},t)$ is a solution of the Schrödinger equation, then a new wavefunction with an arbitrary phase factor $\psi^{'}(\vec{r},t) = \psi(\vec{r},t)\exp[i\chi]$ also satisfy the above equation and

provide same probability density for the constant χ. This problem is more interesting when χ depends on the local coordinates $(\vec{r},t)$ and the wavefunction have the form

$$\psi^{'}(\vec{r},t) = \psi(\vec{r},t)\exp[i\chi(\vec{r},t)]. \tag{1.58}$$

This new wave function does not satisfy the Schorindenger equation but provides the correct probability density as the modulus removes the extra phase part. In order to make the Hamiltonian local gauge invariant, we have to modify it by introducing the scalar and vector potentials as

$$\left\{\frac{1}{2m}\left[-i\hbar\vec{\nabla}+e\vec{A}\right]^2 - e\phi(\vec{r},t)+V(r)\right\}\psi(\vec{r},t) = i\hbar\frac{\partial\psi(\vec{r},t)}{\partial t}, \tag{1.59}$$

where m is the effective mass of the system. We notice that the quantum Hamiltonian shows a similar structure to the classical electromagnetic interaction Hamiltonian in Eq.(1.54). Recalling the gauge transformation we made earlier in Eq. (1.52)-(1.53), the new Hamiltonian is invariant under the local gauge transformation with the arbitrary function $\chi(\vec{r},t)$ given by

$$\psi(\vec{r},t) \rightarrow \psi(\vec{r},t)\exp[i\chi(\vec{r},t)], \tag{1.60}$$

$$\phi(\vec{r},t) \rightarrow \phi(\vec{r},t) + \frac{\hbar}{e}\frac{\partial\chi(\vec{r},t)}{\partial t}, \tag{1.61}$$

$$\vec{A}(\vec{r},t) \rightarrow \vec{A}(\vec{r},t) - \frac{\hbar}{e}\vec{\nabla}\chi(\vec{r},t). \tag{1.62}$$

In this transformation, physically observable quantities such as probability density and electric and magnetic fields remain unchanged. For further simplification of the Hamiltonian, we apply the Coulomb or radiation gauge given by $\phi(\vec{r},t) = 0$ and $\nabla\cdot\vec{A} = 0$ in Eq.(1.59). The modified Hamiltonian has a new form displayed below

$$H = -\frac{\hbar^2}{2m}\nabla^2 - \frac{i\hbar e}{2m}\vec{A}(\vec{r},t)\cdot\vec{\nabla} + \frac{e^2}{2m}\vec{A}^2(\vec{r},t) + V(r). \tag{1.63}$$

We introduce our first approximation on the spatial variation of the electric field over the atom, popularly known as "dipole approximation". The plane electromagnetic wave propagating near the atom can be expressed in terms of the vector potential as

$$\vec{A}(\vec{r}_0+\vec{r},t) = A\vec{(t)}\exp[i\vec{k}\cdot(\vec{r}_0+\vec{r})] \tag{1.64}$$

where $\vec{r}_0$ is the location of the nucleus. From this expression, it is clear that the different locations of the atom experience a different electric field. To reduce the complexity of the problem, we assume that the wavelength of the light is much larger than the atomic dimension mathematically expressed as $kr \ll 1$ or $2\pi r/\lambda \ll 1$. Under such practical approximation, simplified vector potential is written as

$$\vec{A}(\vec{r}_0+\vec{r},t) = \vec{A}(t)\exp[i\vec{k}\cdot(\vec{r}_0+\vec{r})] \tag{1.65}$$

$$= \vec{A}(t)\exp(i\vec{k}\cdot\vec{r}_0)[1+i\vec{k}\cdot\vec{r}+\cdots] \tag{1.66}$$

$$\approx \vec{A}(t)\exp(i\vec{k}\cdot\vec{r}_0). \tag{1.67}$$

The dipole approximation says that EM-wave interaction with a tiny atom for a large wavelength experiences an almost constant electric field calculated at the nucleus.

By putting this new expression of the vector potential in the Eq.(1.63), the modified Hamiltonian has this form

$$H = -\frac{\hbar^2}{2m}\nabla^2 - \frac{i\hbar e}{2m}\vec{A}(\vec{r}_0,t)\cdot\vec{\nabla} + \frac{e^2}{2m}\vec{A}^2(\vec{r}_0,t) + V(r). \tag{1.68}$$

Creating a further compact form of the Hamiltonian requires a proper unitary transformation frame of reference or, equivalently, a gauge transformation $\chi(\vec{r},t) = -e\vec{A}(\vec{r}_0,t)\cdot\vec{r}/\hbar$. This gauge transformation redefines the wavefunction as

$$\psi(\vec{r},t) \rightarrow \psi(\vec{r},t)\exp[-\frac{ie}{\hbar}\vec{A}(\vec{r}_0,t)\cdot\vec{r}]. \tag{1.69}$$

In the case of a Coulomb gauge, the electric field at $\vec{r}_0$ and time t satisfies the relation $\vec{E}(\vec{r}_0,t) = -\frac{\partial}{\partial t}\vec{A}(\vec{r}_0,t)$. Therefore, the Schrödinger equation for the redefined wavefunction is given by

$$\left[-\frac{\hbar^2}{2m}\nabla^2 + V(r) + e\vec{r}\cdot\vec{E}\right]\psi(\vec{r},t) = i\hbar\frac{\partial\psi(\vec{r},t)}{\partial t}. \tag{1.70}$$

The total Hamiltonian can be divided into two parts they are the free Hamiltonian H_0 and the interaction Hamiltonian H_I where

$$H = H_0 + H_I. \tag{1.71}$$

Finally, the interaction Hamiltonian can be written in terms of the electric dipole moments defined by $\vec{d} = -e\vec{r}$ as

$$H_I = -\vec{d}\cdot\vec{E}. \tag{1.72}$$

In this thesis, we only use this interaction Hamiltonian for the radiation-matter interaction.

1.4 Electron-phonon interaction

In this section, we will understand the influence of the solid-state nature of the QD on the optical properties. In the fabrication process, QDs are grown inside a crystalline semiconductor. Therefore, the QD directly interacts with the surrounding host crystal lattice. A crystal comprises atoms placed in a periodic arrangement and connected by covalent bonds. Thus, any external stimulation causes vibration of the atoms around their equilibrium position, resulting in the collective lattice vibration. The vibration energy of the lattice can be quantized similarly to electromagnetic radiation and the fundamental quasiparticle known as a phonon [59, 60]. The phonons are classified into three groups: thermal phonons (thermal vibration), acoustical phonons (sound wave), and optical phonons (optical radiation). In this study, we investigate the effect of phonon due to the thermally excited lattice vibration only.

To understand the properties of phonons, we consider a simple model system of a one-dimensional linear harmonic chain of N identical atoms, as shown in Fig. 1.7. These atoms in the chain have mass m, and the periodic separation a is also known as the lattice constant in solid-state physics. For simplicity, we have considered that each atom can interact with the nearest neighbor atoms only, and the classical spring-mass

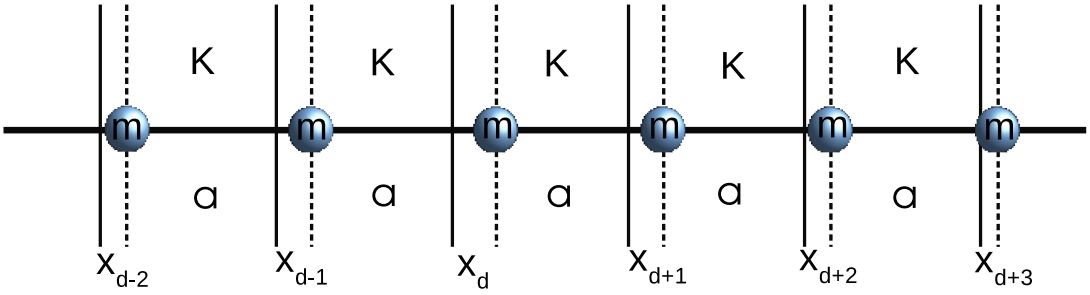

Figure 1.7: Schematic diagram of the one-dimensional periodic chain of identical atoms. The periodic separation and the spring constant between neighboring atoms are a and K, respectively. All the displacements defined here are from their respective equilibrium positions.

system replaces the actual electronic bond interaction with a spring constant K. In such a configuration, a small displacement x_d of the d-site atom from its equilibrium position affects other atoms in the chain and gets displaced from their respective equilibrium position. The potential energy stored in a spring-mass system due to the displacement has the well-known form $(1/2)Kx^2$. Therefore, the total Hamiltonian of the system can be written as

$$H = \sum_d \frac{1}{2m} p_d^2 + \frac{1}{2} K (x_d - x_{d-1})^2, \tag{1.73}$$

where $p_d = \dot{x}_d$ is the canonical momentum. The resultant force on a particular atom comes from the two neighboring atoms calculated from the above Hamiltonian given by

$$m\ddot{x}_d = K(x_{d+1} + x_{d-1} - 2x_d). \tag{1.74}$$

To solve this equation, we impose a periodic boundary condition with the equal displacement of the first and last atom in the chain expressed as $x_{d+N} = x_d$ where $d \in \mathbf{Z}$. By applying this condition in Eq.(1.74), we can write down the general solution as

$$x_d = Ae^{-i\omega t - ikad}, \tag{1.75}$$

where ω and k are the frequency and the weave vector, respectively. Surprisingly, the lattice's symmetry keeps the solution invariant under the transformation $k \to k + 2\pi/a$. Therefore, any wave vector can be accessible in the first Brillouin zone within the range $-\pi/2$ to $\pi/2$. The periodic condition $x_{d+N} = x_d$ of the atomic chain also discretized the value of k with the expression $k = 2\pi l/Na$ where $l = -N/2, \cdots, N/2$. Now putting the solution Eq.(1.75) in the equation of motion Eq.(1.74), the frequency dispersion relation has the structure

$$\omega = 2\sqrt{\frac{K}{m}} \left| \sin\left(\frac{ka}{2}\right) \right|. \tag{1.76}$$

The phonons are characterized by their dispersion properties. Hence, the above dispersion relation sketch with k ranging over the first Brillouin zone displays a lower phonon branch corresponding to the acoustic phonons. Further, one can extend this model system with two or more non-identical atoms for more exciting results. We will not present the calculation for such systems here, as they are similar to the previous

calculations and given in any standard textbook. The dispersion relation of the diatomic chain depicts a new upper phonon branch corresponding to the optical phonons along with the previous acoustic phonons branch. In the case of acoustic phonons, the two oppositely charged ions of a diatomic compound move in the same phase (same direction). However, for optical phonon, the positively and negatively charged ion moves in the out of phase (opposite direction). Analyzing the lattice with one dimension, we see only one acoustic and one optical branch in the diatomic case. For a three-dimensional lattice, the acoustic phonon branch is divided into longitudinal acoustic (LA) and transverse acoustics (TA) branches; on the other hand, the optical phonon branch is classified into longitudinal optical (LO) and transverse optical (TO) branches. In the case of a three-dimensional lattice with p number of atoms in the unit cell, have one LA and two TA phonon branches along with (p - 1) LO and 2(p - 1) TO phonon branches. The longitudinal and transverse branches are identified by the atomic vibration along the wave propagation or its transverse direction.

Let's introduce the normal mode coordinates for the position and momentum of the linear monoatomic chain to get a compact form of the Hamiltonian in Eq.(1.73). Therefore, the normal modes in Fourier space are defined by transforming the canonical variables using the discrete Fourier transformation. The normal modes of the system with considered boundary condition is given by

$$x_k = \frac{1}{\sqrt{N}} \sum_d e^{-ikad} x_d, \qquad x_d = \frac{1}{\sqrt{N}} \sum_k e^{ikad} x_k, \tag{1.77}$$

$$p_k = \frac{1}{\sqrt{N}} \sum_d e^{ikad} p_d, \qquad p_d = \frac{1}{\sqrt{N}} \sum_k e^{-ikad} p_k. \tag{1.78}$$

By using the normal modes Eq.(1.77)-(1.78) in the Hamiltonian Eq.(1.73), we get the new form of the Hamiltonian in a wave vector basis expressed as

$$H = \frac{1}{2m} \sum_k [p_k p_{-k} + m^2 \omega_k^2 x_k x_{-k}], \tag{1.79}$$

where k is the usual wave vector and ω_k displayed in Eq.(1.76). This Hamiltonian looks similar to the previously derived EM-radiation Hamiltonian in Eq.(1.23); therefore, we can replace the classical operators by the quantum operators $\hat{x}_k, \hat{p}_k$ to get the quantum Hamiltonian. Following the previously used technique, we can define the annihilation and creation operator for the lattice vibration as

$$b_k = \frac{1}{\sqrt{2m\hbar\omega_k}} (m\omega_k \hat{x}_k + i\hat{p}_{-k}) \tag{1.80}$$

$$b_k^\dagger = \frac{1}{\sqrt{2m\hbar\omega_k}} (m\omega_k \hat{x}_k - i\hat{p}_{-k}). \tag{1.81}$$

These operators follow all the bosonic commutation relations similar to the EM-radiation case. The final quantized Hamiltonian of the one-dimensional monoatomic lattice can be written as

$$H = \hbar \sum_k \omega_k \left(b_k^\dagger b_k + \frac{1}{2} \right). \tag{1.82}$$

Extending this formalism for a three-dimensional lattice, the vibrational degrees of freedom of an atom will be three with the wave vector $\vec{k}$; this leads to the three polarisation state of phonon branches defined as s with one longitudinal and two transverse polarization. The general Hamiltonian for a three-dimensional lattice vibration is written as

$$H = \hbar \sum_{\vec{k}s} \omega_{\vec{k}s} \left(b^{\dagger}_{\vec{k}s} b_{\vec{k}s} + \frac{1}{2} \right). \tag{1.83}$$

Finally, we have successfully quantized the lattice vibration to get the free phonon Hamiltonian. Next, we want to analyze the interaction between electrons and phonons in a solid-state lattice. Mainly, three types of electron-phonon interactions are observed in solid-state systems: (i) deformation potential coupling to acoustic and optical phonons, (ii) piezoelectric coupling to acoustic phonons, and (iii) polar coupling to optical phonons (Fröhlich interaction). Among them, piezoelectric and polar couplings are very weak compared to the deformation potential coupling with the acoustic phonons. Therefore, our investigation in this thesis is limited to the deformation coupling with acoustic phonons only. The interaction between the electron and the rest of the atom is called an ion, depending on their length separation. Let us consider a solid-state crystals with atomic positions $\vec{R}_d$ and an electron inside the emitter with position $\vec{r}_j$, then interaction Hamiltonian is defined as

$$H_{ea} = \sum_{jd} V(\vec{r}_j - \vec{R}_d). \tag{1.84}$$

The lattice vibration or phonon causes the atoms to vibrate around their equilibrium position $\vec{R}_{0d}$ with a tiny displacement $\vec{x}_d$ hence the current position can be written as $\vec{R}_d = \vec{R}_{0d} + \vec{x}_d$. By putting this condition in Eq. (1.84) and expanding the potential in a Taylor series around $\vec{R}_{0d}$ we get

$$H_{ea} = \sum_{jd} V(\vec{r}_j - \vec{R}_{0d} - \vec{x}_d) = \sum_{jd} [V(\vec{r}_j - \vec{R}_{0d}) - \vec{x}_d \cdot \vec{\nabla} V(\vec{r}_j - \vec{R}_{0d}) + \mathcal{O}(\vec{x}_d^2)]. \tag{1.85}$$

The first term of the Taylor series is associated with the Coulomb potential between the electron and all the atoms in the equilibrium position in a static lattice. Hence, an explicit form of this potential is given by

$$V(\vec{r}_j - \vec{R}_{0d}) = \frac{1}{4\pi\epsilon} \sum_{jd} \frac{(-e)q_d}{|\vec{r}_j - \vec{R}_{0d}|} \tag{1.86}$$

where $-e$ and q_d are the charges of electron and ion, ϵ stands for the permitivity of the medium. Looking at the second term of the Taylor series expansion, we understand that the contribution only comes from the small potential variation due to the lattice vibration or phonon. Therefore, the second term represents the electron-phonon interaction expressed as

$$V_{e-ph}(\vec{r}_j - \vec{R}_{0d}) = \sum_{jd} \vec{x}_d \cdot \vec{\nabla} V(\vec{r}_j - \vec{R}_{0d}) = \frac{1}{4\pi\epsilon} \sum_{jd} \vec{x}_d \cdot \vec{\nabla} \left[\frac{(-e)q_d}{|\vec{r}_j - \vec{R}_{0d}|} \right]. \tag{1.87}$$

Again, we introduce the normal modes in the Fourier domain to simplify this interaction potential. For the three-dimensional lattice, all the one-dimensional displacement

is replaced by three-dimensional vectors, and the sum over d is now the sum over $\vec{R}_{0d}$. The interaction potential and displacement in the Fourier domain have this form

$$V(\vec{r}) = \frac{1}{N}\sum_{\vec{q}} V(\vec{q})e^{i\vec{q}\cdot\vec{r}} \tag{1.88}$$

$$\vec{x}_{\vec{q}} = \frac{1}{\sqrt{N}}\sum_{d} \vec{x}_d e^{-i\vec{q}\cdot\vec{R}_{0d}} \equiv \frac{1}{\sqrt{N}}\sum_{\vec{R}_{0d}} \vec{x}_d e^{-i\vec{q}\cdot\vec{R}_{0d}} \tag{1.89}$$

By using Eq.(1.88) and Eq.(1.89) in the Eq.(1.87) we can rewrite the interaction potential as

$$V_{e-ph}(\vec{r}_j) = \frac{i}{\sqrt{N}}\sum_{j\vec{q}} V(\vec{q})e^{i\vec{q}\cdot\vec{r}_j}\,\vec{q}\cdot\vec{x}_{\vec{q}}. \tag{1.90}$$

The wave vector $\vec{q}$ has no restrictions and spans all the Fourier space. However, to keep this wave vector in the first Brillouin zone, it is necessary to satisfy the condition $\vec{q} = \vec{k} + \vec{G}$ where $\vec{G}$ is the reciprocal lattice vector. Recalling the Eq.$(1.80 - 1.81)$ and putting in Eq.(1.90), the operator form of the interaction potential can be written as

$$V_{e-ph}(\vec{r}_j) = i\sum_{j\vec{k}\vec{G}} \sqrt{\frac{\hbar}{2mN\omega_{\vec{k}s}}} V(\vec{k}+\vec{G})e^{i(\vec{k}+\vec{G})\cdot\vec{r}_j}(\vec{k}+\vec{G})\cdot\vec{\xi}_{\vec{k}s}\left(b_{\vec{k}s} + b^{\dagger}_{\vec{k}s}\right). \tag{1.91}$$

Here, we have considered the operators so that wave vectors of the phonons always lie inside the first Brillouin zone. The above equation displays a single electron's interaction potential energy at $\vec{r}_j$. To get the total interaction Hamiltonian, we must sum up all the electrons' energy inside the emitter. Let's say $\rho(\vec{r})$ is the charged density of an elementary volume centered at the position vector $\vec{r}$. For such a distribution, the summation is converted to integration, and the electron-phonon interaction Hamiltonian is

$$H_{e-ph} = \int d^3r\,\rho(\vec{r})V_{e-ph}(\vec{r}) \tag{1.92}$$

$$= i\sum_{\vec{k}\vec{G}} \sqrt{\frac{\hbar}{2mN\omega_{\vec{k}s}}} \rho(\vec{k}+\vec{G})V(\vec{k}+\vec{G})(\vec{k}+\vec{G})\cdot\vec{\xi}_{\vec{k}s}\left(b_{\vec{k}s} + b^{\dagger}_{\vec{k}s}\right). \tag{1.93}$$

where $\rho(\vec{k}+\vec{G})$ is the Fouriar transform of the $\rho(\vec{r})$. The electron-phonon transition matrix is defined as

$$M_{\vec{k}+\vec{G},s} = i\sqrt{\frac{\hbar}{2mN\omega_{\vec{k}s}}} V(\vec{k}+\vec{G})(\vec{k}+\vec{G})\cdot\vec{\xi}_{\vec{k}s}. \tag{1.94}$$

Finally, the general form of the electron-phonon interaction Hamiltonian is given by

$$H_{e-ph} = \sum_{\vec{k}\vec{G}s} M_{\vec{k}+\vec{G},s}\rho(\vec{k}+\vec{G})\left(b_{\vec{k}s} + b^{\dagger}_{\vec{k}s}\right). \tag{1.95}$$

1.4.1 Deformation potential coupling

The concept of deformation potential was first developed by Bardeen and Shockley[61] in 1950 to explain various characteristics of crystal vibration. Later, Herring and Vogt [62] extended this idea for many valley semiconductors by addressing previous model drawbacks and the inclusion of degenerate states. Further, the theory of strain-dependent band structure of a semiconductor and the origin of deformation potential was carried out by Bir and Pikus[63] using group theory. The potential energy change of a confined electron due to the crystal deformation is known as deformation potential. This crystal deformation can happen due to thermal lattice vibration or externally produced strain. Thus, uncontrolled thermal vibration (phonon) interaction leads to a distorted electronic energy state with a modified band gap that affects the emitter's emission spectrum. The transition matrix elements carry the information of the deformation potential coupling strength between electron and phonon. In thermal equilibrium, the excited state energy lies near the band minimum with the wave vector near the zone center or edge. Usually, the excited state electron and long wavelength phonon interaction take care of the polaron effect in the system. Three electron-phonon interactions are popular in the literature. They are deformation coupling to acoustical phonons, piezoelectric coupling to acoustical phonons, and polar coupling to optical phonons. All these interactions are prominent in the long wavelength phonon limit. As mentioned earlier, the coupling between deformation potential and acoustic phonon dominates for the long wavelength limit; therefore, we can safely choose the reciprocal vector $\vec{G} = 0$. For $\vec{k} \to 0$, the potential $V(\vec{k}) \to D$ where D is the deformation potential constant. Also, for the long wavelength limit $\vec{\xi}_{\vec{k}} \to \hat{k}$ this suggests only the longitudinal phonons are important if the bands are nondegenerate [59]. After applying these assumptions, the electron-phonon interaction Hamiltonian is given by

$$H_{e-ph} = \sum_{\vec{k}LA} M_{\vec{k},LA}\rho(\vec{k}) \left(b_{\vec{k}LA} + b^{\dagger}_{\vec{k}LA} \right). \tag{1.96}$$

where the transition matrix has the form

$$M_{\vec{k},LA} = iD\sqrt{\frac{\hbar}{2mN\omega_{\vec{k}LA}}}|\vec{k}|. \tag{1.97}$$

1.4.2 Phonon spectral density function

In this subsection, we are interested in finding the analytical form of the phonon spectral density function. To do so, we have to choose a specific system. Let us consider a simple system of two-state semiconductor QD interacting with the phonon due to the thermal vibration. The QD states are labeled as a ground state $|g\rangle$ and excited state $|e\rangle$. The ground and excited states are situated in the valance and conduction bands for a semiconductor QD, respectively. Therefore, the charge density could differ for the two energy levels according to their corresponding bands. Suppose the charge densities correspond to the ground and exited states are $\rho_{gg}(\vec{k})$ and $\rho_{ee}(\vec{k})$ then the total charge density would be

$$\rho(\vec{k}) = \rho_{gg}(\vec{k})|g\rangle\langle g| + \rho_{ee}(\vec{k})|e\rangle\langle e| \quad = \frac{I}{2}(\rho_{ee}(\vec{k}) + \rho_{gg}(\vec{k})) + \sigma_z(\rho_{ee}(\vec{k}) - \rho_{gg}(\vec{k})) \tag{1.98}$$

where I and σ_z are the identity operator and z-component of the Pauli matrix, respectively. We have neglected the cross terms in the charge density because of the much larger QD emission frequency than the phonon. The first term in Eq.(1.98) can only produce a constant energy shift, modifying the free Hamiltonian. Neglecting the first term of the charge density Eq.(1.98) and putting in Eq.(1.96) we get the final form of the QD-phonon interaction Hamiltonian

$$H_{QD-ph} = \sigma_z \sum_{\vec{k}} M_{\vec{k}} \left(b_{\vec{k}} + b^{\dagger}_{\vec{k}} \right), \tag{1.99}$$

$$M_{\vec{k}} = i \sqrt{\frac{\hbar}{2mN\omega_{\vec{k}}}} |\vec{k}| (D_e \rho_{ee}(\vec{k}) - D_g \rho_{gg}(\vec{k})). \tag{1.100}$$

where D_e and D_g are the deformation potential constant of the conduction and valance band, respectively. The charge density corresponds to individual QD states best expressed in terms of the symmetrical ground state wavefunction of the conduction and valence band as [64]

$$\rho_{jj}(\vec{k}) = \int d^3r |\phi_j(\vec{r})|^2 e^{i\vec{k}\cdot\vec{r}}, \tag{1.101}$$

$$\phi_j(\vec{r}) = \frac{1}{(l_j\sqrt{\pi})^{3/2}} e^{-\frac{r^2}{2l_j^2}}, j \in \{e, g\}, \tag{1.102}$$

where l_j is the confinement length of the QD. The transition matrix takes a new form

$$M_{\vec{k}} = i \sqrt{\frac{\hbar}{2mN\omega_{\vec{k}}}} |\vec{k}| \int d^3r \left[D_e |\phi_e(\vec{r})|^2 - D_g |\phi_g(\vec{r})|^2 \right] e^{i\vec{k}\cdot\vec{r}}. \tag{1.103}$$

After performing the Fouriar transformation in Eq.(1.103) we get

$$M_{\vec{k}} = i \sqrt{\frac{\hbar}{2mN\omega_{\vec{k}}}} |\vec{k}| \left[D_e e^{-\frac{1}{4}k^2 l_e^2} - D_g e^{-\frac{1}{4}k^2 l_g^2} \right] \tag{1.104}$$

The phonon spectral density function is defined to find exciton-phonon coupling strength in a QD as [64, 65]

$$J(\omega) = \sum_{\vec{k}} |M_{\vec{k}}|^2 \delta(\omega - \omega_{\vec{k}}). \tag{1.105}$$

To find the phonon spectral density function, we assume spherically symmetric QD with equal confinement length $l_e = l_g = l$ and the liner dispersion relation $\omega_{\vec{k}} = c_s \vec{k}$ where c_s is the speed of sound. For closely spaced phonon modes, the sum over $\vec{k}$ is transformed to the integration over a continuous variable k to find the analytical form of the spectral function given by

$$J(\omega) = \alpha_p \omega^3 e^{-\frac{\omega^2}{2\omega_c^2}}. \tag{1.106}$$

where $\omega_c = \sqrt{2} c_s / l$ and $\alpha_p = (D_e^2 - D_g^2)\hbar / 4\pi^2 \rho_V c_s^5$ are the cutoff frequency and the coupling strength respectively.

1.5 Two level system dynamics

In this section, we will try to understand how to find the dynamics of a QD interacting with an electromagnetic field. The QD consists of many optically allowed eigenstates corresponding to their discrete energy levels, as shown in Fig. 1.5. Therefore, consideration of all the energy levels makes the system complicated to understand the underlying physics. Hence, we choose a monochromatic field with a frequency close to the difference between two optically allowed transition levels. Thus, all other QD levels are highly detuned except the resonant one, approximating the QD into a practical two-level system. Studying two-level QD is crucial for understanding the coherent interaction between light and QD and their effect on QD's optical properties.

1.5.1 Rabi model

Let us consider the QD system with a bright exciton state $|1\rangle$ and ground state $|2\rangle$ with dipole-allowed transition among them, separated by the emission frequency ω_{QD}. Initially, all the QD population resides in the ground state. Then, a weak EM-field coupled to the $|1\rangle \leftrightarrow |2\rangle$ transition transfers a small population from the ground state to the excited state. The system is treated semiclassically by considering the EM field as a continuous wave interacting with the quantized QD energy levels. The schematic level diagram of the mentioned model system is displayed in Fig. 1.8.

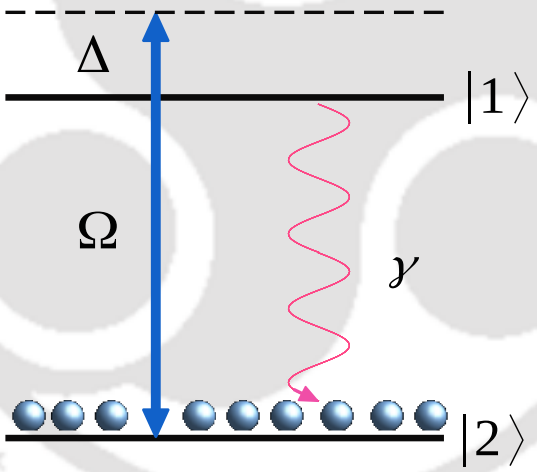

Figure 1.8: Schematic diagram of a two-level QD system interacting with an electromagnetic field with the Rabi frequency Ω and detuning Δ. The excited state decays to the ground state by the spontaneous emission process with a characteristic decay rate γ.

The electric field of a classical electromagnetic radiation is given by

$$\vec{E}(\vec{r},t) = \hat{e}\mathcal{E}(\vec{r},t)e^{i(\vec{k}.\vec{r}-\omega t)} + c.c., \tag{1.107}$$

where $\hat{e}$, $\mathcal{E}(\vec{r},t)$ are the polarization and the amplitude envelop function respectively. Subsequently, the frequency and wave vector of the incident light is ω and k, which satisfy the linear dispersion relation $\omega = ck$ where c is the speed of light in free space. By choosing the QD ground state eigenfrequency zero and recalling the radiation matter interaction in Eq.(1.72), we can write down the total Hamiltonian as

$$H^{'} = H_0 + H_I = \hbar\omega_{QD}|1\rangle\langle 1| - \vec{d}\cdot\vec{E}(\vec{r},t) \tag{1.108}$$

where $\vec{d}$ is the induced dipole moment in the medium. Now, to find the explicit form of the interaction Hamiltonian, we apply the identity operator to both sides of the H_I and use the identity $|1\rangle\langle 1| + |2\rangle\langle 2| = 1$. The interaction Hamiltonian H_I takes the form

$$H_I = -[\vec{d}_{12} \cdot \hat{e}\mathcal{E}(\vec{r},t)e^{i(\vec{k}\cdot\vec{r}-\omega t)} + \vec{d}_{12} \cdot \hat{e}\mathcal{E}^*(\vec{r},t)e^{-i(\vec{k}\cdot\vec{r}-\omega t)}]|1\rangle\langle 2| \tag{1.109}$$

$$-[\vec{d}_{21} \cdot \hat{e}\mathcal{E}(\vec{r},t)e^{i(\vec{k}\cdot\vec{r}-\omega t)} + \vec{d}_{21} \cdot \hat{e}\mathcal{E}^*(\vec{r},t)e^{-i(\vec{k}\cdot\vec{r}-\omega t)}]|2\rangle\langle 1| \tag{1.110}$$

where dipole matrix element $\vec{d}_{ij} = \langle i|\vec{d}|j\rangle$ and * denote the complex conjugate of the function. We have neglected the same parity term in the above expression to satisfy the dipole interaction selection rule. To express the interaction Hamiltonian in a compact form, let's define the Rabi frequencies [66] as

$$\Omega = \frac{\vec{d}_{12} \cdot \hat{e}}{\hbar}\mathcal{E}(\vec{r},t)e^{i\vec{k}\cdot\vec{r}} \qquad \text{and} \qquad \overline{\Omega} = \frac{\vec{d}_{12} \cdot \hat{e}}{\hbar}\mathcal{E}^*(\vec{r},t)e^{-i\vec{k}\cdot\vec{r}}. \tag{1.111}$$

The interaction Hamiltonian after considering Rabi frequencies is

$$H_I = -\hbar[\Omega e^{-i\omega t} + \overline{\Omega}e^{i\omega t}]|1\rangle\langle 2| - \hbar[\Omega^* e^{i\omega t} + \overline{\Omega}^* e^{-i\omega t}]|2\rangle\langle 1|. \tag{1.112}$$

Therefore, the total Hamiltonian of a QD-light interaction is described by

$$H^{'} = \hbar\omega_{QD}|1\rangle\langle 1| - \hbar[\Omega e^{-i\omega t} + \overline{\Omega}e^{i\omega t}]|1\rangle\langle 2| - \hbar[\Omega^* e^{i\omega t} + \overline{\Omega}^* e^{-i\omega t}]|2\rangle\langle 1|. \tag{1.113}$$

The above Hamiltonian has an explicit time dependence with the oscillating terms having frequency $\pm\omega$. To remove the explicit time dependence from the Hamiltonian, we must consider a suitable unitary transformation U. The interaction picture Hamiltonian after such unitary transformation follows the rule

$$H = U^{\dagger}H^{'}U - i\hbar U^{\dagger}\frac{\partial U}{\partial t}. \tag{1.114}$$

In this case, we have chosen the unitary transformation to be

$$U = e^{-i\omega|1\rangle\langle 1|t}. \tag{1.115}$$

After this transformation, the total Hamiltonian takes the following form

$$H = -\hbar\Delta|1\rangle\langle 1| - \hbar[\Omega + \overline{\Omega}e^{2i\omega t}]|1\rangle\langle 2| - \hbar[\Omega^* + \overline{\Omega}^* e^{-2i\omega t}]|2\rangle\langle 1|. \tag{1.116}$$

where the detuning is defined as $\Delta = \omega - \omega_{QD}$. Looking at the Hamiltonian in Eq.(1.116), it is clear that the $\overline{\Omega}$ is associated with the rapidly oscillating terms with frequency $\pm 2\omega$. Therefore, the contribution from such high-frequency terms is negligible under current consideration. For that reason, the approximate Hamiltonian by safely neglecting the rapidly oscillating terms, is given by

$$H = -\hbar\Delta|1\rangle\langle 1| - \hbar\Omega|1\rangle\langle 2| - \hbar\Omega^*|2\rangle\langle 1|. \tag{1.117}$$

This particular approximation is popularly known as the rotating wave approximation (RWA) [67]. After the RWA approximation, the final Hamiltonian becomes explicitly time-independent, as shown in Eq.(1.117).

1.5.2 Density Matrix formalism

Until now, we have only discussed the single emitter system whose wavefunction $|\psi\rangle$ carries all the system information. The system dynamics can be easily obtained in such cases by solving the Schrödinger equation $H|\psi\rangle = i\hbar\partial|\psi\rangle/\partial t$. The above treatments become ineffective when ensembles of large identical emitters are considered in the system with various incoherent decay processes. In this scenario, finding the exact wave function of the whole system is challenging. The concept of a statistical mixture of wavefunctions with classical probability has been introduced to address such a problem. The density matrix operator is defined by

$$\rho = \sum_i p_i |\psi_i\rangle\langle\psi_i| \tag{1.118}$$

where p_i is the classical probability of finding the system in the $|\psi_i\rangle$ state. The conservation of probability suggests that the sum over all possible realization is equal to unity mathematically expressed as $\sum_i p_i = 1$. Let's consider a case when the system is exactly in the $|\psi_0\rangle$ state, the density matrix for the system $\rho = |\psi_0\rangle\langle\psi_0|$ with the probability $p_0 = 1$. This type of quantum state is called a pure state. Now, we are interested in finding the expectation value of a quantum operator associated with some observable. For a quantum operator $\mathcal{O}$, the expectation value after averaging over a quantum mechanical and statistical ensemble is given by

$$\langle\mathcal{O}\rangle = Tr(\mathcal{O}\rho) = Tr(\rho\mathcal{O}) \tag{1.119}$$

where Tr represents the trace of a matrix. Some of the important properties of the density matrix have been used to distinguish the different classes of the quantum state, as given below

$$i) \quad \text{Normalisation condition:} Tr[\rho] = 1 \tag{1.120}$$
$$ii) \quad \text{For a pure state:} Tr[\rho^2] = 1 \tag{1.121}$$
$$iii) \quad \text{For a mixed state:} Tr[\rho^2] < 1. \tag{1.122}$$

The density matrix contains complete system information by finding all the elements. The elements of a density matrix are defined by $\rho_{ij} = \langle i|\rho|j\rangle$ where i, j ran over all the states. The diagonal elements of the density matrix with $i = j$ refer to the population in that state. On the other hand, off-diagonal elements of the density matrix with $i \neq j$ refer to the coherence term between two states $|i\rangle$ and $|j\rangle$, which decide the optical properties of the medium by controlling the susceptibility. The time evolution of a quantum mechanical system's wavefunction $|\psi_i\rangle$ determined by the Schrödinger equation

$$\frac{\partial|\psi_i\rangle}{\partial t} = \frac{1}{i\hbar}H|\psi_i\rangle. \tag{1.123}$$

In this regard, to find the time evolution of the density matrix, we take a time derivative of ρ as

$$\dot{\rho} = \sum_i p_i \left(\frac{\partial|\psi_i\rangle}{\partial t}\langle\psi_i| + |\psi_i\rangle\frac{\partial\langle\psi_i|}{\partial t}\right) \tag{1.124}$$

where p_i is a time-independent quantity. Using Eq.(1.123) in Eq.(1.124), we get the final form of the density matrix dynamics, often called Liouville or Von Neumann equation given by

$$\dot{\rho} = \frac{1}{i\hbar}[H, \rho]. \tag{1.125}$$

This Liouville equation completely describes the dynamics of a coherently interacting system. However, any natural system always suffers from incoherent processes such as spontaneous emission [68], decoherence, dephasing, collision, thermal vibration, etc. These processes are responsible for the decay of the excited state to the ground state. The density matrix formalism allows us to incorporate such decay rates via relaxation matrix Γ defined by $\langle n|\Gamma|m\rangle = \gamma_n \delta_{nm}$. Therefore, the modified Liouville equation looks like

$$\dot{\rho} = \frac{1}{i\hbar}[H, \rho] - \frac{1}{2}\{\Gamma, \rho\}, \tag{1.126}$$

where the anti-commutator bracket $\{\Gamma, \rho\} = \Gamma\rho + \rho\Gamma$. Generally, all the relaxation processes may not necessarily fit into this particular formalism but rather show a much-complicated structure. From the above equation, (i, j)th element of the density matrix is

$$\dot{\rho}_{ij} = \frac{1}{i\hbar}\sum_k (H_{ik}\rho_{kj} - \rho_{ik}H_{kj}) - \frac{1}{2}\sum_k (\Gamma_{ik}\rho_{kj} + \rho_{ik}\Gamma_{kj}). \tag{1.127}$$

For a two-level system Eq.(1.127) transformed into a new form by introducing Lindbladian term as

$$\dot{\rho} = \frac{1}{i\hbar}[H, \rho] + \frac{\gamma}{2}\mathcal{L}[\sigma^-]\rho, \tag{1.128}$$

where $\sigma^- = |2\rangle\langle 1|$. The Lindbladian superoperator acting upon an operator $\mathcal{O}$ expressed as $\mathcal{L}[\mathcal{O}]\rho = 2\mathcal{O}\rho\mathcal{O}^\dagger - \mathcal{O}^\dagger\mathcal{O}\rho - \rho\mathcal{O}^\dagger\mathcal{O}$. The Eq.(1.128) is called the master equation in the literature. This thesis will use the master equation formalism to study the dynamics of various quantum optical systems.

1.5.3 Time-dependent solution

In the previous subsection, we have understood the basic formalism of the density matrix. Now, we will apply this theory to find the dynamics of a two-level system. For a two-level system, the density matrix will be a 2×2 matrix with four elements. Among them, two diagonal elements ρ_{11} and ρ_{22} are the population, and the remaining two off-diagonal elements ρ_{12} and ρ_{21} are the coherence term. Recalling Eq.(1.128), the coupled linear differential equations of the density matrix are given by

$$\dot{\rho}_{11} = i\Omega\rho_{21} - i\Omega^*\rho_{12} - \gamma\rho_{11}, \tag{1.129}$$

$$\dot{\rho}_{12} = i\Omega(\rho_{22} - \rho_{11}) - (\frac{\gamma}{2} - i\Delta)\rho_{12}, \tag{1.130}$$

$$\dot{\rho}_{21} = i\Omega^*(\rho_{11} - \rho_{22}) - (\frac{\gamma}{2} + i\Delta)\rho_{21}, \tag{1.131}$$

$$\dot{\rho}_{22} = i\Omega^*\rho_{12} - i\Omega\rho_{21} + \gamma\rho_{11}. \tag{1.132}$$

These above equations are called generalized optical Bloch equations (OBE). The mentioned equations also follow the properties of the density matrix $Tr[\rho] = \rho_{11} + \rho_{22} = 1$, which indicates the conservation of the total population in the system. The Hermitian property of the density matrix suggests that two off-diagonal elements ρ_{12} and ρ_{21} satisfy the relation $\rho_{12} = \rho_{21}^*$. Applying these constraints to the optical Bloch equation, we can reduce the number of equations and variables into two, which is solvable. At first, we consider an ideal system where the spontaneous decay rate $\gamma = 0$. In that case, the system of equations $(1.129 - 1.132)$ forms an exactly solvable system. The analytical solution of the density matrix elements with initial condition $\rho_{22}(t = 0) = 1$ is given by

$$\rho_{12}(t) = \frac{2\Omega}{\Omega_G^2} \sin\left(\frac{\Omega_G t}{2}\right) \left\{ \Delta \sin\left(\frac{\Omega_G t}{2}\right) + i\Omega_G \cos\left(\frac{\Omega_G t}{2}\right) \right\} \tag{1.133}$$

$$\rho_{22}(t) = \cos^2\left(\frac{\Omega_G t}{2}\right) + \frac{\Delta^2}{\Omega_G^2} \sin^2\left(\frac{\Omega_G t}{2}\right), \tag{1.134}$$

where $\Omega_G = \sqrt{\Delta^2 + 4\Omega^2}$ is called the generalized Rabi frequency. In Fig. 1.9, we have plotted both the ground and excited state population of a two-level system with time.

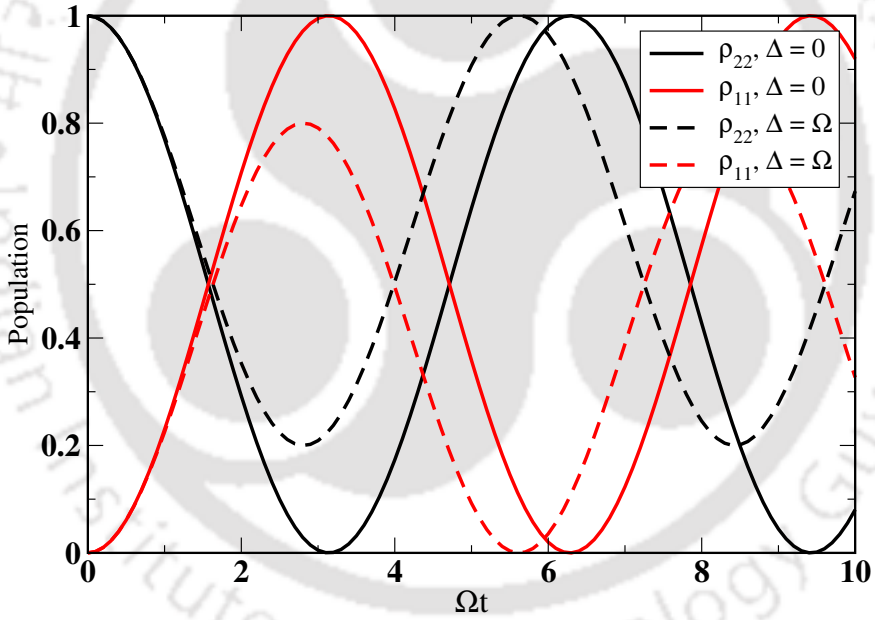

Figure 1.9: The populations of a two-level QD system plotted as a function of dimensionless time for two different detunings $\Delta = 0, \Omega$. The ground and excited state populations display Rabi oscillations, with a reduced peak value for larger detuning.

We observed that for $\Delta = 0$, the population shows a Rabi oscillation between ground and excited state with frequency Ω. The complete population transfer from zero to one has occurred in this case. Contrarily, for $\Delta = \Omega$, the population oscillation increases along with the reduction in the population peak. From Fig. 1.9, we notice that the sum of the ground and excited state population is always conserved and equal to unity. Now, we incorporate the spontaneous emission rate by considering $\gamma \neq 0$ in the generalized OBE. Therefore, the system dynamics become more realistic, unlike the previous case where the excited state does not decay arbitrarily long. After this consideration, the density matrix equations do not have any general analytical

solution. Therefore, we solved the system of first-order coupled differential equations numerically. Fig. 1.10 shows the variation of the population of a two-level system by considering the spontaneous decay rate γ. Due to a spontaneous decay rate, the excited state no longer reaches the maximum population after some time. Also, the Rabi frequency shows a damping nature; after a long time, the population reaches a steady state value. These findings match very well with the experimentally observed results in atomic systems.

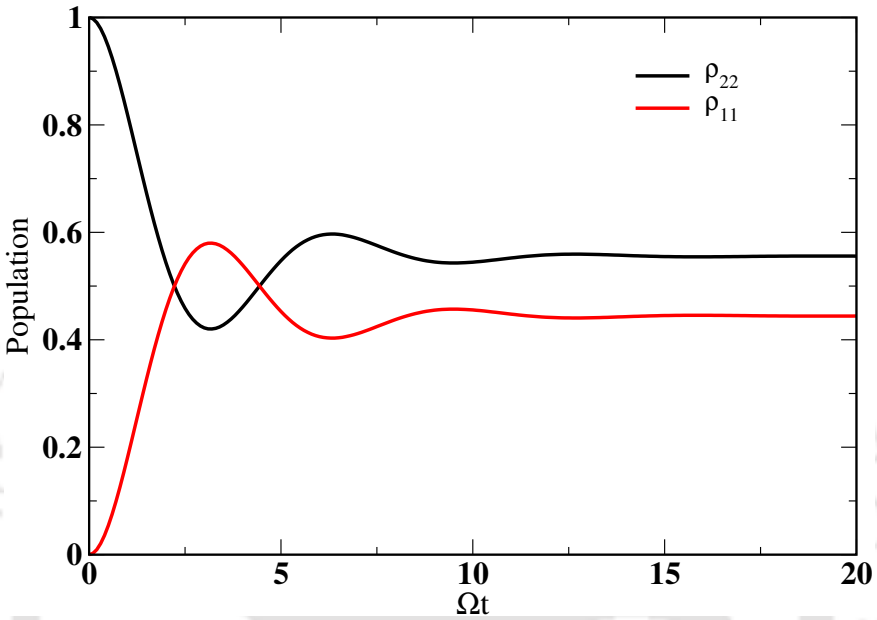

Figure 1.10: Variation of two-level QD populations with dimensionless time for detuning $\Delta = 0$ in the presence of spontaneous decay rate $\gamma = \Omega$.

1.5.4 Steady-state solution

In the previous subsection, we noticed that the population undergoes a steady state behavior after a long time in the presence of a spontaneous decay rate. Therefore, we are interested in studying the steady-state solution of the density matrix equation. To do so, we have set the time derivative of the density matrix to zero, indicating that the density matrix elements are independent of time. As a result, all four equations don't have any derivative terms, transforming OBE into a set of linear equations with a simple solution. The exact analytical solution of the density matrix element by solving the set of linear equations is given by

$$\rho_{11} = \frac{|\Omega|^2}{\left(\left(\frac{\gamma}{2}\right)^2 + \Delta^2\right) + 2|\Omega|^2}, \tag{1.135}$$

$$\rho_{12} = \frac{i\Omega\left(\frac{\gamma}{2} + i\Delta\right)}{\left(\left(\frac{\gamma}{2}\right)^2 + \Delta^2\right) + 2|\Omega|^2}. \tag{1.136}$$

We found the steady-state solution of the density matrix as a function of detuning. Therefore, one can control the coherence term ρ_{12} by changing the detuning with the help of applied field frequency. Fig. 1.11 shows the variation of the real and imaginary

part of the coherence term ρ_{12} as a function of detuning Δ. Now, we will discuss the effect of the coherence on the medium's optical properties. An electromagnetic field

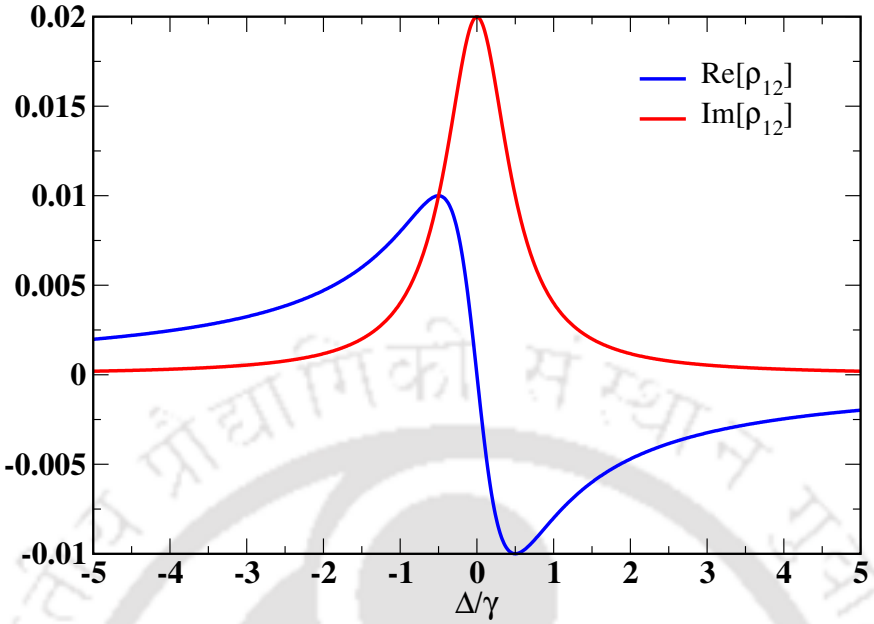

Figure 1.11: The real and imaginary part of the steady state coherence term ρ_{12} variation with the normalized detuning Δ/γ for a weak applied field $\Omega = 0.01\gamma$.

interacting with the medium produces an induced polarisation. Thus, the induced polarization is calculated by taking the average of all individual dipole moments in the system. The induced polarization of the QD medium with volume density N is given by

$$\vec{P} = N\langle\vec{d}\rangle = NTr[\vec{d}\rho] \tag{1.137}$$

$$= N(\vec{d}_{21}\rho_{12} + H.c). \tag{1.138}$$

The induced polarization obeys a relation $\vec{P} = \chi\vec{E}$ where χ is the susceptibility of the medium. Using the steady state coherence in Eq.(1.136), we can get the expression for the susceptibility of the medium as

$$\chi = \frac{N|d_{12}|^2}{\hbar}\frac{i\left(\frac{\gamma}{2} + i\Delta\right)}{\left(\left(\frac{\gamma}{2}\right)^2 + \Delta^2\right) + 2|\Omega|^2}. \tag{1.139}$$

We can see that the susceptibility of the medium depends on the higher orders of the applied field intensity, indicating the presence of nonlinearity in the system [69]. However, the system will act as a linear medium when the applied field intensity becomes very small or $|\Omega|^2 \to 0$. Fig. 1.11 effectively exhibits the behavior of the susceptibility without some constant multiplication factor. The real part of the susceptibility shows the dispersion phenomena. In the two-level system, the dispersion is anomalous. The imaginary part of the susceptibility is responsible for the absorption and gain in the system. Positive and negative signs of the imaginary part decide the absorption and gain of the system, respectively. Notably, a Lorentzian absorption peak has been observed near the resonance condition for a two-level system [70]. This absorption peak indicates a very high absorption of the applied field by the medium at resonance condition $\Delta = 0$. In Chapter 2, we will discuss how to avoid such a problem by making the system transparent at the resonance.

1.6 Pulse propagation in a medium

The Maxwell equation fully describes classical electromagnetic radiation propagation in a medium. To understand the physics, first, we recall all the relevant quantities previously defined in Eq.(1.1 − 1.4) and Eq.(1.5 − 1.6) under the subsection 1.1.1. Previously, in the case of free space, we assume that all the source terms and induced polarisations are zero. However, the electromagnetic radiation polarised the individual atoms to build up the resultant induced polarisation $\vec{P}$ for a dielectric medium. In this study, we will consider all the previous assumptions correct except for the induced electric polarisation. Now, the electric displacement vector for the dielectric medium has the additional induced polarisation term described as

$$\vec{D} = \epsilon_0 \vec{E} + \vec{P}. \tag{1.140}$$

Using all the relevant equations mentioned before, one can write down the differential equation for the electric field given by

$$\vec{\nabla} \times \left(\vec{\nabla} \times \vec{E} \right) = -\mu_0 \frac{\partial^2}{\partial t^2} \left(\epsilon_0 \vec{E} + \vec{P} \right). \tag{1.141}$$

Appling various vector identities and no bound charge condition, we can get the wave equation for the electric field with a source term expressed as

$$\nabla^2 \vec{E} - \frac{1}{c^2} \frac{\partial^2 \vec{E}}{\partial t^2} = \mu_0 \frac{\partial^2 \vec{P}}{\partial t^2}. \tag{1.142}$$

The presence of the source term in Eq.(1.142) opens up various new possibilities for studying the propagation dynamics. The wave equation can become nonlinear depending on the susceptibility behavior of the medium. In general, we could not find the exact solution of the wave equation in the presence of polarization; instead, it is possible by numerical methods. Therefore, some crucial approximations are required to get the analytical solution of the wave equation. Let's recall the electric field of a quasi-monochromatic plane wave propagating along the z-direction in Eq.(1.15)

$$\vec{E}(z,t) = \hat{e}\mathcal{E}(z,t)e^{i(kz-\omega t)} + c.c. \tag{1.143}$$

where $\hat{e}$ is the arbitrary linear polarisation. Interaction between the applied electric field and the medium changes the dipole orientation, resulting in induced polarization

$$\vec{P}(z,t) = \hat{e}\mathcal{P}(z,t)e^{i(kz-\omega t)} + c.c. \tag{1.144}$$

where $\mathcal{P}(z,t)$ is the envelope function for induced polarisation. The second derivative in space and time is calculated for the electric field and induced polarization

$$\nabla^2 \vec{E} = \hat{e} \left(\frac{\partial^2 \mathcal{E}}{\partial z^2} + 2ik \frac{\partial \mathcal{E}}{\partial z} - k^2 \mathcal{E} \right) e^{i(kz-\omega t)} + c.c., \tag{1.145}$$

$$\frac{\partial^2 \vec{E}}{\partial t^2} = \hat{e} \left(\frac{\partial^2 \mathcal{E}}{\partial t^2} - 2i\omega \frac{\partial \mathcal{E}}{\partial t} - \omega^2 \mathcal{E} \right) e^{i(kz-\omega t)} + c.c., \tag{1.146}$$

$$\frac{\partial^2 \vec{P}}{\partial t^2} = \hat{e} \left(\frac{\partial^2 \mathcal{P}}{\partial t^2} - 2i\omega \frac{\partial \mathcal{P}}{\partial t} - \omega^2 \mathcal{P} \right) e^{i(kz-\omega t)} + c.c. \tag{1.147}$$

Before plugging these parts directly into the wave equation, we make a realistic approximation to simplify the problem. We assume that the spatial and temporal variation of the envelop functions is negligible at the optical period and wavelength scale. This approximation holds very well for the optical to infrared wavelength range. We can express the approximation mathematically by considering smaller values for higher-order derivatives as

$$\left|\frac{\partial^2 \mathcal{E}}{\partial z^2}\right| \ll \left|k\frac{\partial \mathcal{E}}{\partial z}\right| \ll \left|k^2 \mathcal{E}\right| \tag{1.148}$$

$$\left|\frac{\partial^2 \mathcal{E}}{\partial t^2}\right| \ll \left|\omega\frac{\partial \mathcal{E}}{\partial t}\right| \ll \left|\omega^2 \mathcal{E}\right| \tag{1.149}$$

$$\left|\frac{\partial^2 \mathcal{P}}{\partial t^2}\right| \ll \left|\omega\frac{\partial \mathcal{P}}{\partial t}\right| \ll \left|\omega^2 \mathcal{P}\right|. \tag{1.150}$$

By putting Eq.$(1.145 - 1.147)$ in Eq.(1.142), we get the explicit differential form of the wave equation. Neglecting the second-order derivative terms of the electric field and both first and second-order derivative terms of the polarization, we can get the simplified propagation equation as

$$\frac{\partial \mathcal{E}}{\partial z} + \frac{1}{c}\frac{\partial \mathcal{E}}{\partial t} = \frac{i\mu_0 \omega c}{2}\mathcal{P}, \tag{1.151}$$

by using the linear dispersion relation $\omega = ck$. The above approximation is popularly known as the slowly varying envelop approximation (SVEA) in the literature [35]. Under the SVEA approximation, the propagation equation transforms into a simpler form and is easy to solve analytically and numerically. This equation itself is insufficient to get a practical system's complete dynamics. The induced polarisation should be calculated from OBE under the density matrix formalism discussed earlier. The propagation of the applied pulse depends on the real and imaginary parts of the susceptibility present in the polarization. The medium's property indirectly depends on the coherence term ρ_{12} as the induced polarisation is proportional to it. The system is now solvable "self-consistently" because the applied pulse produces induced polarisation, then the medium changes the propagating pulse and completes the cycle. Further simplification of the propagation equation (1.151) is done by introducing a new frame of reference moving with the speed of light c. The transformation rule between old coordinates (z, t) and the new coordinates (ζ, τ) are defined by

$$\zeta = z, \qquad \tau = t - \frac{z}{c} \tag{1.152}$$

so that

$$\frac{\partial}{\partial z} + \frac{1}{c}\frac{\partial}{\partial t} = \frac{\partial}{\partial \zeta}, \qquad \frac{\partial}{\partial t} = \frac{\partial}{\partial \tau}. \tag{1.153}$$

In the new frame, the transformed propagation equation takes the form

$$\frac{\partial \mathcal{E}}{\partial \zeta} = \frac{i\mu_0 \omega c}{2}\mathcal{P}. \tag{1.154}$$

We will use the above propagation equation for the rest of my thesis to numerically calculate the pulse propagation dynamics with the help of an iterative method. The calculation process starts at $\zeta = 0$ with the initial assumption and finds the next solution point. In the next iteration, the previously solved point is taken as an initial condition to find the next point. The step size of the iteration process plays a crucial role in getting reliable results.

1.7 Four-wave mixing

This section discusses the basic understanding of various nonlinear optical phenomena. The nonlinear optical phenomena occurred due to the medium's nonlinear susceptibility [69]. The polarization of a medium depends on the coherence term of the density matrix; hence, it is possible to manipulate the susceptibility of the medium. In general, the polarisation density of the medium depends on the electric field, as given below

$$P(t) = \epsilon_0 \left(\chi^{(1)} E(t) + \chi^{(2)} E^2(t) + \chi^{(3)} E^3(t) + \cdots \right). \tag{1.155}$$

In the above equation, the first term describes the linear optical process as the polarization is proportional to the first power of the electric field. The proportionality constant $\chi^{(1)}$ refers to the linear susceptibility of the medium. For a linear medium, all the higher-order susceptibility terms are zero. Therefore, polarization satisfies the relation $\vec{P} = \chi^{(1)} \vec{E}$. By putting this relation into the modified wave equation (1.142), we can get a wave equation similar to the free space with modified propagation velocity v. This modified velocity is determined by the medium's refractive index n as $v = c/n$. Alternatively, the relationship between susceptibility and the refractive index obeys the relation $n = \sqrt{1 + \chi^{(1)}}$. We see that a linear medium can only change the speed of the light compared to free space. Much more interesting optical phenomena occurred when the nonlinear terms in Eq. (1.155) were present in the system. The second and third terms correspond to the second and third-order nonlinear susceptibility defined by $\chi^{(2)}$ and $\chi^{(3)}$ respectively. Keep in mind that the higher-order susceptibility of the medium exhibits weaker strength. Therefore, the ordering of the susceptibility according to their strength is as follows: $\chi^{(1)} > \chi^{(2)} > \chi^{(3)} > \cdots$. We can neglect the higher-order susceptibility for weak applied electric fields. In the case of a strongly applied electric field, nonlinearity comes into the picture. Another way to observe the nonlinear effect is to take a medium whose lower-order susceptibility is almost negligible. Let us consider the applied electric field amplitude,

$$E(t) = \mathcal{E} e^{-i\omega t} + c.c. \tag{1.156}$$

Then, the second-order polarization term is written as

$$P^{(2)}(t) = \epsilon_0 \chi^{(2)} E^2(t) \tag{1.157}$$

$$= 2\epsilon_0 \chi^{(2)} |\mathcal{E}|^2 + \left(\epsilon_0 \chi^{(2)} \mathcal{E}^2 e^{-2i\omega t} + c.c. \right). \tag{1.158}$$

We notice that the second-order polarization contribution in Eq.(1.158) explicitly shows the first term corresponds to the zero frequency, and the second term is associated with 2ω frequency. Therefore, the constant term will be zero after the second-order time derivative in the propagation equation and hence does not contribute to the new harmonic generation. Notably, the first term produces a static electric field across the medium, and the process is called optical rectification. On the other hand, the second term indicates the second harmonic generation as the new frequency is twice the applied field frequency [71]. The generated new positive frequency can have all possible combinations given by $\omega_n = \pm\omega \pm \omega = \{0, 2\omega\}$. Now, we study the second-order nonlinear process with two electric fields having different frequencies ω_1 and ω_2. The total electric field for the two frequency components is defined as

$$E(t) = \mathcal{E}_1 e^{-i\omega_1 t} + \mathcal{E}_2 e^{-i\omega_2 t} + c.c. \tag{1.159}$$

Again, using the expression for second-order nonlinear polarization in Eq.(1.155) we can get

$$P^{(2)}(t) = \epsilon_0 \chi^{(2)} E^2(t) \tag{1.160}$$

$$= 2\epsilon_0 \chi^{(2)}(|\mathcal{E}_1|^2 + |\mathcal{E}_2|^2) + \epsilon_0 \chi^{(2)}\Big(\mathcal{E}_1^2 e^{-2i\omega_1 t} + \mathcal{E}_2^2 e^{-2i\omega_2 t} + 2\mathcal{E}_1\mathcal{E}_2 e^{-i(\omega_1+\omega_2)t} + 2\mathcal{E}_1\mathcal{E}_2^* e^{-i(\omega_1-\omega_2)t} + c.c.\Big). \tag{1.161}$$

In this case, four new positive frequency generations are possible via a second-order nonlinear process; those are $\omega_n = \pm\omega_1 \pm \omega_2 = \{0, 2\omega_1, 2\omega_2, \omega_1 + \omega_2, \omega_1 - \omega_2\}$. Every frequency generation in the second bracket undergoes some unique physical process and is, therefore, named accordingly. The process involved in the second and third frequency terms of the second bracket is called a second-harmonic generation (SHG), the fourth frequency represents the sum-frequency generation (SFG), and the final frequency term indicates difference-frequency generation (DFG). These three processes have many applications, such as frequency converters, ultra-short pulse measurements, and high-resolution optical microscopy. In the above discussion, we have understood the second-order nonlinear optical process associated with the nonlinear susceptibility of the medium. We go one step further to understand third-order nonlinear optical processes coming from third-order nonlinear susceptibility in the medium. Similar to the previous calculation, we consider an electric field with three frequency components given by

$$E(t) = \mathcal{E}_1 e^{-i\omega_1 t} + \mathcal{E}_2 e^{-i\omega_2 t} + \mathcal{E}_3 e^{-i\omega_3 t} + c.c. \tag{1.162}$$

The third-order contribution of the polarization is written in terms of the electric field as

$$P^{(3)}(t) = \epsilon_0 \chi^{(3)} E^3(t). \tag{1.163}$$

From Eq.(1.163), we understand that the right-hand side cubic term can be expanded by putting some effort. Here, we will not present the explicit form of the polarisation as it will have lots of new frequency terms. However, the new positive frequency terms [71] calculated from the above equation are given by

$$\omega_n = \Big\{\omega_1, \omega_2, \omega_3, 3\omega_1, 3\omega_2, 3\omega_3, (\omega_1 + \omega_2 + \omega_3), (\omega_1 + \omega_2 - \omega_3), (\omega_1 + \omega_3 - \omega_2), (\omega_2 + \omega_3 - \omega_1), (2\omega_1 \pm \omega_2), (2\omega_1 \pm \omega_3), (2\omega_2 \pm \omega_1), (2\omega_2 \pm \omega_3), (2\omega_3 \pm \omega_1), (2\omega_3 \pm \omega_2)\Big\}. \tag{1.164}$$

Although many frequency generations are possible in a third-order nonlinear medium, all these can not be found simultaneously at the medium end. In this regard, no more than one frequency could have appreciable intensity generated from the third-order nonlinear optical interaction. Obtaining a particular frequency harmonic in the system is closely connected with obeying some specific condition. Usually, the condition does not obey simultaneously for more than one frequency of the nonlinear polarization. The mentioned condition is the energy and momentum conservation in the process, which must be satisfied to generate particular harmonics. In general, any nonlinear optical process is often referred to as an N-wave mixing process where

N number of photons are involved, including the emitted one. Therefore, the SHG doubling the applied frequency in a second-order nonlinear medium is a three-wave mixing process. In this manner, when three applied fields interact with the third-order nonlinear medium to produce a fourth electric field with a new frequency, such method is called four-wave mixing [72–74]. Let's consider a four-level QD system to understand the condition of new harmonic generation via a four-wave mixing process in the presence of third-order nonlinear susceptibility.

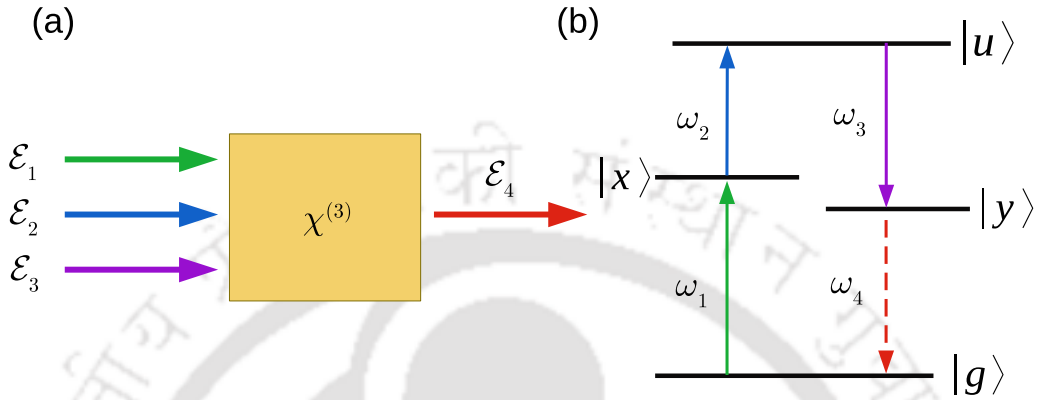

Figure 1.12: (a) Schematic diagram of the system of three electric fields interacting with the third-order nonlinear medium to generate an FWM field with a new frequency. (b) Energy conservation of the FWM process inside the four-level QD medium. All the solid lines represent the applied field, and the dashed line indicates the generated FWM field with the mentioned frequency.

In Fig. 1.12(a) and (b), we have displayed the generation of a new field inside a nonlinear medium by applying three fields and the energy level diagram of the medium, respectively. First, consider that the frequency and wave vector of the four electric fields is ω_i and $\vec{k}_i$ respectively, where $i \in \{1, 2, 3, 4\}$. According to the energy conservation principle for the multiphoton process, we get

$$\omega_4 = \omega_1 + \omega_2 - \omega_3. \tag{1.165}$$

Another essential requirement for observing the FWM process is the conservation of the momentum in the process, which obeys the relation

$$\vec{k}_4 = \vec{k}_1 + \vec{k}_2 - \vec{k}_3. \tag{1.166}$$

These above-stated conditions are commonly called phase-matching conditions [75]. Subsequently, a precise phase-matching condition must be satisfied to observe efficient FWM signal generation. Under the current consideration, third-order polarisation dependency on the electric field components in the frequency domain is given below

$$P(\omega_1 + \omega_2 - \omega_3) = 6\epsilon_0 \chi^{(3)} \mathcal{E}_1 \mathcal{E}_2 \mathcal{E}_3^*. \tag{1.167}$$

In a similar level system with two degenerate exciton states, Hsu et al. calculated the analytical form of the light propagation by solving both the OBE and propagation equation simultaneously. In this work, they obtain the contribution from the first and third-order nonlinearity and named two-level absorption and ladder transparency, respectively. Interestingly, the $\chi^{(3)}$ term contributed in the generated field depends on the electric field as

$$\mathcal{E}_4 \propto \mathcal{E}_1 \mathcal{E}_2 \mathcal{E}_3^*. \tag{1.168}$$

We notice that the right-hand side of Eq. (1.167) and (1.168) show similar structure. In Chapter 3, we will apply the FWM process to generate the vector beams.

1.8 Basic theory of vector beams

This section discusses the fundamental theory of vector beams and their origin. Again, we start with the Maxwell equation in free space, but this time, the variation of the transverse component of the electric field is not considered to be zero. Therefore, we are now deviating from the earlier-mentioned SVEA approximation and will discuss the new approximation in this section in detail. Then, we solve the Maxwell equation to get a light that can carry the orbital angular momentum having a vortex structure in the transverse intensity distribution. Such OAM-carrying beams originate from the phase singularity. Finally, we can generate the vector beams by vector superposition of these OAM-carrying lights with orthogonal polarisation. The resultant light shows an inhomogeneous polarisation distribution with polarisation singularity.

1.8.1 Laguerre-Gaussian mode

The Maxwell equation in free space (1.13) written in the cartesian coordinates is given by

$$\left(\frac{\partial^2}{\partial x^2}+\frac{\partial^2}{\partial y^2}+\frac{\partial^2}{\partial z^2}\right)\vec{E}-\frac{1}{c^2}\frac{\partial^2\vec{E}}{\partial t^2}=0. \tag{1.169}$$

By considering the general form of the electric field in the free space as

$$\vec{E}(x,y,z,t)=\hat{e}\mathcal{E}(x,y,z,t)e^{i(kz-\omega t)}+c.c., \tag{1.170}$$

we find all the spatial and temporal derivatives of the electric fields as mentioned in Eq.$(1.145-1.146)$. An optical field is said to be a beam when the intensity varies in the transverse spatial direction but is independent in time. To satisfy the condition for a beam, we make some new assumptions, which are

$$\left|\frac{\partial^2\mathcal{E}}{\partial z^2}\right|\ll\left|\frac{\partial^2\mathcal{E}}{\partial x^2}\right|,\left|\frac{\partial^2\mathcal{E}}{\partial y^2}\right|,\left|k\frac{\partial\mathcal{E}}{\partial z}\right|. \tag{1.171}$$

This approximation states that variation of the electric field envelope function $\mathcal{E}(x,y,z)$ along the z- direction is negligible compared to the transverse direction (x,y). The approximation displayed in Eq.(1.171) is called the paraxial wave approximation [76]. Applying these conditions in the wave equation, we can get the new propagation equation as

$$\frac{\partial^2\mathcal{E}}{\partial x^2}+\frac{\partial^2\mathcal{E}}{\partial y^2}+2ik\frac{\partial\mathcal{E}}{\partial z}=0. \tag{1.172}$$

The above propagation equation offers a solution with an infinite set of functions individually called modes. The solution can also vary depending on the coordinate system chosen to solve the problem. For the Cartesian coordinate system, the solution of the Eq.(1.172) gives Hermite-Gaussian modes. Subsequently, the zeroth mode of the Hermite-Gaussian solution exhibits the well-known Gaussian intensity distribution.

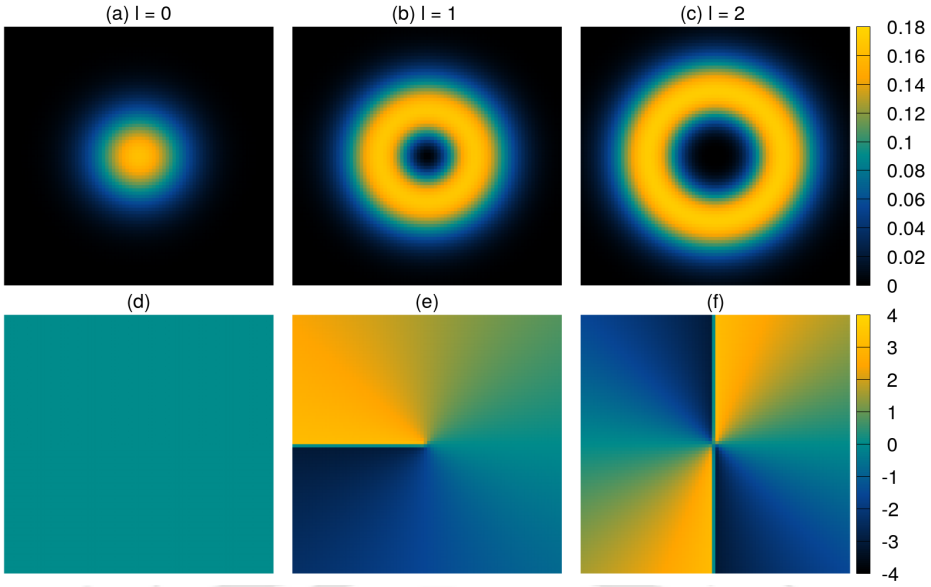

Figure 1.13: (a)-(c) Intensity plot of the Laguerre-Gaussian modes with $l = 0, 1, 2$ in the transverse plane. (d)-(f) Phase plot of the considered Laguerre-Gaussian modes. The bright and dark colors represent high and low intensity or phase, respectively.

Instead of taking the Cartesian coordinates, it is possible to write the propagation equation in cylindrical polar coordinates. The mathematical form of the propagation equation in cylindrical polar coordinates (r, ϕ, z) is given by

$$\frac{1}{r}\frac{\partial}{\partial r}\left(r\frac{\partial \mathcal{E}}{\partial r}\right) + \frac{1}{r^2}\frac{\partial^2 \mathcal{E}}{\partial \phi^2} + 2ik\frac{\partial \mathcal{E}}{\partial z} = 0. \tag{1.173}$$

The beam propagation equation in cylindrical polar coordinates satisfies the Laguerre-Gaussian modes, which are described as

$$\mathcal{E}(r,\phi,z) = \mathcal{E}_0\sqrt{\frac{2m!}{\pi(m+|l_i|)!}}\frac{w_0}{w(z)}\left(\frac{r\sqrt{2}}{w(z)}\right)^{|l|}\exp\left[-\frac{r^2}{w^2(z)}\right]L_m^l\left[\frac{2r^2}{w(z)^2}\right]e^{il\phi}$$
$$\times\exp\left[\frac{ikr^2z}{2\left(z^2+z_R^2\right)}\right]\exp\left[-i(2m+|l|+1)\eta(z)\right]. \tag{1.174}$$

Used notations are the maximum field amplitude $\mathcal{E}_0$, integer numbers l, m, azimuthal angle ϕ, Rayleigh length $z_R = kw_0^2/2$, beam waist w_0, wave number k, beam waist at z distance $w(z) = w_0\sqrt{1+z^2/z_R^2}$, Gouy phase $(2m+|l|+1)\eta(z)$ where $\eta(z) = \tan^{-1}(z/z_R)$ [76].

Next, we will understand the properties of the Laguerre-Gaussian modes and the corresponding transverse intensity distributions. To minimize the complexity of the problem, we have chosen $m = 0$ throughout the thesis. In Fig. 1.13, we have plotted the intensity and phase distribution in a transverse plane for the first three values of l. The intensity distribution shows a Gaussian distribution for $l = 0$ and a vortex structure for $l \neq 0$. The vortex radius increases with the increasing l value. Also, the phase plot displays an equal number of maxima and minima same as the binding number l. This observation ensures the plotted LG modes have the binding number $l = 0, 1, 2$. From the intensity distribution, we can observe that the intensity is zero at the center

for $l \neq 0$, thus representing a phase singularity [77]. Generally, a beam exhibiting phase singularity refers to having the orbital angular momentum. By looking at the Eq.(1.174), we can understand that the $e^{il\phi}$ term is responsible for the OAM of an optical field [78]. The quantum mechanical operator for the z-component of OAM is described by $L_z = -i\hbar\frac{\partial}{\partial\phi}$ in cylindrical polar coordinates. In a crude approximation, if the envelop wavefunction of the light has a similar structure to LG beams, the OAM of the considered light would be the $l\hbar$ [79]. Finally, we have understood that, among many other properties, light can also carry orbital angular momentum. It is clear that LG modes are one such OAM carrying light beam having OAM same as the integer index of Laguerre polynomial l.

1.8.2 Vector beams

To this point, we always consider the light with constant polarisation denoted by the $\hat{e}$. Therefore, the polarisation at each point of a light beam in the transverse plane is exactly the same. This particular type of light is called a scalar beam due to its homogeneous polarisation distribution. The previous subsection shows that the LG modes can produce inhomogeneous intensity distribution in the transverse plane with constant polarization. The question arises: What will happen when two light beams with inhomogeneous intensity distribution and orthogonal polarization are vectorially superimposed? To address this question, we choose a circular polarisation basis of the light with two orthogonal polarisation directions named left and right circular polarisation $\hat{e}_L$ and $\hat{e}_R$ respectively. The resultant electric field of the two superimposed LG beams is given by

$$\vec{E}(r,\phi,z) = \mathcal{E}_L(r,\phi,z)\hat{e}_L + \mathcal{E}_R(r,\phi,z)\hat{e}_R, \tag{1.175}$$

where

$$\mathcal{E}_L(r,\phi,z) = \cos(\alpha)LG_0^{l_L}, \text{ and } \mathcal{E}_R(r,\phi,z) = e^{i\theta}\sin(\alpha)LG_0^{l_R}, \tag{1.176}$$

are the Laguerre- Gaussian modes with two controlling parameters, α and θ, known as relative amplitude and phase. In the literature, various investigations suggest that the light mentioned above has a unique property of heterogeneous polarization distribution in the transverse plane. The newly generated light has a unique polarisation vector direction in the different coordinate points in the xy plane, denoted as vector beam (VB). The characteristics of a vector beam are mainly defined by four controlling parameters: each component OAM l_L, l_R, relative strength α, and phase θ. Depending on the OAM of the VB components, they are classified into two groups: (a) full Poincaré (FP) beams and (b) cylindrical vector (CV) beams. A VB with one zero and non-zero OAM index of the LG mode component is called a full Poincaré (FP) beam [80]. Examples of such beams are lemon, star, and web VBs. These VBs can be generated by varying OAM indexes. Such VBs always carry a net OAM. In contrast, when a VB has an equal and opposite OAM index of LG components, those are called cylindrical vector (CV) beams [81]. Some examples of such VBs are radial, spiral, and azimuthal VBs according to their displayed polarization symmetry. In this case, these beams can be generated by varying the relative phase θ. Due to the equal and opposite OAM components, the net total OAM carried by the CV beams is always zero. Let us understand the polarisation distribution of a lemon VB by generating it from the

two scalar beams. Before studying the polarization distribution of a VB, we need to know an important tool called Stokes parameters. The Stokes parameters are excellent alternatives for defining a general polarisation state of incoherent or partially polarised light. We adopted the Stokes parameter formalism in the circular polarization basis to visualize the polarization distribution in a transverse plane given by

$$\begin{aligned} S_0 &= |\mathcal{E}_L|^2 + |\mathcal{E}_R|^2,\ S_1 = 2\mathrm{Re}[\mathcal{E}_L^* \mathcal{E}_R], \\ S_2 &= 2\mathrm{Im}[\mathcal{E}_L^* \mathcal{E}_R], \quad S_3 = |\mathcal{E}_L|^2 - |\mathcal{E}_R|^2. \end{aligned} \tag{1.177}$$

With the help of Stokes parameters, the ellipticity χ and orientation ψ of the degree of polarization at any given point can be calculated as follows

$$\frac{S_1}{S_0} = \cos(2\chi)\cos(2\psi), \frac{S_2}{S_0} = \cos(2\chi)\sin(2\psi), \frac{S_3}{S_0} = \sin(2\chi). \tag{1.178}$$

We can derive the expression for ellipticity χ and orientation ψ in terms of the stokes parameters by using Eq.(1.177) and Eq.(1.178) and are given by

$$\chi = \frac{1}{2}\sin^{-1}\left(\frac{S_3}{S_0}\right) = \frac{1}{2}\sin^{-1}\left(\frac{|\mathcal{E}_L|^2 - |\mathcal{E}_R|^2}{|\mathcal{E}_L|^2 + |\mathcal{E}_R|^2}\right), \tag{1.179}$$

$$\psi = \frac{1}{2}\tan^{-1}\left(\frac{S_2}{S_1}\right) = \frac{1}{2}\tan^{-1}\left(\frac{Im[\mathcal{E}_L^* \mathcal{E}_R]}{Re[\mathcal{E}_L^* \mathcal{E}_R]}\right). \tag{1.180}$$

Now, we are at that point to plot both the intensity and polarization in a transverse plane by calculating the Stokes parameters and the various polarisation ellipse parameters. In Fig. 1.14, we have displayed the generation of a lemon vector beam from the two orthogonally polarised scalar beams, with one having non-zero OAM. This figure

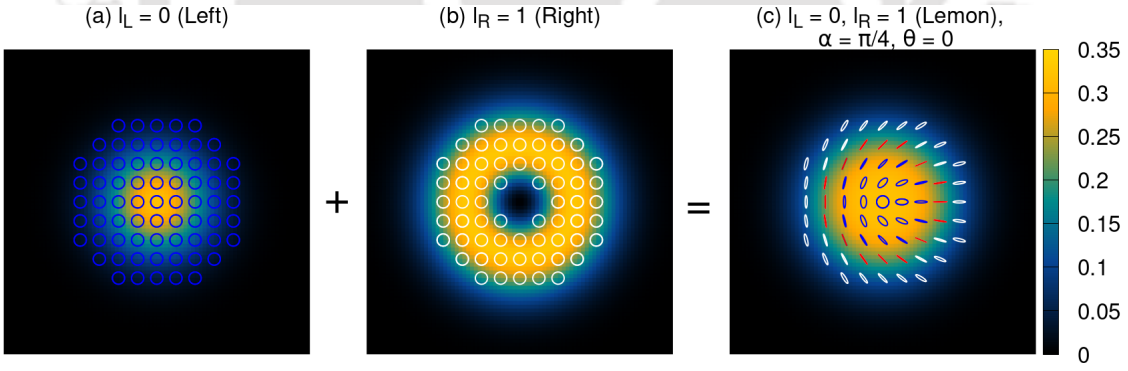

Figure 1.14: The intensity and polarisation distribution of three light beams plotted in xy-plane. (a)The left circularly polarised light with no OAM $l_L = 0$. (b) The right circularly polarised light carrying OAM $l_R = 1$. (c) Generated lemon VB with the parameters $l_L = 0, l_R = 1, \alpha = \pi/4, \theta = 0$. In this figure, blue, white, and red color ellipses represent the left, right, and linear polarisation, respectively.

shows that the left circular polarization component has a Gaussian intensity distribution, and the right circular polarization shows a doughnut intensity distribution. Both the components displayed orthogonal polarisation components exhibiting left (blue) and right (white) circular polarisation. The resultant intensity distribution exhibits a flat-top Gaussian intensity distribution. The generated vector beams display left circular polarisation at the center, linear polarisation in the middle, and right circular

polarisation at the edge. Therefore, the polarisation distribution becomes heterogeneous, as stated earlier. Similar to the phase singularity, lemon VB poses polarisation singularity. At the center, the state of polarisation is circular, which indicates that the direction of the polarisation is undefined. There are also some classifications of the polarisation singularity in the literature. Those are C- and V-point singularities extensively studied by Ruchi et al.[77]. The name " lemon " is considered for this VB because of the polarization distribution pattern itself. More details of arbitrary vector beam generation techniques will discussed in Chapter 3.

1.9 Quantum theory of laser

The first experimental demonstration of a working laser was invented by T. Maiman in 1960 [18]. A conventional laser system consists of a high-quality optical cavity resonator filled with active material called gain medium. There are several methods for pumping the atoms into the excited states. The optical amplification occurs inside active material due to the stimulated emission of electromagnetic radiation. In this process, the population of the excited state goes to the ground state coherently by emitting one additional photon in the cavity mode. Then, the photons inside the cavity travel back and forth between the mirrors to produce a very high output intensity. The input power of a laser is a critical quantity to start lasing action; the minimum operating power of a laser is called laser threshold power. To this point, we have only studied the semiclassical light-matter interaction model where the light was considered classical. This section discusses the complete quantum theory of light-matter interaction. Accordingly, we should first understand the Jaynes Cummings model to study the laser dynamics quantum mechanically.

1.9.1 Jaynes Cummings model

The Jaynes Cummings model [82] is a fully quantum mechanical version of the previously discussed Rabi model. This model considers the simplest possible system of a two-level emitter interacting with the quantized electromagnetic radiation in a single-mode cavity. Let us consider that the two-level emitter has ground state $|g\rangle$ and excited state $|e\rangle$. Subsection 1.1.2 has already discussed the quantized electromagnetic radiation. Therefore, the electric field of a single-mode cavity is given by

$$\vec{E}(z,t) = \hat{e}\mathcal{E}_0(a + a^\dagger)\sin(kz). \tag{1.181}$$

We have considered the energy eigenfrequency of the ground state to be zero. The operator $\sigma_{i,j} = |i\rangle\langle j|$ represents the emiters transition where $i, j \in \{g, e\}$. According to the previous definition, the dipole moment could be written in terms of the emitter operators as

$$\vec{d} = d|g\rangle\langle e| + d^*|e\rangle\langle g| = d\sigma_{ge} + d^*\sigma_{eg} = d\left(\sigma_{ge} + \sigma_{eg}\right), \tag{1.182}$$

where we assumed that the dipole moment is real and the diagonal terms are zero due to the parity selection rule. Recalling the previously established radiation matter interaction Hamiltonian, we get,

$$H_I = -\vec{d}\cdot\vec{E} \tag{1.183}$$

$$= \hbar g\left(\sigma_{ge} + \sigma_{ge}\right)\left(a + a^\dagger\right), \tag{1.184}$$

where $g = -\frac{\mathcal{E}_0 d}{\hbar}\sin(kz)$ is the coupling constant. From Eq.(1.184), we understand that two terms do not satisfy the energy conservation principle among the four possible terms. Therefore, neglecting those terms from the interaction Hamiltonian, we found

$$H_I = \hbar g\left(\sigma_{eg}a + \sigma_{ge}a^\dagger\right). \tag{1.185}$$

We have also derived the free Hamiltonian for both the quantized light and the matter, so the total Hamiltonian is given by

$$H = \hbar\omega_{QD}\sigma_{ee} + \hbar\omega a^\dagger a + \hbar g\left(\sigma_{eg}a + \sigma_{ge}a^\dagger\right). \tag{1.186}$$

In this Hamiltonian, interaction term operator structure only allows two types of transition $|e\rangle|n\rangle \leftrightarrow |g\rangle|n+1\rangle$ or $|e\rangle|n-1\rangle \leftrightarrow |g\rangle|n\rangle$, where $|n\rangle$ represent number states. These composite states are identified as bare states in the literature. Therefore, for a particular detuning, Δ Hamiltonian can be diagonalized in the $|e,n\rangle$, $|g,n+1\rangle$ basis. The eigenfunctions of the mentioned Hamiltonian are given by

$$|+,n\rangle = \cos\theta_n|e,n\rangle + \sin\theta_n|g,n+1\rangle, \tag{1.187}$$
$$|-,n\rangle = \cos\theta_n|g,n+1\rangle - \sin\theta_n|e,n\rangle, \tag{1.188}$$

where $\tan 2\theta_n = 2g\sqrt{n+1}/\Delta$. The corresponding eigenvalues are

$$E_{\pm,n} = \hbar\omega(n+1) \pm \hbar\Omega_n/2; \Omega_n = \sqrt{\Delta^2 + 4g^2(n+1)}. \tag{1.189}$$

These newly generated states $|\pm,n\rangle$ are called dressed states. After studying the JC model, we are ready to develop the master equation for a laser and its corresponding rate equation.

1.9.2 Laser rate equation

Let us consider a multilevel laser system [35] with two levels coupled to the single mode cavity with a coupling constant g. The cavity decay rate is κ. For simplicity, we consider the detuning to be zero, meaning the QD and cavity are in resonance. Further, we assume the population is getting pumped to the excited state $|e\rangle$ with a rate η. Also, the decay rate of the two levels is the same, denoted by γ. The density matrix of the system after taking the trace over all the QD states is given by

$$\dot{\rho}_{n,n'} = \frac{1}{i\hbar}Tr_{QD}[H,\rho]_{n,n'} + (\mathcal{L}[a]\rho)_{n,n'}, \tag{1.190}$$

where

$$(\mathcal{L}[a]\rho)_{n,n'} = -\frac{\kappa}{2}(n+n')\rho_{n,n'} + \kappa\sqrt{(n+1)(n'+1)}\rho_{n+1,n'+1}. \tag{1.191}$$

Expanding the Tr_{QD} in Eq. (1.190), the explicit form of the density matrix equation is written as

$$\dot{\rho}_{nn'} = \frac{1}{i\hbar}\big(H_{en,gn+1}\rho_{gn+1,en'} - \rho_{en,gn'+1}H_{gn'+1,en'} + H_{gn,en-1}\rho_{en-1,gn'}$$
$$-\rho_{gn,en'-1}H_{en'-1,gn'}\big) - \frac{\kappa}{2}(n+n')\rho_{n,n'} + \kappa\sqrt{(n+1)(n'+1)}\rho_{n+1,n'+1}. \tag{1.192}$$

The elements of the JC Hamiltonian are given by

$$H_{en,gn+1} = \hbar g\sqrt{n+1} \tag{1.193}$$

$$H_{gn'+1,en'} = \hbar g\sqrt{n'+1} \tag{1.194}$$

$$H_{gn,en-1} = \hbar g\sqrt{n} \tag{1.195}$$

$$H_{en'-1,gn'} = \hbar g\sqrt{n'}. \tag{1.196}$$

As we know, all the Hamiltonian elements, the unknown element left in the reduced density matrix equation, is $\rho_{\alpha n,\beta n'} = \langle \alpha n|\rho|\beta n^{'}\rangle$. The solution of the coupled density matrix equation of the complete system can provide the unknown quantity. In this system, all the off-diagonal density matrix elements can be written analytically in terms of the diagonal elements using the matrix method as depicted in the quantum optics book by M. O. Scully and M. S. Zubairy [35]. After solving the density matrix elements using adiabatic approximation, we get

$$\rho_{en,gn'+1} = \frac{i\eta g\sqrt{n'+1}}{M}[g^2(n^{'}-n)\gamma^2]\rho_{nn'}, \tag{1.197}$$

$$\rho_{gn+1,en'} = \frac{-i\eta g\sqrt{n+1}}{M}[g^2(n-n^{'})\gamma^2]\rho_{nn'} \tag{1.198}$$

with

$$M = \gamma^4 + 2g^2\gamma^2(n+1+n^{'}+1) + g^4(n-n^{'})^2. \tag{1.199}$$

The other density matrix elements $\rho_{en-1,gn'}$ and $\rho_{gn,en'-1}$ can be determined from the the Eq.(1.197) and Eq.(1.198), by replacing the index $n, n^{'}$ to $n-1, n^{'}-1$. Plugging all the unknowns into Eq.(1.192), we get the final density matrix equation with all the diagonal terms

$$\dot{\rho}_{n,n'} = -\left(\frac{\mathscr{N}^{'}_{nn'}\mathscr{A}}{1+\mathscr{N}_{nn'}\mathscr{B}/\mathscr{A}}\right)\rho_{n,n'} \tag{1.200}$$

$$+\left(\frac{\sqrt{nn'}\mathscr{A}}{1+\mathscr{N}_{n-1,n'-1}\mathscr{B}/\mathscr{A}}\right)\rho_{n-1,n'-1} \tag{1.201}$$

$$-\frac{\kappa}{2}(n+n^{'})\rho_{n,n'} + \kappa\sqrt{(n+1)(n'+1)}\rho_{n+1,n'+1}. \tag{1.202}$$

where the linear gain coefficient

$$\mathscr{A} = \frac{2\eta g^2}{\gamma^2}, \tag{1.203}$$

the self-saturation coefficient

$$\mathscr{B} = \frac{4g^2}{\gamma^2}\mathscr{A}, \tag{1.204}$$

and the dimensionless factors

$$\mathscr{N}^{'}_{nn'} = \frac{1}{2}(n+1+n^{'}+1) + \frac{(n-n^{'})^2\mathscr{B}}{8\mathscr{A}}, \tag{1.205}$$

$$\mathscr{N}_{nn'} = \frac{1}{2}(n+1+n^{'}+1) + \frac{(n-n^{'})^2\mathscr{B}}{16\mathscr{A}}. \tag{1.206}$$

In particular, the diagonal element of the field density matrix $\rho_{nn} = p(n)$ represents the probability of finding the optical field in the $|n\rangle$ state. Therefore, the quantum laser rate equation can be described by

$$\dot{p}(n) = -\Big[\frac{(n+1)\mathscr{A}}{1+(n+1)\mathscr{B}/\mathscr{A}}\Big]p(n) + \Big[\frac{n\mathscr{A}}{1+n\mathscr{B}/\mathscr{A}}\Big]p(n-1) \tag{1.207}$$

$$- \kappa n p(n) + \kappa(n+1)p(n+1). \tag{1.208}$$

The above equation describes the flow of the probability of various photon states. By looking at the equation, it is clear that only three neighboring states $|n-1\rangle, |n\rangle, |n+1\rangle$ population transfer is directly possible via such interaction. Here, $p(n-1)$ and $p(n+1)$ represent the gain and loss term of the cavity. We will use the discussed technique for analyzing the laser scheme in Chapter 4.

1.10 Quantum entanglement

In a classically interacting composite system with two sub-systems, any measurement on the first sub-system does not affect the second sub-system; therefore, it provides definite results on each sub-system and evolves independently. However, this concept is not always correct when considering a quantum system. For an interacting two-particle quantum system, the final state of the individual particles is no longer independent of each other even after separating the particles at a considerable distance. Therefore, the total wavefunction can not be written in terms of the tensor product of individual particle wavefunction. In the early times of quantum mechanics, many leading physicists did not accept this concept. In 1935, Einstein, Podolsky, and Rosen published a paper [83] on a thought experiment explaining that the quantum mechanical description of physical reality given by the wave function is incomplete. This famous concept later attracted great attention and became popularly known as the EPR paradox. The wavefunction of the composite system described in the EPR paradox is given by

$$|\Psi\rangle_{EPR} = \frac{1}{2}\left(|+_1, -_2\rangle - |-_1, +_2\rangle\right) \tag{1.209}$$

where $|\pm_i\rangle, i = 1, 2$ represent the spin state of the first and second particle. Following the concept, Schrödinger first coined the term "entanglement" to describe the quantum correlation between two particles separated at some distance after the interaction. The concept has received much more attention in the last few decades, which has led to the opening of new branches, such as quantum information, quantum communication, quantum cryptography, and teleportation. The two-level quantum system called qubit is realized in terms of the polarisation or spin state. The entangled photon pair has several applications, such as long-distance quantum communication protocols, quantum cryptography, and quantum teleportation. For that reason, the entangled photon pair generation scheme has gained much attention in recent times. Several existing entangled photon pair generation methods are parametric down-conversion, four-wave mixing process, and QD-cavity systems.

1.10.1 Criteria for two-mode entanglement

We consider a system with two cavity modes labeled 1 and 2. Therefore, the individual modes act as subsystems and will define whether the system's total state is entangled. A system is known to be separable when the total wave function can be written as a tensor product of two individual subsystem functions. In terms of the density matrix, a two-mode system's quantum state ρ is separable if it can be expressed in terms of the product form as given below

$$\rho = \sum_i p_i \rho_{i1} \otimes \rho_{i2}, \tag{1.210}$$

where we have considered the ρ_{i1}, ρ_{i2} to be an individual normalized state of the first and second mode, respectively, and $p_i \geq 0$ satisfy the conservation relation $\sum_i p_i = 1$. A maximally entangled continuous variable state can be expressed as a co-eigenstate of a pair of EPR type operators [83], such as $\hat{x}_1 + \hat{x}_2$ and $\hat{p}_1 - \hat{p}_2$. Due to the maximally entangled continuous variable state, the total variance of these two operators is reduced to zero. Obviously, this state refers to a limiting case and is not physical. For a practical entangled continuous variable state such as two-mode squeezed states, the mentioned variance will rapidly tend to zero by increasing the squeezing parameter. In this context, Duan et al.[84] found that a lower bound of the total variance exists for any separable state. In general, they consider the two EPR-like operators given by

$$\hat{u} = |a|\hat{x}_1 + \frac{1}{a}\hat{x}_2, \hat{v} = |a|\hat{p}_1 - \frac{1}{a}\hat{p}_2, \tag{1.211}$$

where we have assumed a to be an arbitrary nonzero real number. For any separable state, the lower bound of the total variance of such variable pair satisfying the commutation relation $[\hat{x}_j, \hat{p}_{j'}] = i\delta_{jj'}$ is written as

$$\langle(\Delta\hat{u})^2\rangle_\rho + \langle(\Delta\hat{v})^2\rangle_\rho \geq a^2 + \frac{1}{a^2}. \tag{1.212}$$

Therefore, the inequality indirectly indicates that the states are inseparable in the region, which satisfies

$$\langle(\Delta\hat{u})^2\rangle_\rho + \langle(\Delta\hat{v})^2\rangle_\rho \leq a^2 + \frac{1}{a^2}. \tag{1.213}$$

This inequality is an essential condition for defining the two-mode entanglement. In Chapter 4, we will use this inequality to quantize the two-mode entanglement.

Chapter 2

Self-induced transparency

2.1 Introduction

In this chapter, we will discuss our first research work. We consider the simplest model system of a two-level emitter interacting with an optical field. Specifically, the optical field intensity is time-dependent and conventionally called an optical pulse. Generally, a weak optical pulse propagating through the medium is always completely absorbed by the medium. However, in self-induced transparency (SIT), an optical pulse propagates resonantly through the two-level absorbing medium without any loss and distortion. This pioneering work was carried out by McCall and Hahn [20, 21]. SIT originates from the generated coherence of a strongly coupled light-medium interaction. Therefore, for observing SIT, the incident pulse should be shorter than the various relaxation times present in the system so that the coherence will not vanish during the pulse propagation. Further, the pulse should be strong enough to excite the atom from the ground state. One of the best theoretical estimations of the input pulse was reported in the "area theorem" [21]. This theorem dictates that a 2π secant pulse can propagate through the medium without any loss and distortion in the pulse shape. In general, for an initial pulse area θ_0 obeying the condition $(n+1)\pi > \theta_0 > n\pi$, evolves the area towards $(n+1)\pi$ or $n\pi$ depending on whether n is odd or even. Therefore input pulse with a larger area of $2n\pi$, breaks up into n number of 2π pulses with different propagation velocities. These effects have been observed experimentally in atomic rubidium medium by Slusher and Gibbs [85]. In particular, they have found excellent agreement between numerical simulations and experimental results. These fundamental properties of the SIT were investigated several times, both theoretically and experimentally [70, 86, 87].

However, in atomic medium, the preparation and trapping of atomic gas required a vast and sophisticated setup. Moreover, due to the gaseous nature of the medium, the different velocities of the atom show Doppler broadening in output results. For the last two decades, solid-state semiconductor mediums have emerged as a potential candidate for optical applications, particularly for scalable on-chip quantum technology. Earlier, the resonant coherent pulse propagation in bulk and quantum-well semiconductors behaves differently compared to a two-level atomic medium. The discrepancy mentioned above occurs due to the many-body Coulomb interaction of the different momentum states present in a bulk medium[88–90]. This problem has been overcome in three-dimensionally confined excitons in quantum dots (QDs). The quantum dots can easily

be engineered to get the desired transition frequency to avoid the problem of laser availability. The scalability and fabrication technology make the semiconductor QDs suitable for modern quantum optics experiments. There have been some interesting theoretical proposals about the possibility of observing SIT in self-organized InGaAs QDs[91]. Excitonic transition in InGaAs QDs have large transition dipole moments and long dephasing time in the range of nanoseconds at cryogenic temperatures [92] and are, therefore a promising candidate for SIT.

Though the QD medium is a potential candidate for observing SIT, it also has a few drawbacks. All the QDs inside the medium are not identical, so an inhomogeneous level broadening is always present in the system. In semiconductors, longitudinal acoustic phonon interaction is vital because of the environment temperature. Interactions between phonon and exciton lead to dephasing in coupled dynamics of exciton-photon interaction[93, 94]. Several theoretical models and experiments have recently explained SIT in the semiconductor QD medium [95–97]. Few of them consider the effect of the phonon environment on the system dynamics in the context of group velocity dispersion[98]. Another recent experimental work showed the SIT mode-locking and area theorem for semiconductor QD medium and rubidium atom [99, 100].

In this chapter, we discuss the possibility of SIT in a semiconductor QD medium incorporating the effect of phonon bath in our model. We utilize the recently developed polaron transformed master equation keeping all orders of exciton-phonon interaction [101–103]. Our model's pulse propagation dynamics depend on system and bath parameters. Hence, the propagation dynamics become more transparent by knowing both the system and the bath's contribution. The motivation behind this work is to find long-distance optical communication without loss of generality in an array of QD. Due to strong confinement of electron hole pairs, QDs have discrete energy levels thus QD arrays mimic atomic medium with the added advantage of scalability and controllability with advanced semiconductor technology. It is also possible to create QD fibers that can be used for quantum communication channels [104, 105]. Motivated by this work, we theoretically investigate the self-induced transparency effect in a semiconductor QD medium.

2.2 Model system

The phonon contribution to QD dynamics at low temperature is mandatory. We assume the propagation of an optical pulse along the z-direction. Accordingly, we define the electric field of the incident optical pulse as

$$\vec{E}(z,t) = \hat{e}\mathcal{E}(z,t)e^{i(kz-\omega_L t)} + c.c, \tag{2.1}$$

where $\mathcal{E}(z,t)$ is the slowly varying envelope of the field. The bulk QD medium comprises multiple alternating InGaAs/GaAs QD deposition layers. Every QD inside the medium strongly interacts with the electric field due to the significant dipole moment. Since all the QD inside the medium is not identical, the exciton energy of the different QD will vary depending on the dot size. The l^{th} type QD can be modeled as a two-level system with exciton state $|1\rangle_l$, and ground state $|2\rangle_l$ with energy gap $\hbar\omega_l$ by taking the proper choice of biexciton binding energy and polarisation as shown in the Fig. 2.1. The raising and lowering operator for the l^{th} type QD can be written as $\sigma_l^+ = |1(\omega_l)\rangle_l\langle 2(\omega_l)|_l$ and $\sigma_l^- = |2(\omega_l)\rangle_l\langle 1(\omega_l)|_l$.

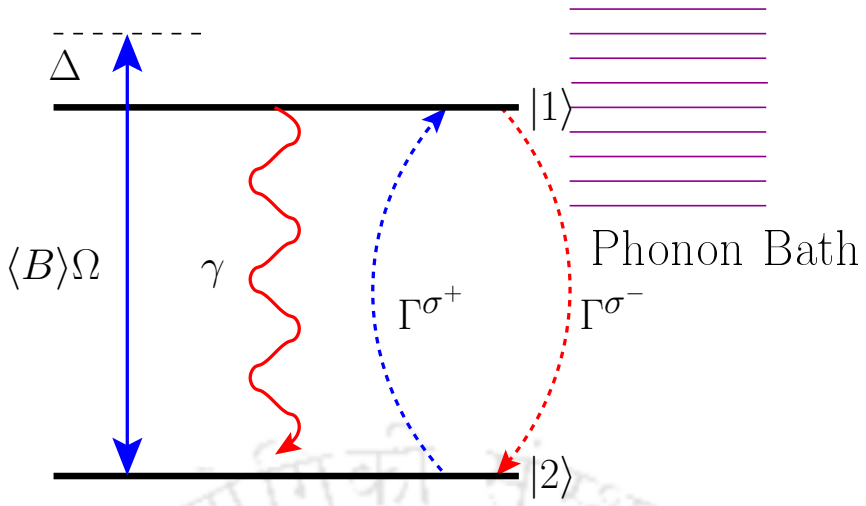

Figure 2.1: A Schematic diagram of the QD level system with ground state $|2\rangle$ and exciton state $|1\rangle$ driven by the optical pulse with effective coupling $\langle B\rangle\Omega$(blue line). The spontaneous decay from the exciton state to the ground state is shown using a curly red line. The parallel violet lines represent the phonon modes interacting with the exciton state. The red and blue dashed lines represent the phonon-induced decay and pumping rate respectively.

In case of semiconductor QD's, the optical properties get modified due to the lattice mode of vibration *i.e.*, the acoustic phonon. Hence, QD exciton transition coupled to an acoustic phonon bath model mimics the desired interaction. The phonon bath consists of a large number of closely spaced harmonic oscillator modes. Therefore, we introduce the annihilation and creation operators associated with k^{th} phonon mode having frequency ω_k as b_k and $b_k^\dagger$. The mode frequency can be expressed as $\omega_k = c_s k$ where k and c_s are the wave vector and velocity of sound. The Hamiltonian for the described model system after making dipole and rotating wave approximation is given by

$$H = \sum_l \Big[-\hbar\delta_l \sigma_l^+\sigma_l^- + \frac{1}{2}\hbar\Big(\Omega(z,t)\sigma_l^+ + \Omega^*(z,t)\sigma_l^-\Big) + \hbar\sigma_l^+\sigma_l^- \sum_k \lambda_k \Big(b_k + b_k^\dagger\Big)\Big] + \hbar\sum_k \omega_k b_k^\dagger b_k, \tag{2.2}$$

where λ_k is the exciton phonon mode coupling constant and $\Omega(z,t) = -2\vec{d}_{12}\cdot\hat{e}\mathcal{E}(z,t)/\hbar$ is the Rabi frequency with transition dipole moment vector $\vec{d}_{12}$. The detuning of the optical field with QD transition is defined as $\delta_l = \omega_L - \omega_l$.

We notice that the Hamiltonian contains an infinite sum over phonon modes. Keeping all order of exciton phonon interaction, we made a transformation in the polaron frame. The transformation rule for modified Hamiltonian is given by $H' = e^P H e^{-P}$ where the operator $P = \sum_l \sigma_l^+\sigma_l^- \sum_k \lambda_k(b_k^\dagger - b_k)/\omega_k$. This transformation also helps us to separate the system Hamiltonian from the total Hamiltonian which is our primary interest. The transformed Hamiltonian is divided into system, bath and interaction

part, which can be decomposed as $H' = H_s + H_b + H_I$, where

$$H_s = \sum_l -\hbar\Delta_l \sigma_l^+ \sigma_l^- + \langle B\rangle X_l^g, \tag{2.3}$$

$$H_b = \hbar \sum_k \omega_k b_k^\dagger b_k, \tag{2.4}$$

$$H_I = \sum_l \xi_g X_l^g + \xi_u X_l^u, \tag{2.5}$$

and Δ_l is the redefined detuning by considering the polaron shift $\sum_k \lambda_k^2/\omega_k$. The definition of phonon-modified system operators is given by

$$X_l^g = \frac{\hbar}{2}\left(\Omega(z,t)\sigma_l^+ + \Omega^*(z,t)\sigma_l^-\right), \tag{2.6}$$

$$X_l^u = \frac{i\hbar}{2}\left(\Omega(z,t)\sigma_l^+ - \Omega^*(z,t)\sigma_l^-\right). \tag{2.7}$$

The phonon bath fluctuation operators are

$$\xi_g = \frac{1}{2}\left(B_+ + B_- - 2\langle B\rangle\right), \tag{2.8}$$

$$\xi_u = \frac{1}{2i}\left(B_+ - B_-\right), \tag{2.9}$$

where B_+ and B_- are the coherent-state phonon displacement operators. Explicitly, the phonon displacement operators in terms of the phonon mode operators can be written as

$$B_\pm = \exp\left[\pm \sum_k \frac{\lambda_k}{\omega_k}\left(b_k^\dagger - b_k\right)\right].$$

From this expression, it is clear that the exponential of the phonon operator takes care of all the higher order phonon processes. Therefore, the phonon displacement operator averaged over all closely spaced phonon modes at a temperature T, obeys the relation $\langle B_+\rangle = \langle B_-\rangle = \langle B\rangle$ where

$$\langle B\rangle = \exp\left[-\frac{1}{2}\int_0^\infty d\omega \frac{J(\omega)}{\omega^2}\coth\left(\frac{\hbar\omega}{2K_BT}\right)\right], \tag{2.10}$$

and K_B is the Boltzmann constant. The phonon spectral density function $J(\omega) = \alpha_p\omega^3\exp[-\omega^2/2\omega_b^2]$ describes longitudinal acoustic(LA) phonon coupling via a deformation potential [106] for QD system, where the parameters α_p and ω_b are the electron-phonon coupling and cutoff frequency, respectively.

Next we use the master equation(ME) approach to solve the polaron-transformed system Hamiltonian dynamics by considering the phonon bath as a perturbation. The Born-Markov approximation can be performed with respect to the polaron-transformed perturbation in the case of nonlinear excitation. Hence, the density matrix equation for the reduced system under Born-Markov approximation can be written as

$$\dot\rho = \frac{1}{i\hbar}[H_s,\rho] + \sum_l\left(\mathcal{L}_{ph}\rho + \frac{\gamma}{2}\mathcal{L}[\sigma_l^-]\rho + \frac{\gamma_d}{2}\mathcal{L}[\sigma_l^+\sigma_l^-]\rho\right), \tag{2.11}$$

where γ is the spontaneous decay rate of the exciton state. The spontaneous decay originates from the quantum fluctuations of the vacuum state. Similarly, for thermal

fluctuation, we have adopted the final Lindbladian form of the dephasing interaction model described by a simple stochastic Hamiltonian[107]. Therefore, we incorporate the pure-dephasing process phenomenologically in ME with a decay rate γ_d. This additional dephasing term explains the broadening of the zero-phonon line (ZPL) in QD with increasing temperatures [108, 109]. The Lindblad superoperator $\mathcal{L}$ is expressed as $\mathcal{L}[\mathcal{O}]\rho = 2\mathcal{O}\rho\mathcal{O}^\dagger - \mathcal{O}^\dagger\mathcal{O}\rho - \rho\mathcal{O}^\dagger\mathcal{O}$, under the operation of $\mathcal{O}$ operator. The term $\mathcal{L}_{ph}$ represents the effect of phonon bath on the system dynamics. Therefore the explicit form of $\mathcal{L}_{ph}\rho$ in terms of previously defined system operators can be expressed as

$$\begin{aligned}\mathcal{L}_{ph}\rho &= -\frac{1}{\hbar^2}\int_0^\infty d\tau \sum_{j=g,u} G_j(\tau)[X_l^j(z,t), X_l^j(z,t,\tau)\rho(t)] \\ &+ H.c.,\end{aligned} \tag{2.12}$$

where $X_l^j(z,t,\tau) = e^{-iH_s\tau/\hbar}X_l^j(z,t)e^{iH_s\tau/\hbar}$, and the polaron Green's functions are $G_g(\tau) = \langle B\rangle^2\{\cosh[\phi(\tau)] - 1\}$ and $G_u(\tau) = \langle B\rangle^2 \sinh[\phi(\tau)]$. The phonon Green's functions depend on phonon correlation function given below

$$\phi(\tau) = \int_0^\infty d\omega \frac{J(\omega)}{\omega^2}\left[\coth\left(\frac{\hbar\omega}{2K_BT}\right)\cos(\omega\tau) - i\sin(\omega\tau)\right]. \tag{2.13}$$

The polaron ME formalism is not generally valid for arbitrary excitation strength and exciton phonon coupling. The validity of polaron ME is stated as [101]

$$\left(\frac{\Omega}{\omega_b}\right)^2\left(1 - \langle B\rangle^4\right) \ll 1. \tag{2.14}$$

It is clear from the above equation that, at low temperatures $\langle B\rangle \approx 1$ and $\Omega/\omega_b < 1$ fulfil the above criteria. Hence, we restrict our calculation in the weak field regime satisfying $\Omega/\omega_b < 1$ at a low phonon bath temperature.

The full polaron ME (2.11) contains multiple commutator brackets and complex operator exponents, which require involved numerical treatment for studying time dynamics. We make some simplifications of the full ME by using various useful identities. These reduce ME into a simple analytical form with decay rates corresponding to the various phonon-induced processes. Though we have not made any approximation, simplified ME scales down the numerical computation efforts and gives better insight into the physical process. By expanding all the commutators in Eq.(2.11) and rearranging using fermion operator identities, we get the simplified ME as

$$\begin{aligned}\dot{\rho} = \frac{1}{i\hbar}[H_s,\rho] + \sum_l \Big(&\frac{\gamma}{2}\mathcal{L}[\sigma_l^-]\rho + \frac{\gamma_d}{2}\mathcal{L}[\sigma_l^+\sigma_l^-]\rho \\ &+ \frac{\Gamma_l^{\sigma^+}}{2}\mathcal{L}[\sigma_l^+]\rho + \frac{\Gamma_l^{\sigma^-}}{2}\mathcal{L}[\sigma_l^-]\rho - \Gamma_l^{cd}(\sigma_l^+\rho\sigma_l^+ + \sigma_l^-\rho\sigma_l^-) \\ &- i\Gamma_l^{sd}(\sigma_l^+\rho\sigma_l^+ - \sigma_l^-\rho\sigma_l^-) + i\Delta_l^{\sigma^+\sigma^-}[\sigma_l^+\sigma_l^-,\rho] \\ &- [i\Gamma_l^{gu+}(\sigma_l^+\sigma_l^-\rho\sigma_l^+ + \sigma_l^-\rho - \sigma_l^+\sigma_l^-\rho\sigma_l^-) + H.c.] \\ &- [\Gamma_l^{gu-}(\sigma_l^+\sigma_l^-\rho\sigma_l^+ - \sigma_l^-\rho + \sigma_l^+\sigma_l^-\rho\sigma_l^-) + H.c.]\Big).\end{aligned} \tag{2.15}$$

The phonon-induced decay rates are given by

$$\Gamma_l^{\sigma^+/\sigma^-} = \frac{\Omega_R(z,t)^2}{2}\int_0^\infty \Bigg(\mathrm{Re}\Big\{(\cosh(\phi(\tau))-1)f(z,t,\tau) + \sinh(\phi(\tau))\cos(\eta(z,t)\tau)\Big\} \mp \mathrm{Im}\left\{(e^{\phi(\tau)}-1)\frac{\Delta_l \sin(\eta(z,t)\tau)}{\eta(z,t)}\right\}\Bigg) d\tau, \tag{2.16}$$

$$\Gamma_l^{\mathrm{cd}} = \frac{1}{2}\int_0^\infty \mathrm{Re}\Big\{\Omega_S(z,t)\sinh(\phi(\tau))\cos(\eta(z,t)\tau) - \Omega_S(z,t)(\cosh(\phi(\tau))-1)f(z,t,\tau) + \Omega_T(z,t)(e^{-\phi(\tau)}-1)\frac{\Delta_l \sin(\eta(z,t)\tau)}{\eta(z,t)}\Big\} d\tau, \tag{2.17}$$

$$\Gamma_l^{\mathrm{sd}} = \frac{1}{2}\int_0^\infty \mathrm{Re}\Big\{\Omega_T(z,t)\sinh(\phi(\tau))\cos(\eta(z,t)\tau) - \Omega_T(z,t)(\cosh(\phi(\tau))-1)f(z,t,\tau) - \Omega_S(z,t)(e^{-\phi(\tau)}-1)\frac{\Delta_l \sin(\eta(z,t)\tau)}{\eta(z,t)}\Big\} d\tau, \tag{2.18}$$

$$\Delta_l^{\sigma^+\sigma^-} = \frac{\Omega_R(z,t)^2}{2}\int_0^\infty \mathrm{Re}\left\{(e^{\phi(\tau)}-1)\frac{\Delta_l \sin(\eta(z,t)\tau)}{\eta(z,t)}\right\} d\tau, \tag{2.19}$$

$$\Gamma_l^{\mathrm{gu}+} = \frac{\Omega_R(z,t)^2}{2}\int_0^\infty \Big\{(\cosh(\phi(\tau))-1)\,\mathrm{Im}[\langle B\rangle\Omega]h(z,t,\tau) + \sinh(\phi(\tau))\frac{\mathrm{Re}[\langle B\rangle\Omega]\sin(\eta(z,t)\tau)}{\eta(z,t)}\Big\} d\tau, \tag{2.20}$$

$$\Gamma_l^{\mathrm{gu}-} = \frac{\Omega_R(z,t)^2}{2}\int_0^\infty \Big\{(\cosh(\phi(\tau))-1)\,\mathrm{Re}[\langle B\rangle\Omega]h(z,t,\tau) - \sinh(\phi(\tau))\frac{\mathrm{Im}[\langle B\rangle\Omega]\sin(\eta(z,t)\tau)}{\eta(z,t)}\Big\} d\tau, \tag{2.21}$$

where

$$f(z,t,\tau) = (\Delta_l^2\cos(\eta(z,t)\tau) + \Omega_R(z,t)^2)/\eta(z,t)^2, \tag{2.22}$$

$$h(z,t,\tau) = \Delta_l(1-\cos(\eta(z,t)\tau))/\eta^2(z,t), \tag{2.23}$$

$$\eta(z,t) = \sqrt{\Omega_R(z,t)^2+\Delta_l^2} \tag{2.24}$$

with the polaron-shifted Rabi frequency,

$$\Omega_R(z,t) = \langle B\rangle|\Omega(z,t)|, \tag{2.25}$$

$$\Omega_S(z,t) = \mathrm{Re}[\langle B\rangle\Omega(z,t)]^2 - \mathrm{Im}[\langle B\rangle\Omega(z,t)]^2, \tag{2.26}$$

$$\Omega_T(z,t) = 2\,\mathrm{Re}[\langle B\rangle\Omega(z,t)]\,\mathrm{Im}[\langle B\rangle\Omega(z,t)]. \tag{2.27}$$

Next, we use Maxwell wave equation to describe the propagation dynamics of the electromagnetic field inside the QD medium

$$\left(\nabla^2 - \frac{1}{c^2}\frac{\partial^2}{\partial t^2}\right)\vec{E}(z,t) = \mu_0\frac{\partial^2}{\partial t^2}\vec{P}(z,t) \tag{2.28}$$

where μ_0 is the permeability of free space. The induced polarisation $\vec{P}(z,t)$ originates from the alignment of the medium dipole in the presence of an applied field. Therefore it depends on the coherence term of the density matrix equation. For l^{th} type QD, the coherence term of the density matrix equation can be written as $\rho_{12}(\Delta_l, z, t) = \langle 1(\omega_l)|_l \rho(z,t)|2(\omega_l)\rangle_l$. The medium consists of a large number of QD with continuous frequency distribution centered at ω_c. Therefore we can safely replace the summation with integration by redefining the discrete variable Δ_l to a continuous variable Δ. The induced macroscopic polarisation can be written in terms of the density matrix element as

$$\vec{P}(z,t) = N \int_{-\infty}^{\infty} \left(\vec{d}_{12} \rho_{12}(\Delta, z, t) e^{i(kz - \omega_L t)} + c.c. \right) g(\Delta) d\Delta, \tag{2.29}$$

where N is the QD volume number density. The inhomogeneous level broadening function in the frequency domain is defined by $g(\Delta)$. In our calculation, the form of $g(\Delta)$ is

$$g(\Delta) = \frac{1}{\sigma\sqrt{2\pi}} e^{-\frac{(\Delta - \Delta_c)^2}{2\sigma^2}}, \tag{2.30}$$

where the standard deviation is σ. The detuning between the applied field and the QD's central frequency is represented by Δ_c. By applying slowly varying envelope approximation, one can cast inhomogeneous second order partial differential Eq.(2.28) to first order differential equation as

$$\left(\frac{\partial}{\partial z} + \frac{1}{c} \frac{\partial}{\partial t} \right) \Omega(z,t) = i\eta \int_{-\infty}^{\infty} \rho_{12}(\Delta, z, t) g(\Delta) d\Delta, \tag{2.31}$$

where the coupling constant η is defined by

$$\eta = -3N\lambda^2\gamma/4\pi \tag{2.32}$$

and λ is the carrier wavelength of the QD transition. The self consistent solution of Eq.(2.15) and (2.31) with proper initial conditions can display the spatiotemporal evolution of the field inside the medium. Moreover the analytical solution of the coupled partial differential equation is known only for some special conditions, hence we adopted numerical integration of Eq.(2.15) and (2.31) to depict the results. For numerical computation, a useful frame transformation $\tau = t - z/c$ and $\zeta = z$ is needed which removes the explicit time variable from Eq.(2.31), which now only depends on the one variable ζ.

2.3 Numerical result

2.3.1 Phonon-induced scattering rates

First we discuss various decay rates for the QD system with experimentally available parameter regions [110, 111]. The medium comprises InGaAs/GaAs QDs with volume density $N = 5 \times 10^{20} \mathrm{m}^{-3}$ and a length of 1 mm. The central QD excitation energy is $\hbar\omega_c$ =1.3 eV with a Gaussian spectral distribution having FWHM of 23.5 meV. The QD is driven by the optical pulse at $\zeta = 0$ with a hyperbolic secant profile

$$|\Omega(0,\tau)| = \Omega_0 \operatorname{sech}\left(\frac{\tau - \tau_c}{\tau_0} \right) \tag{2.33}$$

where τ_0, and τ_c defines the width, and center of the pulse, respectively. For numerical computation, the amplitude and width of the pulse are taken to be $\Omega_0 = 0.2$ meV and $\tau_0 = 6.373$ ps. The phonon bath temperature T = 4.2 K gives $\langle B \rangle = 0.95$. Other parameters are $\alpha_p = 0.03$ ps^2, $\omega_b = 1$ meV. The system under consideration has a relaxation rate $\gamma = \gamma_d = 2$ μeV(2 ns). In order to normalize all the system parameters to a dimensionless quantity we have chosen normalization frequency to be $\gamma_n = 1$ rad/ps.

In Fig. 2.2, the color bar represents the variation of various phonon-induced scattering rates as a function of detuning and time, both at normalised units along the x- and y-axis respectively. In the QD system, various phonon processes are connected with exciton transitions. In the case of ground state to exciton transition, phonon absorption occurs while in the opposite process, phonon emission occurs. Now we

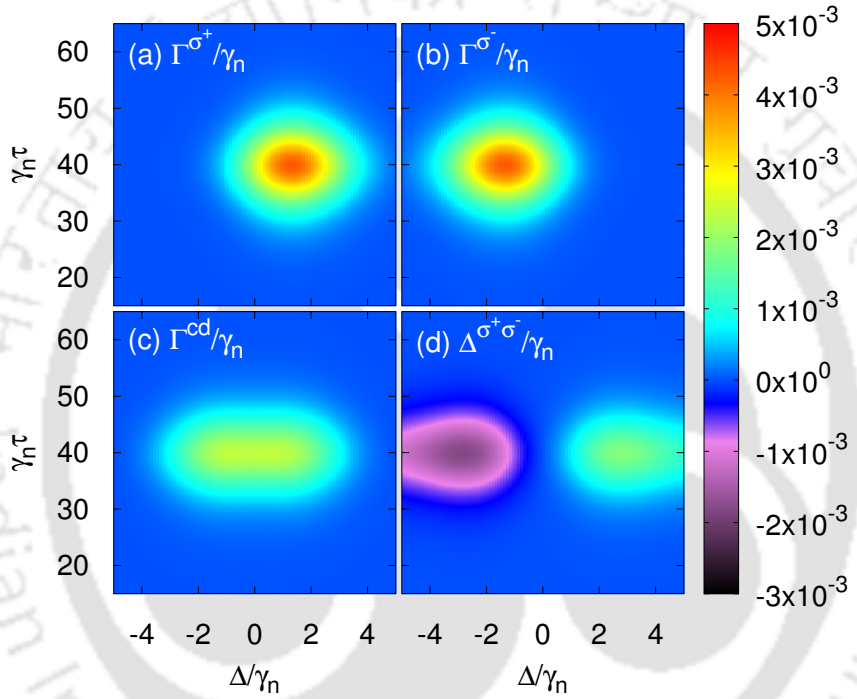

Figure 2.2: The variation of phonon-induced scattering rates with detuning and time of a QD at $\zeta = 0$ for the applied secant pulse in Eq.(2.33). a) Phonon-induced pumping rate Γ^{σ^+}[Eq.(2.16)] b) Phonon-induced decay rate Γ^{σ^-}[Eq.(2.16)] c) Phonon induced dephasing $\Gamma^{\rm cd}$[Eq.(2.17)] d) Phonon induced detuning $\Delta^{\sigma^+\sigma^-}$[Eq.(2.19)] for peak Rabi frequency $\Omega_0 = 0.2$ meV, pulse width $\tau_0 = 6.373$ ps and pulse center $\gamma_n\tau_c = 40$. The phonon bath temperature T = 4.2 K corresponds to $\langle B \rangle = 0.95$ with spectral density function parameters $\alpha_p = 0.03$ ps^2, $\omega_b = 1$ meV.The first two subplots, (a) and (b), display the low-temperature asymmetry in phonon-induced pumping (Γ^{σ^+}) and decay rate (Γ^{σ^-}) as we can see that peak value shifted towards positive and negative detuning respectively. In panel (c), the phonon-assisted dephasing rate (Γ^{cd}) associated with the off-diagonal density matrix term changes symmetrically with the detuning and attain maximum at resonance. The last subfigure (d) shows phonon-induced detuning varies similarly with actual detuning as their sign is the same in the plot.

discuss the physical process associated with the phonon scattering rates Γ^{σ^+} and Γ^{σ^-}. For positive detuning, the applied field frequency is larger than the QD transition frequency. Subsequently a phonon generates with Δ frequency in order to make a resonant QD transition. These emitted phonons develop an incoherent excitation in the system referred by the Γ^{σ^+}. Oppositely for negative detuning, the applied field

frequency is smaller than the QD transition frequency, and a resonant QD transition is possible only when some phonon of frequency Δ will be absorbed from the bath. With this mechanism, QD exciton to ground state decay enhances the radiation which is represented by the Γ^{σ^-}. This low-temperature asymmetry is clearly visible in Fig. 2.2(a) and 2.2(b). At higher temperatures, this asymmetry gets destroyed, and both rates overlap and are centered at $\Delta = 0$. Fig. 2.2(c) shows the variation of Γ^{cd} which is only present in the off-diagonal density matrix element and responsible for the additional dephasing in the system dynamics. The additional detuning $\Delta^{\sigma^+\sigma^-}$ from the simplified master equation plotted in Fig. 2.2(d), shows a very tiny value compared to the system detuning Δ. We also notice that the sign of $\Delta^{\sigma^+\sigma^-}$ changes according to the system detuning Δ. It is important to keep in mind that we display the variation along the y-axis around $\gamma_n\tau$ =40, which is the centre of the pulse with the secant profile.

2.3.2 Pulse area theorem

It is well know from Beer's law, that a weak pulse gets absorbed inside the medium due to the presence of opacity at the resonance condition. However, McCall and Hahn showed that some specific envelope pulse shape remains intact for a long distance without absorption, even at resonance[20, 21]. Inspired of this phenomena, we have taken into account of a time-varying pulse whose envelope shape is stated in the Eq.(2.33). The area $\Theta(z)$ enclosed by its hyperbolic envelope shape is defined as

$$\Theta(z) = \int_{-\infty}^{+\infty} \Omega(z, t^{'})dt^{'}. \tag{2.34}$$

By formally integrating Eq.(2.31) over time and detuning, one can find the spatial variation of the pulse area closely followed by the McCall and Hahn work. The evolution of the pulse area $\Theta(z)$ during its propagation in a two-level absorbing QD medium is given by

$$\frac{d\Theta(z)}{dz} = -\frac{\alpha}{2}\sin\Theta(z) \tag{2.35}$$

where α is the optical extinction per unit length. The optical extinction depends on the various system parameters as $\alpha = 2\pi\eta g(0)$. The solution of the Eq.(2.35) is

$$\tan\frac{\Theta(z)}{2} = \tan\frac{\Theta(0)}{2}e^{-\alpha z/2}, \tag{2.36}$$

where $\Theta(0)$ is the pulse area at z =0. It is clear from the above expression that $\Theta(z) = 2n\pi$ is the stable solution, whereas $\Theta(z) = (2n+1)\pi$ is an unstable one. The pulse area of the given envelope as stated in Eq.(2.33) is $\Theta(0) = \pi\Omega_0\tau_0$. Thus, the envelope with amplitude $\Omega_0 = 2/\tau_0$ gives 2π area pulse. This envelope shape remains preserve for the long propagation distance even though it interacts resonantly with the medium.

Fig. 2.3 exhibits the variation of pulse area with the propagation distance inside the QD medium. It is evident from this figure that the propagation dynamics of 2π area pulse through the medium of length L has negligible loss in pulse area. In the absence of phonon(black line) interaction, the system behaves identical to the atomic system and hence follows $\Theta \approx 2\pi(1-\tau_0/T_2^{'})$ reported earlier by McCall and Hahn [21]. The loss in

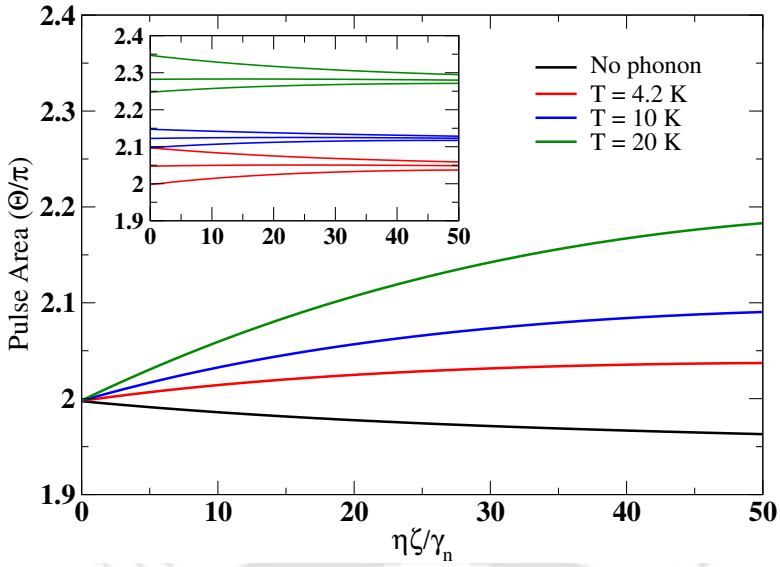

Figure 2.3: Evolution of the pulse area(Θ) as a function of propagation distance ζ started with 2π sech-type pulse for different temperatures. The applied pulse has a width of τ_0 = 6.373 ps and centered at $\gamma_n\tau_c = 40$. The system under consideration without phonon bath(black) and with phonon bath maintaining temperature T = 4.2K(red), 10K(blue), 20K(green) with electron phonon coupling $\alpha_p = 0.03$ ps^2 and cut off frequency $\omega_b = 1$ meV.The central QD detuning Δ_c = 0 with spontaneous decay and the pure dephasing rate $\gamma = \gamma_d = 2$ μeV(2 ns).The optical extinction per unit length α = 10 mm^{-1}. Comparing these four different temperature pulse area curves, we can understand that a higher pulse area is required for stable pulse propagation to compensate for the effect of phonon at higher temperatures. The inset figure shows the stability of the pulse area higher than 2π for different phonon bath temperatures.

pulse area comes from the finite lifetime $T_2^{'}$ of the QD which is inversely proportional to γ_d. Ideally, the pulse will retain initial pulse area for an arbitrary distance in absence of decay and decoherence. However, in presence of phonon contribution, we have noticed the pulse area gets enhanced by a small amount. The amount of raise in the pulse area linearly depends on the bath temperature as indicated in Fig. 2.3. This effect can be explained by carefully examing the definition of an effective Rabi frequency $\Omega_R(z,t) = \langle B\rangle|\Omega(z,t)|$ where $\langle B\rangle$ is dependent on the bath temperatures. The inset of Fig. 2.3 illustrate the convergence of the pulse area shifted from the 2π value at different temperatures.

To explain the behavior of Fig. 2.3, we study the absorption and dispersion properties of the medium as a function of detuning at various time intervals of the pulse. Fig. 2.4 delineates the physical process behind the dispersion and absorption. We assume all the population in the ground state, before the leading edge of the pulse reaches the medium. The peak of incident pulse enters inside the medium at $\gamma_n\tau_c = 40$. It is clear from Fig. 2.4(a) that most of the leading edge pulse energy gets absorbed by the ground state population and the population goes to the excited state. Hence the medium shows maximum absorption at $\gamma_n\tau = 30$, hence elucidating the absorption phenomenon at resonance. Simultaneously, the nature of the dispersion curve is anomalous as previously reported [112]. The anomalous dispersion accompanied fast velocity is completely prohibited due to huge absorption at the resonance condition. The medium becomes saturated as the centre of the pulse enters the medium; consequently, the medium turns less absorbent to the pulse. Nonetheless, a tiny absorption peak still

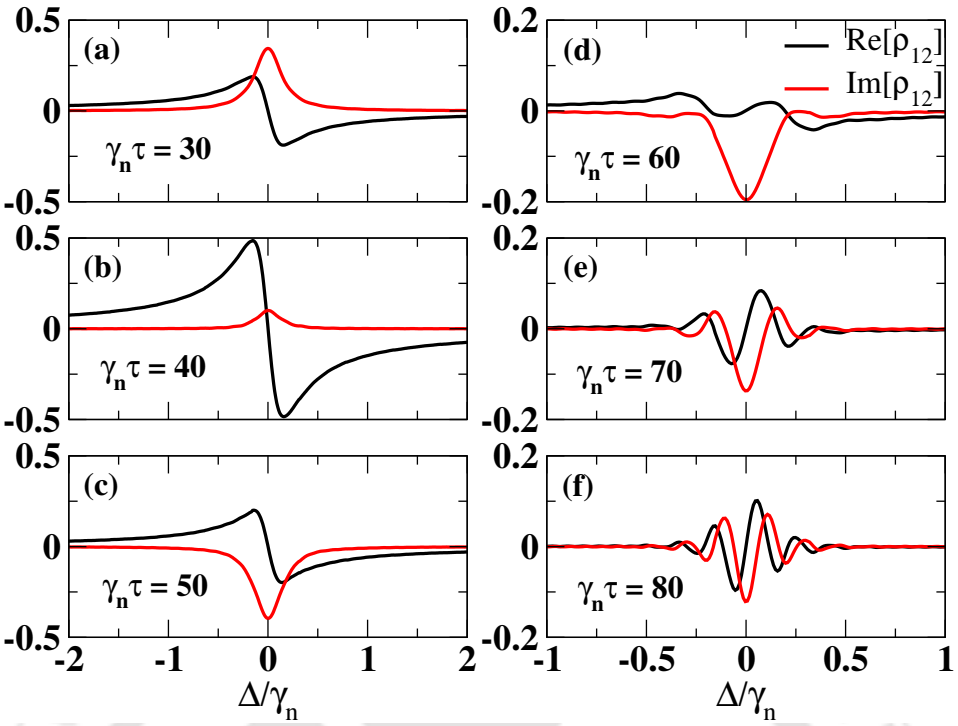

Figure 2.4: The real(black) and imaginary(red) part of the coherence ρ_{12} of a single QD at different times for a 2π sech-type short pulse with pulse center at $\gamma_n\tau_c = 40$ as a function of detuning. The pulse has a width $\tau_0 = 6.373$ ps. Corresponding phonon bath parameters are T = 4.2K, $\alpha_p = 0.03$ ps^2, $\omega_b = 1$ meV. Considered QD relaxation rates are $\gamma = \gamma_d = 2$ μeV(2 ns). In this figure, a positive and negative value of the red curve corresponds to the absorption and gain of the medium; also, the black curve represents the dispersion. Looking at the subfigures, it is clear that medium property changes with time, equivalently interacting with the different parts of the pulse. At a time before the pulse center $\gamma_n\tau = 30$, the medium shows high absorption, then at the center, $\gamma_n\tau = 40$ medium becomes almost transparent, finally after the pulse center $\gamma_n\tau = 50$ medium display high gain. After a long time from the pulse center $\gamma_n\tau = 80$, the dispersion curve also changes from the anomalous dispersion to the normal dispersion, completing the cycle for reconstructing the identical pulse.

exists at the resonance condition due to the presence of various decay processes of the medium as indicated by Fig. 2.4(b). Therefore, the excited state gets populated during the passage of the leading edge pulse. This population can leave the excited state and return to the ground by stimulated emission in the presence of the trailing edge of the pulse. As a results, a gain can be experienced by the incident pulse at $\gamma_n\tau = 50$ as revealed in Fig. 2.4(c). From these three panels, we can conclude that the leading edge of the pulse gets absorbed by the medium, while the trailing edge of the pulse experiences gain. Towards the trailing end of the pulse, the dispersive nature of the medium changes from anomalous to normal, as shown in Fig. 2.4(d). The positive slope of the dispersion curve lead to slow group velocity that started at $\gamma_n\tau = 60$ shown in Fig. 2.4(d). Fig. 2.4(d) to Fig. 2.4(f) indicate that the optical pulse regeneration process is completed due to the medium-assisted gain; hence, the pulse shape remains preserved. This is the explanation of the underpinning mechanism behind SIT. The claim of the above physical mechanism can be supported by studying population dynamics at the excited state. For this purpose, we have plotted the excited state population as a function of the pulse area in Fig. 2.5. A noticeable population

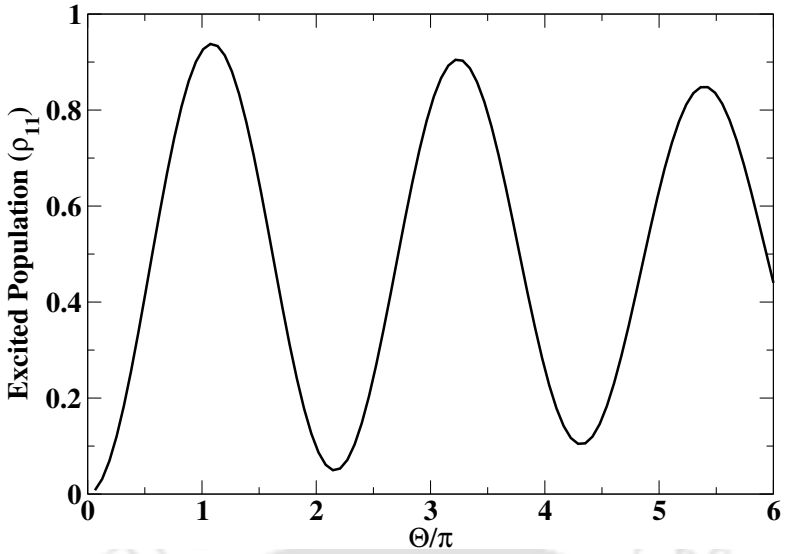

Figure 2.5: The variation of excited state population with input pulse area at resonance condition $\Delta_c = 0$. The system and bath parameters are $\tau_0 = 6.373$ ps, $\gamma_n \tau_c = 40$, T = 4.2K, $\alpha_p = 0.03$ ps^2, $\omega_b = 1$ meV, $\gamma = \gamma_d = 2$ μeV(2 ns). The excited state population curve matches the pulse area theorem statements as the population peaks near odd π pulse area and population dips near even π pulse area. The lower population value indicates the fact that the medium becomes transparent. The phonon-assisted pulse area shift signatures are visible as the population dip is not precisely at 2π but instead shifted towards a slightly higher value, validating our previous findings.

redistribution among the levels is feasible within few widths of incident pulse wherein intensity is appreciable. As soon as the pulse intensity diminishes at the trailing end, spontaneous emission takes care of depletion of the excited state population. This leads to vanishing population at the excited state after a sufficiently long time from the pulse centre. As a consequence, it is crucial to decide the observation time of the QD population. Hence, we display the exciton population at just the end of the pulse $\gamma_n \tau = 60$, to capture the outcome of the pulse. It is clear from Fig. 2.5 that the excited state population shows a decaying Rabi oscillation kind of behaviour. It is also confirmed that the population never fully transferred to the excited state or fully returned to the ground state for any pulse area, indicating to non-constant phonon induced decay and gain process involved in the system. The decaying features of the local population maximum can be justified by the examining the photon and phonon induced decay rates. The various phonon decay rates are given in Eq.(2.16)-(2.21) where increasing incident pulse amplitude $\Omega(z,t)$ results in the enhancement of these decay rates. This field amplitude dependent phonon decay together with constant photon decay can explain the gradual decay of the population local maxima. On the contrary, the dip of local minima increases due to the presence of phonon induced gain processes $\Gamma^{\sigma+}$ as suggested in Eq.(2.16). The local maximum and minimum of the exciton population are located respectively near odd and even integer multiples of π pulse area. The maxima signifies the pulse absorption by the medium, resulting in population inversion. Similarly, minima manifests the transparency of the medium. Thus, the leading edge of the pulse excite the population whereas the trailing edge assists in stimulated emission leaving the population in the ground state of the medium. It is evident that only even integer multiples of π pulse can propagate through the medium without absorption that is consistent with the pulse area theorem. That

the local maxima and minima of exciton population never match exactly with the integer value can be figured out later by investigating pulse propagation dynamics. Previously, we found the stable pulse area is higher than 2π as shown in Fig. 2.3 which also agrees with the above observation. Therefore, the analysis of coherence and population ensures us that SIT phenomena can be accomplished in the QD medium.

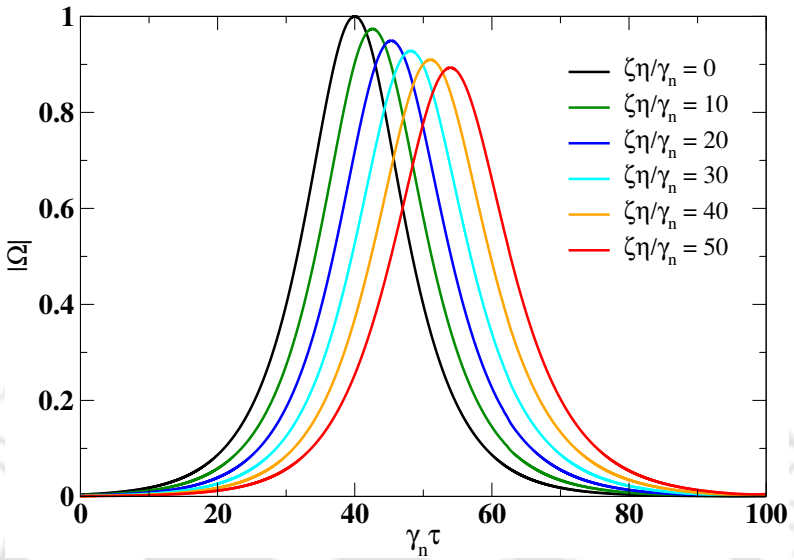

Figure 2.6: The Rabi frequency normalized with the input peak value is plotted against retarded time at different propagation distances inside the medium at resonance condition $\Delta_c = 0$. The input pulse has the following parameters $\Theta(0) = 2\pi$, $\tau_0 = 6.373$ ps, $\gamma_n\tau_c = 40$. The chosen QD inhomogeneous level broadening in normalized units $\sigma/\gamma_n = 15$. Other parameters are T = 4.2K, $\alpha_p = 0.03$ ps^2, $\omega_b = 1$ meV, $\gamma = \gamma_d = 2$ μeV(2 ns). This figure portrays how the pulse peak intensity decreases with the propagation length and experiences a minimal intensity loss, unlike the ideal scenario where no intensity change occurs. Various phenomenological and phonon-induced decay is responsible for such behaviors.

2.3.3 Self Induced Transparency

A homogenous QD medium with length 1 mm is taken into account for studying spatio-temporal evolution of hyperbolic secant optical pulse. To achieve a stable pulse propagation, we have chosen the initial pulse area to be 2π. Fig. 2.6 confirms the area theorem by showing a stable optical pulse propagation for a longer distance. However, the pulse shape at larger distances has noticed some distortion and absorption. Fig. 2.6 also indicates that the pulse's peak value gradually decreases by increasing the propagation distance. This suggests a finite absorption in the QD medium that prohibited complete transparency in the system. In particular, the statement agrees well with the small absorption peak at resonance in the absorption profile shown in Fig. 2.4(b). Fig. 2.7 displays the individually normalized pulse for different propagation distances. Inspection says that the input pulse experiences delay and a little broadening during the propagation through the medium. The sole reason behind the pulse broadening is the dispersive nature of the system. In the frequency domain, a temporal pulse can be treated as a linear superposition of many travelling plane waves with different frequencies. These individual frequency waves gather different phases and move with varying velocities during the pulse propagation in a dispersive medium.

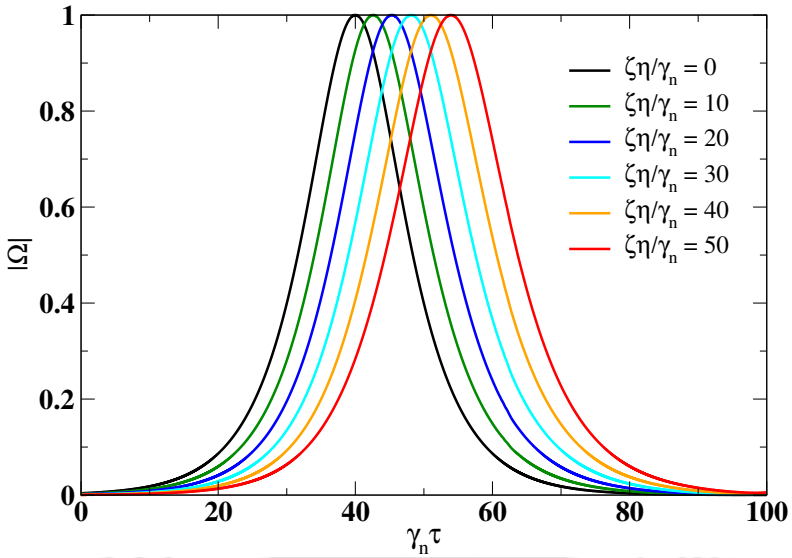

Figure 2.7: The Rabi frequency normalized with the individual peak value is plotted against retarded time at different propagation distances inside the medium at resonance condition $\Delta_c = 0$. All the other parameters are the same as Fig. 2.6. The figure depicts crucial features of pulse broadening for considerable propagation length in the medium by comparing the pulse width of the black and red line curves.

Therefore the pulse gets broader as the leading part(low frequency) moves faster, and the tailing end(high frequency) goes slower. In the QD system, the pure dephasing rate is also responsible for this broadening as it destroys the coherence. From Fig. 2.7, a distinct peak shift is observed while optical pulse propagating through the medium. This peak shift arises because of normal dispersive medium that induced slow group velocity of the optical pulse inside the medium. We adopt the analytical expression of time delay in the ideal case by considering $\sigma \gg 1/\tau_0$ reported earlier[113]. The analytical expression for time delay found to be $\gamma_n \tau_d = \alpha L \gamma_n \tau_0/4$. Here the absorption coefficient α is approximately 10 mm^{-1} calculated from the chosen parameters. Therefore the calculated analytical time delay $\gamma_n \tau_d \approx 15$ shows excellent agreement with the numerical result. The inhomogeneous level broadening σ plays an important role in pulse propagation dynamics. In our calculation, we are in the regime where the pulse width is greater than the inhomogeneous broadening time $\sigma\tau_0 \gg 1$. Therefore, the higher spread of the QD parameter σ leads to fewer QD resonantly interacting with the propagating pulse. This results in a negligibly small change in pulse shape. Alternatively, the effective QD density becomes less, indicating the lower value of the optical extinction parameter α. Henceforth a lower time delay is expected in the final output pulse due to its presence in the righthand term of Eq.(2.31). In Fig. 2.8, the final output pulse shape variation is presented for the three different QD spreads. The pulse delay decreases with an increasing QD broadening σ. On the other hand, the pulse peak value decreases with the lower QD spreads. This observation matches our previous prediction that higher σ produce a lower pulse delay in the medium. Also, more resonant QD absorb more energy from the pulse, resulting in a lesser peak value in the final pulse shape. Hence spread of the QD is also a determining factor for the shape and delay of the output pulse. Recalling the pulse area theorem again, we observe that the pulse area is almost constant throughout the propagation near 2π. The result is consistent because as the pulse amplitude decreases, the pulse width increases,

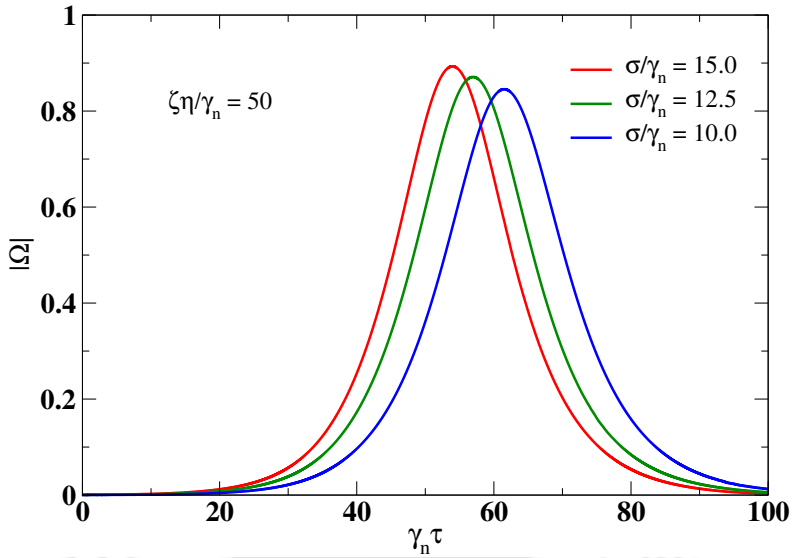

Figure 2.8: The normalized Rabi frequency displayed with retarded time after passing the medium for three different QD broadening σ. All the other parameters are the same as Fig. 2.6. The inhomogeneous broadening parameter σ affects pulse intensity and time delay during medium propagation. From the figure, we understand that a higher inhomogeneous broadening medium output pulse has a high intensity and low time delay, and the opposite is true for lower inhomogeneous broadenings.

maintaining the constant area under the curve. Therefore an absorbing QD medium can exhibit the SIT phenomena at low temperatures.

2.3.4 Phonon bath parameter dependence on SIT

In the simplified master equation (2.15), various phonon-induced scattering rates depend on both the system and bath parameters. Hence it is crucial to study the effect of phonon bath on the SIT dynamics. The phonon contribution comes to the picture in two ways; one from the reduced Rabi frequency, which depends on the $\langle B \rangle$ and the other is the phonon-induced scattering rates connected with the phonon spectral density function.

Therefore increasing phonon bath temperatures reduces the value of $\langle B \rangle$ and $\hbar\omega/2K_bT$ present in the expression of $\phi(\tau)$ given in the Eq.(2.13). Consequently, effective coupling between QD and applied field gets reduced, but the phonon-induced decay rates get enhanced. From Fig. 2.9, we notice that the final pulse shape experiences more deformation for higher temperatures. The peak of the output pulse is also very much reduced for the higher temperature T =20 K. Therefore, the bath temperature should be minimised to see the SIT in the QD medium.

Another controlling factor of the SIT is the interaction strength between the QD and the phonon bath. So the increment of system-bath coupling leads to the reduction of the coherence in the system. This statement is understandable by looking at the phonon correlation function shown in Eq.(2.13). Thus the final pulse shape for the equal propagation distances is significantly modified by the electron-phonon coupling constant, as shown in Fig. 2.10. Therefore we also have to ensure that the QD bath interacts weakly to get SIT phenomena in the QD medium.

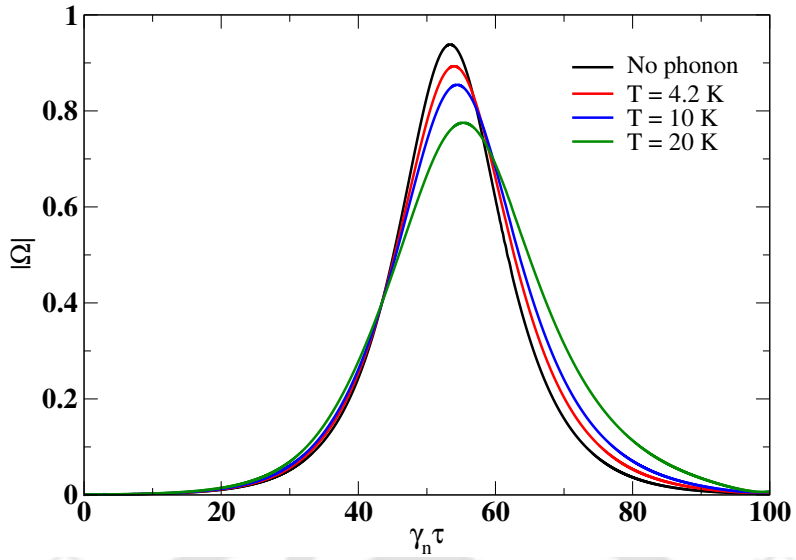

Figure 2.9: The plot of Rabi frequency envelope with time at a propagation distance $\zeta\eta/\gamma_n = 50$ for different phonon bath temperatures at resonance condition $\Delta_c = 0$. The common parameters are $\Theta(0) = 2\pi$, $\tau_0 = 6.373$ ps, $\gamma_n\tau_c = 40$, $\alpha_p = 0.03$ ps^2, $\omega_b = 1$ meV, $\gamma = \gamma_d = 2$ μeV(2 ns). The figure display four different configurations, system without a phonon bath (black) and with a phonon bath at a temperature T = 4.2K(red), 10K(blue), 20K(green). It is visible from here that temperature plays a vital role in the QD system as the higher temperature curves exhibit distortion in the pulse shape.

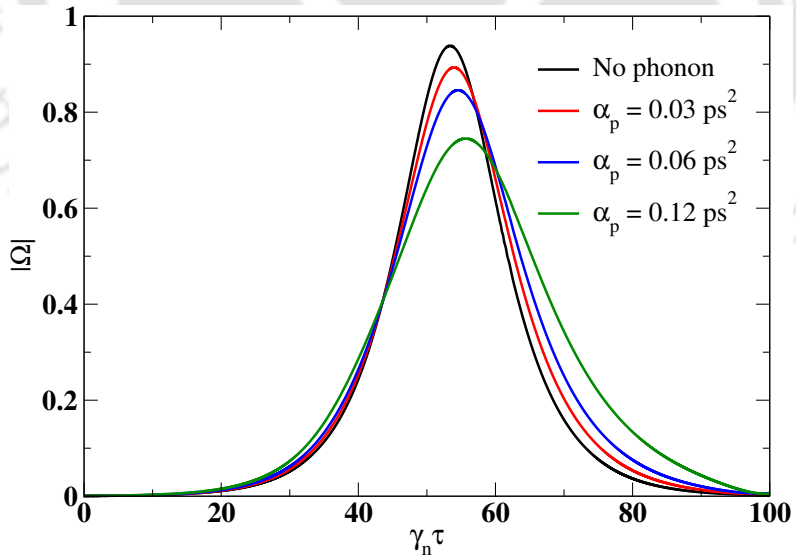

Figure 2.10: The Rabi frequency envelope with time at a propagation distance $\zeta\eta/\gamma_n = 50$ for different electron-phonon coupling strength α_p at resonance condition $\Delta_c = 0$. All the parameters are same as Fig. 2.9 except T = 4.2K and various electron-phonon coupling $\alpha_p = 0.03$ ps^2(red), 0.06 ps^2(blue), 0.12 ps^2(green). This plot explains the effects of QD-phonon coupling strength on pulse propagation dynamics. It shows the system becomes unstable when the phonon coupling is strong, generating a distorted pulse output at the medium end.

2.3.5 Higher pulse area and pulse breakup

Finally, we discuss the behaviour of a pulse propagating through the absorbing QD medium with a higher pulse area than 2π. Therefore we consider the next stable pulse area solution 4π for further investigation. The numerical result of the pulse propagation in both space and time is shown in Fig. 2.11. Unlike the 2π pulse case, here, the initial pulse breaks into two pulses as it travels through the medium. This phenomenon is also well explained by the pulse area theorem where $2n\pi$ pulse is split into n number of 2π pulses. Surprisingly, the initial pulse breakup into two pulses is not identical in shape. One pulse gets sharper, and the other gets broader in the time domain and adjusts the peak value such that the area under the curve is 2π. The broader pulse component shows a prominent time delay, whereas the sharper pulse component propagates with a tiny time delay. As a result, total pulse area is constant throughout the propagation distance near 4π.

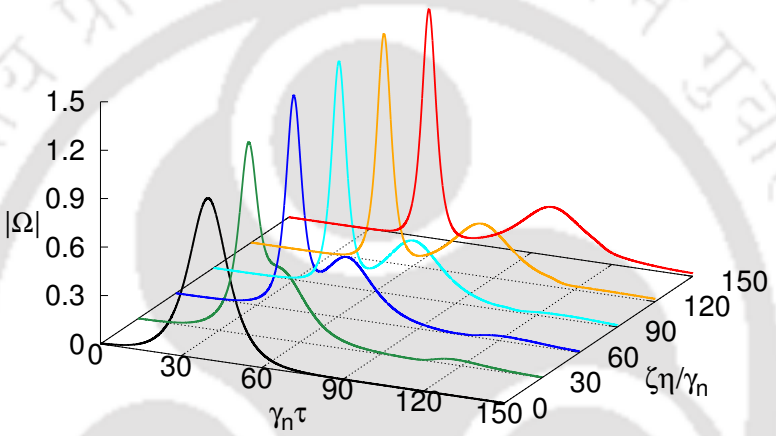

Figure 2.11: The propagation dynamics of a 4π area pulse in an absorbing QD medium as a function of both space and time at resonance condition $\Delta_c = 0$. All other parameters are same as Fig. 2.6. The pulse-breaking phenomenon is investigated in this figure. We sent a 4π secant pulse in the medium input, and then during the propagation, a single pulse started breaking into two parts and finally separated from each other. These two pulses have different shapes; one is sharply peaked, and the other is broader. According to theory, these pulses have 2π pulse area and sum up to the initial pulse area 4π.

2.4 Conclusions

We have investigated the SIT phenomena in an inhomogeneously broadened semiconductor QD medium. In our model, we have included the effect of phonon in the total Hamiltonian to describe the modified optical properties of QD in the presence of a thermal environment. We then adopted the polaron ME formalism to analytically derive the simplified ME with various phonon-induced decay rates. These phonon-induced scattering rates are plotted against detuning and time, which verify the presence of low-temperature asymmetry of phonon-induced pumping and decay in our system. We solve numerically the density matrix equation and Maxwell equation selfconsistently with suitable parameters. We observe that stable pulse propagation is possible in the QD medium with pulse area slightly higher than 2π, depending on the phonon bath temperature. The physical mechanism of the SIT is clearly understood by analyzing

the absorption and dispersion of the medium. The leading edge of the pulse gets absorbed by the medium, whereas the trailing edge of the pulse experience gain, hence the pulse shape remains intact and propagate through medium with short length. However, for longer propagation distances, we find that even though the pulse propagation through the medium is possible, the propagating pulse gets absorbed and broadened. The final pulse shape is preserved on exiting the medium. Increasing the phonon bath temperature and coupling produce more deformation in the final pulse shape, as it destroys the coherence in the system. Finally, we explore the propagation of a 4π pulse in the QD medium, which shows prominent pulse breakup phenomena reported earlier in the literature. Therefore our investigation ensures that a short pulse can propagate through the considered QD medium with a tiny change in shape. Hence, this work may have potential applications in quantum communication, quantum information, and mode-locking.

Chapter 3

Arbitrary vector beam generation

3.1 Introduction

The current chapter presents our second research problem. This problem is one step ahead of the previous research work and deals with a four-level system. Unlike optical pulse propagation, we investigate the light beam propagation in this four-level system. Hence, this considered scheme offers a new type of light with inhomogeneous polarisation called vector beam due to the nonlinear susceptibility present in the medium. The spatial polarization inhomogeneity of vector beam(VB) light has gained research interest in the optics community due to its fundamental applications, including high-density optical communication and super-resolution imaging. Such VB generation requires vector superposition of two orbital angular momentum-carrying Laguerre-Gaussian(LG) modes with orthogonal polarization [80, 81, 114]. The solution of the paraxial wave equation provides LG modes with an optical vortex structure and, therefore, capable of carrying the orbital angular momentum (OAM) [115]. This class of scalar beams with homogeneous polarisation distribution has been studied extensively in the literature. However, the VB is a relatively new and unexplored concept. Based on the OAM of each component, VBs are classified into two groups: full Poincare (FP) beams [80], and cylindrical vector (CV) beams [81]. The FP and CV beams consist of components with one nonzero OAM and two equal and opposite OAM, including examples such as lemon, star, web, radial, azimuthal, and spiral VB, respectively [77].

The CV beams have wide applications in the various fields of science and technology. The unique property of the CV beam demonstrates high numerical aperture (NA) focusing [116, 117], resulting in a significantly small spot size and beating the theoretical focusing limit for scalar beams [118]. Several other applications have also been reported, including optical trapping [119–121], super-resolution microscopy [122, 123], optical communication [124, 125], and high harmonic generation [126–128]. Subsequently, the theoretical prediction suggested a robust VB propagation through atmospheric turbulence [129–132]. The nonseparability of VB can be used to encode information for optical communication [133]. Further, VBs provide an infinite-dimensional Hilbert space platform associated with OAM to study quantum entanglement [134], quantum key distribution (QKD) protocols [135], and quantum cryptography [136] for high-security communication.

Due to the growing popularity of VB and its application in various fields, the VB

generation technique has also gained much attention. Conventionally, the VB generation requires an interferometer setup with precise alignment between two components [137, 138]. Some initial attempts on radially polarised beam generation methods rely on an image-rotating resonator [139] and double interferometer [140]. Several other systems consider the Sagnac-like interferometer [141], Twyman-Green method [142], and Wollaston prism [143]. In addition, several other platforms, like polarization gratings [144], optical fibers [145], and ring resonators [146] have been used for vector vortex beam generation. The current commercial production of VB utilizes advanced optical elements such as a spatial light modulator (SLM) [147], digital micromirror devices (DMDs) [148], and liquid crystal-based q-plates [149].

Although many different VB generation techniques are available, almost none match the current quantum architecture or satellite communication requirement due to their large setup and high power consumption. The recent development of nanotechnology has led to various systems for vortex beam generation, such as integrated silicon-chip-based vortex beam emitters [150], vortex vertical-cavity surface-emitting lasers (VCSELs) [151], angular gratings [152], micro-nano-OAM laser emitters [153], and various metasurface designs [154]. Other microsystems regarding vortex beams have been invented, such as vector vortex on-chip generators [155] and parallel OAM processors [156]. These vortex beams could be helpful for VB generation in a microstructure.

This chapter explores the possibility of arbitrary VB generation in a thin disk-shaped semiconductor quantum dot (QD) medium. In contrast, the QDs show full potential for this scheme because of the predetermined fabrication technology, tiny footprint, and ultra-low power consumption. Though the QD shows some remarkable advantages, lattice vibration is inevitable due to its sloid-state nature under the environment temperature. This temperature-dependent lattice vibration leads to the longitudinal acoustic phonon interaction with deformation potential. The phonon interaction with the QD exciton state results in various distinct features, such as dephasing [157], zero phonon line broadening [108], off-resonant cavity feeding [158], and Mollow triplet [159] observed. To study the system dynamics, polaron transformation and corresponding master equation have been considered for the phonon interaction [101–103]. In the literature, Hsu et al. [160] reported the controllable propagation of an optical field due to the cross-talk between first and third-order nonlinear susceptibility in a four-level diamond-like system. Later, a similar QD system shows the OAM transfer from the control field to the generated field via four-wave mixing (FWM) [161]. Motivated by these works, we can find a scheme where one part of the field gets absorbed by two-level absorption, and the other part experiences gain due to ladder transparency associated with the first, and third-order nonlinear susceptibility, respectively. In this scenario, two orthogonal polarisation components with the desired OAM have been generated, and their superposition leads to the arbitrary VB generation.

3.2 Model system

In this section, we present a simple and practical scheme for vector beam generation in a quantum dot(QD) medium. The medium comprises a few self-organized InGaAs QD layers separated by GaAs wetting layers created by the Molecular Beam Epitaxy (MBE) [162]. In the self-organized process, all the QDs are not identical in size. Thus,

different QD have different emission frequencies, which causes inhomogeneous broadening in the system. However, we have assumed all the QDs to be identical throughout this chapter to simplify our problem. Therefore, a single QD up to two excitons exhibits a four-level diamond-like energy level system. The system consists of a ground-state $|g\rangle$, two exciton states $|x\rangle$, $|y\rangle$ and a biexciton state $|u\rangle$ with corresponding energy $\hbar\omega_i$ where $i \in \{g, x, y, u\}$. Normally, two exciton states exhibit unequal energy due to the underlying asymmetry of QD. The frequency difference between two exciton states is known as fine structure splitting(FSS), defined by $\delta_x = \omega_x - \omega_y$. The biexciton state is a bound state of two exciton states. The energy required to form a biexciton state is known as biexciton binding energy, expressed as $\Delta_{xx} = \omega_x + \omega_y - \omega_u$. Various methods can reduce the FSS, such as thermal annealing and application of external electric and magnetic fields [163]. However, the uniaxial stress applied by the piezoelectric process is the most convenient technique for making it zero [164]. Our system considers the FSS zero to access the circular polarization basis of the QD transition to produce vector beam components. We also choose very high biexciton binding energy to differentiate the frequency between probe and control beams required for detection.

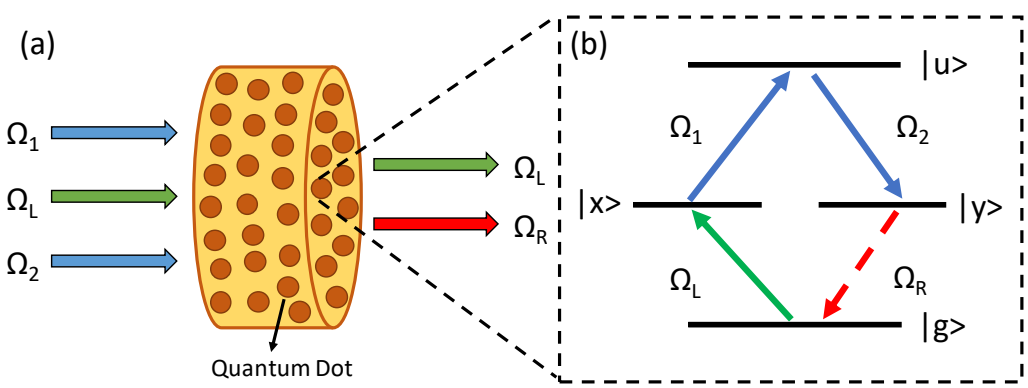

Figure 3.1: a) The schematic diagram of one weak probe field Ω_L and two strong control fields Ω_1, Ω_2 passing through a thin disc shape QD medium and generating an FWM field Ω_R. On the right-hand side, Ω_L represented by the green arrow is the transmitted probe field, and the two strong control field's presence is not shown in the figure due to far-detuned frequencies. b) The diamond-shaped energy level structure of QD interacting with the applied fields with corresponding Rabi frequencies.

In this scheme, one weak probe field $\vec{E}_L$ and two strong control fields $\vec{E}_1, \vec{E}_2$ propagate through a thin disc-shaped structure made of QD layers and generate a weak field $\vec{E}_R$ via four-wave mixing(FWM) process, as shown in Fig. 3.1(a). The corresponding electric fields are given by

$$\vec{E}_j(\vec{r}, t) = \hat{e}_j \mathcal{E}_{0j}(\vec{r}) e^{i(k_j z - \omega_j t)} + c.c., \quad j \in \{L, R, 1, 2\} \tag{3.1}$$

where $\mathcal{E}_{0j}(\vec{r})$ is the transverse variation of envelope, $k_j = \omega_j/c$ is the wave vector amplitude, ω_j is the frequency and $\hat{e}_j$ is the polarisation vector of the quasi-monochromatic field. It is worth mentioning that the optical field $j = L, 2$ and $j = R, 1$ have left and right circular polarisation matching with the corresponding QD transition. Therefore, the Rabi frequencies after both rotating wave and dipole approximation have the form $\Omega_j = -\vec{d}.\hat{e}_j \mathcal{E}_{0j}/\hbar$ where $j \in \{L, R, 1, 2\}$ and $\vec{d}$ is the dipole moment vector of the QD transition.

Fig. 3.1(b) shows the schematic energy levels of the QD interacting with the various optical fields. Initially, all the population is in the ground state $|g\rangle$. Then, we apply a weak probe field Ω_L and two strong control field Ω_1, Ω_2 to the $|g\rangle \rightarrow |x\rangle$, $|x\rangle \rightarrow |u\rangle$ and $|u\rangle \rightarrow |y\rangle$ transition, resulting in a small population redistribution from $|g\rangle \rightarrow |x\rangle \rightarrow |u\rangle \rightarrow |y\rangle$. Finally the weak four-wave mixing field Ω_R will be generated through $|y\rangle \rightarrow |g\rangle$ transition obeying the phase matching condition $k_R = k_L + k_1 - k_2$. In this process, the population returns to the ground state, and the generated field Ω_R carries the transferred OAM from the control beam. The non-zero intensity of Ω_L and Ω_R are required at the medium's output end to generate a vector beam. Therefore, we have considered a thin QD medium, which helps the weak probe Ω_L to reach the output end before being entirely absorbed by the medium. Hence, a fraction of the Ω_L is transmitted through the medium, and the coherently absorbed part is converted to Ω_R having OAM, resulting in a vector beam generation. Any semiconductor QD medium is inevitable to the surrounding lattice vibration caused by environmental temperature. Therefore, the QD system dynamics get modified due to the quantized mode of thermal vibration, i.e., acoustic phonon. The phonon bath consists of a collection of infinite closely spaced harmonic oscillators. Thus, annihilation and creation operators of the kth phonon mode with frequency ω_k will be b_k and $b_k^\dagger$. We consider the QD-phonon interaction in the total Hamiltonian to solve the QD dynamics in more detail.

As we have considered zero FSS in our system, the frequency of both the exciton will be equal $\omega_x = \omega_y$. Therefore, the applied field frequencies have the following structure $\omega_L = \omega_R = \omega_p$ and $\omega_1 = \omega_2 = \omega_c$ to remove the explicit time dependency from the interaction Hamiltonian. The interaction picture Hamiltonian with phonon interaction in a suitable unitary transformation frame is

$$\begin{aligned} H = & -\hbar\delta_p(\sigma_{xx} + \sigma_{yy}) - \hbar(\delta_p + \delta_c)\sigma_{uu} \\ & + \hbar\left(\Omega_L\sigma_{xg} + \Omega_1\sigma_{ux} + \Omega_2\sigma_{uy} + \Omega_R\sigma_{yg} + H.c.\right) \\ & + \hbar\sum_k \omega_k b_k^\dagger b_k + \sum_{i=x,y,u} \lambda_k\sigma_{ii}(b_k + b_k^\dagger), \end{aligned} \tag{3.2}$$

where $\delta_p = \omega_p - \omega_x$, $\delta_c = \omega_c - (\omega_u - \omega_x)$ are the detunings of corresponding QD transition and λ_k is the coupling strength. The QD projection operators defined by $\sigma_{ij} = |i\rangle\langle j|$ where $|i\rangle$ and $|j\rangle$ are the QD states. To deal with the entire order of phonon interaction, we choose the polaron transformation, $H' = e^P H e^{-P}$ where $P = \sum_{i=x,y,u}\sigma_{ii}\sum_k \lambda_k\left(b_k^\dagger - b_k\right)/\omega_k$. The transformed Hamiltonian decouple the system Hamiltonian H_S from the bath Hamiltonian H_B and the QD-bath interaction Hamiltonian H_I with renormalized Rabi frequency given by $H' = H_S + H_B + H_I$ where

$$H_S = -\hbar\Delta_p(\sigma_{xx} + \sigma_{yy}) - \hbar(\Delta_p + \Delta_c)\sigma_{uu} + \langle B\rangle X_g, \tag{3.3}$$

$$H_B = \hbar\sum_k \omega_k b_k^\dagger b_k, \tag{3.4}$$

$$H_I = \xi_g X_g + \xi_u X_u. \tag{3.5}$$

After this transformation, previous detunings are redefined into effective detunings Δ_p and Δ_c by summing up the additional polaron shift $\sum_k \lambda_k^2/\omega_k$. The polaron frame

system operators are

$$X_g = \hbar\left(\Omega_L\sigma_{xg} + \Omega_1\sigma_{ux} + \Omega_2\sigma_{uy} + \Omega_R\sigma_{yg}\right) + H.c. \tag{3.6}$$

$$X_u = i\hbar\left(\Omega_L\sigma_{xg} + \Omega_1\sigma_{ux} + \Omega_2\sigma_{uy} + \Omega_R\sigma_{yg}\right) + H.c., \tag{3.7}$$

and the phonon bath fluctuation operators are

$$\xi_g = \frac{1}{2}\left(B_+ + B_- - 2\langle B\rangle\right) \quad \xi_u = \frac{1}{2i}\left(B_+ - B_-\right), \tag{3.8}$$

where B_+,B_- are the phonon displacement operator. The expression for phonon displacement operators in terms of phonon creation and annihilation operators is $B_\pm = \exp[\pm\sum_k \frac{\lambda_k}{\omega_k}\left(b_k^\dagger - b_k\right)]$. Hence, the expectation value of this operator at a temperature T with a phonon spectral density $J(\omega)$ provides us $\langle B_+\rangle = \langle B_-\rangle = \langle B\rangle = \exp\left[-\frac{1}{2}\int_0^\infty d\omega \frac{J(\omega)}{\omega^2}\coth\left(\frac{\hbar\omega}{2K_bT}\right)\right]$, where K_b is the Boltzman constant. We have considered the experimentally verified phonon spectral density function $J(\omega) = \alpha_p\omega^3\exp[-\omega^2/2\omega_b^2]$ in our calculation, where the parameters α_p and ω_b are the electron-phonon coupling and cutoff frequency, respectively.

Now, to derive the polaron Master Equation(ME), we model a small system H_S placed in a large phonon reservoir H_B and interacting with the reservoir H_I. We apply the Born-Markov approximation to the system density matrix equation, which considers up to the second order in exciton-photon coupling. The phonon reservoir is chosen to be in thermal equilibrium to factorize the density matrix in the initial time. The time convolutionless ME for the reduced density matrix of a QD-field system in the presence of a phonon environment is given by

$$\begin{aligned}\dot{\rho} = &-\frac{i}{\hbar}[H_S,\rho] - \sum_{i=x,y}\left(\frac{\gamma_1}{2}\mathcal{L}[\sigma_{gi}] + \frac{\gamma_2}{2}\mathcal{L}[\sigma_{iu}]\right)\rho \\ &- \sum_{i=x,y,u}\frac{\gamma_d}{2}\mathcal{L}[\sigma_{ii}]\rho - \frac{1}{\hbar^2}\int_0^\infty d\tau \sum_{j=g,u}\times \\ &\left(G_j(\tau)[X_j(t), e^{-iH_S\tau/\hbar}X_j(t)e^{iH_S\tau/\hbar}\rho(t)] + H.c.\right),\end{aligned} \tag{3.9}$$

where γ_1, γ_2 are the spontaneous decay rates of exciton and biexciton states, γ_d refers to pure dephasing rate, and $G_{g/u}$ corresponding to the polaron Green functions. The pure dephasing process occurs due to the imperfectness of the system and is responsible for the zero-phonon line broadening in QD, which also depends on temperatures. The Green functions can be calculated from the correlation between bath fluctuation operators at time τ as $G_g(\tau) = \langle B\rangle^2\{\cosh[\phi(\tau)] - 1\}$, $G_u(\tau) = \langle B\rangle^2\sinh[\phi(\tau)]$ where phonon correlation $\phi(\tau) = \int_0^\infty d\omega\frac{J(\omega)}{\omega^2}\left[\coth\left(\frac{\hbar\omega}{2K_bT}\right)\cos(\omega\tau) - i\sin(\omega\tau)\right]$. The Lindblad super-operator $\mathcal{L}$ in the ME has the well-known form $\mathcal{L}[\mathcal{O}]\rho = \mathcal{O}^\dagger\mathcal{O}\rho - 2\mathcal{O}\rho\mathcal{O}^\dagger + \rho\mathcal{O}^\dagger\mathcal{O}$ where $\mathcal{O}$ represent any arbitrary operator.

According to the Maxwell equation, any electromagnetic field interacting with QD creates induced polarisation $\vec{P}(z,t)$ due to its dipole alignment. This induced polarisation is associated with the coherence term of density matrix elements ρ_{xg} and ρ_{yg} expressed as $\langle x|\rho|g\rangle$, $\langle y|\rho|g\rangle$ for two weak probe fields Ω_L, Ω_R. The induced polarization amplitude is written as

$$\mathcal{P}_{xg}(z,t) = Nd\rho_{xg}, \tag{3.10}$$

$$\mathcal{P}_{yg}(z,t) = Nd\rho_{yg}, \tag{3.11}$$

where N is the QD volume number density. By applying slowly varying envelope approximation to the Maxwell wave equation and making a frame transformation $\tau = t - z/c, \zeta = z$, we get the propagation equation

$$\frac{\partial}{\partial\zeta}\Omega_L(\zeta,\tau) = i\eta\rho_{xg}, \tag{3.12}$$

$$\frac{\partial}{\partial\zeta}\Omega_R(\zeta,\tau) = i\eta\rho_{yg}, \tag{3.13}$$

where the coupling constant $\eta = -3N\lambda^2\gamma_1/4\pi$ and λ is the central wavelength of the QD transition. We solve the master equation (3.9) and propagation equation simultaneously to calculate the generated field numerically using Quantum Optics Toolbox[165] in MATLAB. Now, we define the transmitted and generated electric fields $\mathcal{E}_L$, $\mathcal{E}_R$ at the output end of the medium. The generated vector beam (VB) in a cylindrical coordinate system is

$$\vec{E}(r,\phi,z) = \mathcal{E}_L(r,\phi,z)\hat{e}_L + \mathcal{E}_R(r,\phi,z)\hat{e}_R, \tag{3.14}$$

where $\mathcal{E}_L(r,\phi,z) = \cos(\alpha)LG_0^{l_L}$, and $\mathcal{E}_R(r,\phi,z) = e^{i\theta}\sin(\alpha)LG_0^{l_R}$ are the Laguerre-Gaussian modes of left and right circular polarization with two controlling parameters, α and θ known as relative amplitude and phase. The considered Laguerre- Gaussian modes with zero radial index $LG_0^{l_i}(i \in L, R)$ has the form

$$LG_0^{l_i}(r,\phi,z) = E_i^0\sqrt{\frac{2}{\pi|l_i|!}}\frac{w_0}{w(z)}\left(\frac{r\sqrt{2}}{w(z)}\right)^{|l|}\exp\left[-\frac{r^2}{w^2(z)}\right]$$
$$\times\exp\left[\frac{ik_i^f n_i r^2 z}{2\left(z^2+n_i^2 z_R^2\right)}\right]e^{il_i\phi - i(|l|+1)\eta(z)+ik_i^f n_i z}. \tag{3.15}$$

Used notations are the maximum field amplitude E_i^0, angular momentum l_i, azimuthal angle ϕ, Rayleigh length $z_R = k_i^f w_0^2/2$, beam waist w_0, wave number k_i^f, beam waist at z distance $w(z) = w_0\sqrt{1+z^2/n_i^2 z_R^2}$, refractive index n_i, Gouy phase $(|l|+1)\eta(z)$ where $\eta(z) = \tan^{-1}(z/n_i z_R)$. We adopted the Stokes parameter formalism in the circular polarization basis to visualize the polarization distribution in a transverse plane given by

$$S_0 = |\mathcal{E}_L|^2 + |\mathcal{E}_R|^2,\ S_1 = 2\mathrm{Re}[\mathcal{E}_L^*\mathcal{E}_R],$$
$$S_2 = 2\mathrm{Im}[\mathcal{E}_L^*\mathcal{E}_R],\quad S_3 = |\mathcal{E}_L|^2 - |\mathcal{E}_R|^2. \tag{3.16}$$

With the help of Stokes parameters, the ellipticity χ and orientation ψ of the degree of polarization at any given point can be calculated as follows

$$\frac{S_1}{S_0} = \cos(2\chi)\cos(2\psi), \frac{S_2}{S_0} = \cos(2\chi)\sin(2\psi), \frac{S_3}{S_0} = \sin(2\chi). \tag{3.17}$$

We can derive the expression for ellipticity χ and orientation ψ in terms of the stokes parameters by using Eq.3.16 and Eq.3.17 and are given by

$$\chi = \tfrac{1}{2}\sin^{-1}\left(\tfrac{S_3}{S_0}\right) = \tfrac{1}{2}\sin^{-1}\left(\tfrac{|\mathcal{E}_L|^2-|\mathcal{E}_R|^2}{|\mathcal{E}_L|^2+|\mathcal{E}_R|^2}\right), \tag{3.18}$$

$$\psi = \tfrac{1}{2}\tan^{-1}\left(\tfrac{S_2}{S_1}\right) = \tfrac{1}{2}\tan^{-1}\left(\tfrac{Im[\mathcal{E}_L^*\mathcal{E}_R]}{Re[\mathcal{E}_L^*\mathcal{E}_R]}\right). \tag{3.19}$$

3.3 Vector beam generation

In order to study the VB generation in a QD medium, we have considered some experimental parameters that are compatible with our model system. The QD structure possess volume number density $N = 1.5\times10^{19}m^{-3}$. The phonon bath temperatures T = 0, 5, 10, 20 K gives $\langle B\rangle = 1.0, 0.90, 0.84, 0.73$ for phonon spectral distribution parameters $\alpha_p\gamma_n^2 = 1.42 \times 10^{-3}$ and $\omega_b = 10\gamma_n$ with normalization frequency $\gamma_n = 100\,\mu eV$. The relaxation and dephasing rates of the QD are taken to be $\gamma_1 = \gamma_2 = \gamma_d = \gamma = 0.01\gamma_n$. The scheme comprises one weak applied field Ω_L and two strong control fields Ω_1, Ω_2 with the general LG beam structure. According to our definition, the Rabi frequencies associated with the following fields can be written as

$$\Omega_L(r,\phi,z=0) = \Omega_{0L}\left(\frac{r\sqrt{2}}{w_L}\right)^{|l_L|} e^{-\frac{r^2}{w_L^2}} e^{il_L\phi}, \tag{3.20}$$

$$\Omega_1(r,\phi,z=0) = \Omega_{01}\left(\frac{r\sqrt{2}}{w_1}\right)^{|l_1|} e^{-\frac{r^2}{w_1^2}} e^{i(l_1\phi+\theta_1)}, \tag{3.21}$$

$$\Omega_2(r,\phi,z=0) = \Omega_{02}\left(\frac{r\sqrt{2}}{w_2}\right)^{|l_2|} e^{-\frac{r^2}{w_2^2}} e^{i(l_2\phi+\theta_2)}, \tag{3.22}$$

where r, ϕ corresponds to radial distance, azimuthal angle in cylindrical coordinates along with the beam waist w_i and OAM l_i $i \in \{L, 1, 2\}$. In general, we incorporated the constant relative phase of the two control fields compared to the applied field, denoted by θ_1 and θ_2. Subsequently, all the beam waist in the definition of three LG beams have normalized with a common beam waist w with the chosen value of 100 μm. In a similar atomic configuration, the effect of third-order nonlinearity has been studied extensively for field propagation dynamics, both theoretically [160] and experimentally [166]. It has been predicted that the interplay between the first and third-order nonlinearity of the medium leads to a controlled field propagation. Motivated by this work, a recent study shows the structured beam generation and OAM transfer between fields via FWM process [167]. In this direction, the implementation of the spatially structured transparency and transfer of optical vortices via four-wave mixing in a QD nanostructure was reported recently [161]. According to this study, the Rabi frequency of the generated FWM fields depends on the one applied field and two control fields as $\Omega_R \propto \Omega_L\Omega_1\Omega_2^*$. From this equation, it is clear that the OAM of the generated field will be $l_R = l_L + l_1 - l_2$. Now, we can make our first attempt to generate a lemon VB, where the OAM has to be $l_L = 0$ and $l_R = 1$. Therefore to fullfill this requirement, we have chosen $l_L = 0, l_1 = 1, l_2 = 0$. Although the OAM of the left and right circular components of the VB are generated correctly, now we have to focus on the relative strength between the two components denoted by the angle α.

In Fig. 3.2(a), we display the weak applied field intensity distribution variation during propagation inside the QD medium. The applied field with OAM $l_L = 0$ shows a Gaussian distribution along the x-axis at $z = 0$. Consideration of only the x-axis is justifiable because of the radial symmetry of the applied field. We notice that the field intensity rapidly decreases with increasing propagation distance and becomes zero for long distances. This behavior follows the well-known Beer's law of weak field absorption in a two-level medium. The presence of the two-level absorption term in the susceptibility explains this kind of feature at resonance conditions. As

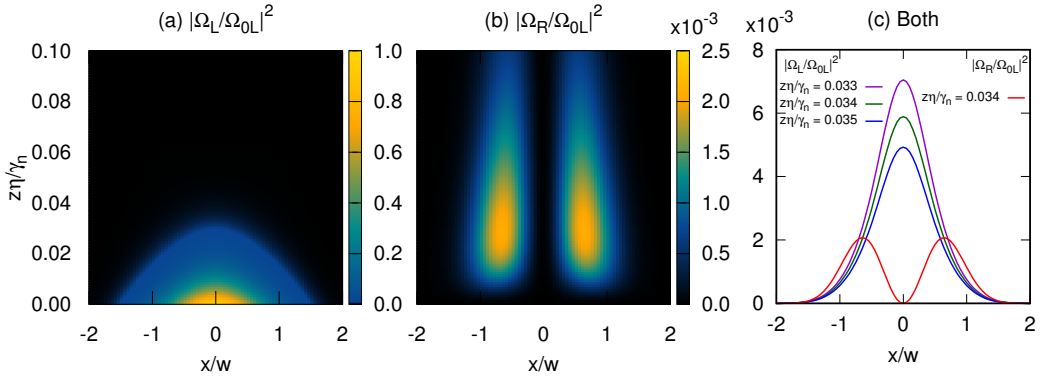

Figure 3.2: The intensity distribution of the applied left circular and generated right circular polarised field along the x-axis and its variation with the propagation distance $z\eta/\gamma_n$. a) Applied field intensity variation as a function of propagation distance for an LG beam with OAM l_L =0. b) Generated FWM field intensity variation corresponding to the propagation length with a signature of OAM $l_R = 1$. c) The relative intensity comparison between the two polarisation components for some specific $z\eta/\gamma_n$ satisfying the lemon VB condition. The generated intensity shows identical behavior for all three different propagation lengths; therefore, it is presented for only one propagation length. The considered applied field Rabi frequencies are $|\Omega_{0L}| = 0.005\gamma_n$, $|\Omega_{01}| = 0.01\gamma_n$, $|\Omega_{02}| = 0.05\gamma_n$ resonantly coupled with the desired transition $\Delta_p = \Delta_c = 0$. The suitable beam waist of the three fields is $w_L = 1.0w$ and $w_1 = w_2 = 1.7w$ at a phonon bath temperature T = 5K. The relative phases are $\theta_1 = \theta_2 = 0$.

the medium acts as a strong absorber for the weak applied field Ω_L, the length of the medium should be small enough to get a viable output intensity at the medium end. Therefore, the absorbed energy transfers a small amount of the QD population from the ground state $|g\rangle$ to the exciton state $|x\rangle$. The first control field Ω_1 couples the transition between $|x\rangle \leftrightarrow |u\rangle$ with OAM $l_1 = 1$ exchange the population to the biexciton state $|u\rangle$. Subsequently, the second control field does not carry any OAM couple the transition $|u\rangle \leftrightarrow |y\rangle$ resulting in the redistribution of the population into $|y\rangle$ state. In this whole process, the third-order nonlinearity of the QD medium couples to the three fields and produces a new field via the FWM process with the following structure $\Omega_R \propto \Omega_L\Omega_1\Omega_2^*$. From this expression, we notice that the OAM of the first control field $l_1 = 1$ transferred to the generated field Ω_R as OAM $l_R = 1$. Fig. 3.2(b) shows the variation of the intensity distribution normalized with the applied field peak intensity along the propagation length for the generated field. We notice that the generated field intensity becomes zero at $z = 0$ as the production of Ω_R is not started. After the propagation of a certain distance inside the QD medium, the generation of the Ω_R started and hence began to show the intensity. Most importantly, one can notice that the intensity distribution shows a doughnut shape along the x-axis. It is understandable from the fact that the transfer of the OAM $l_1 = 1$ to the generated field creates such a structure. Even though we can generate a desired OAM carrying field from this system, the generated field's intensity is much weaker than the applied field because of the third-order nonlinearity. Looking at the propagation axis, we understand that the generated field intensity grows from zero to a maximum value and then gradually decreases to zero for larger distances due to the medium absorption.

We consider the medium length near $z\eta/\gamma_n = 0.03$ to maximize the generated output intensity. Fig. 3.2(c) depicts the variation of both the applied and generated field for a few specific propagation distances. It is worth mentioning that the relative

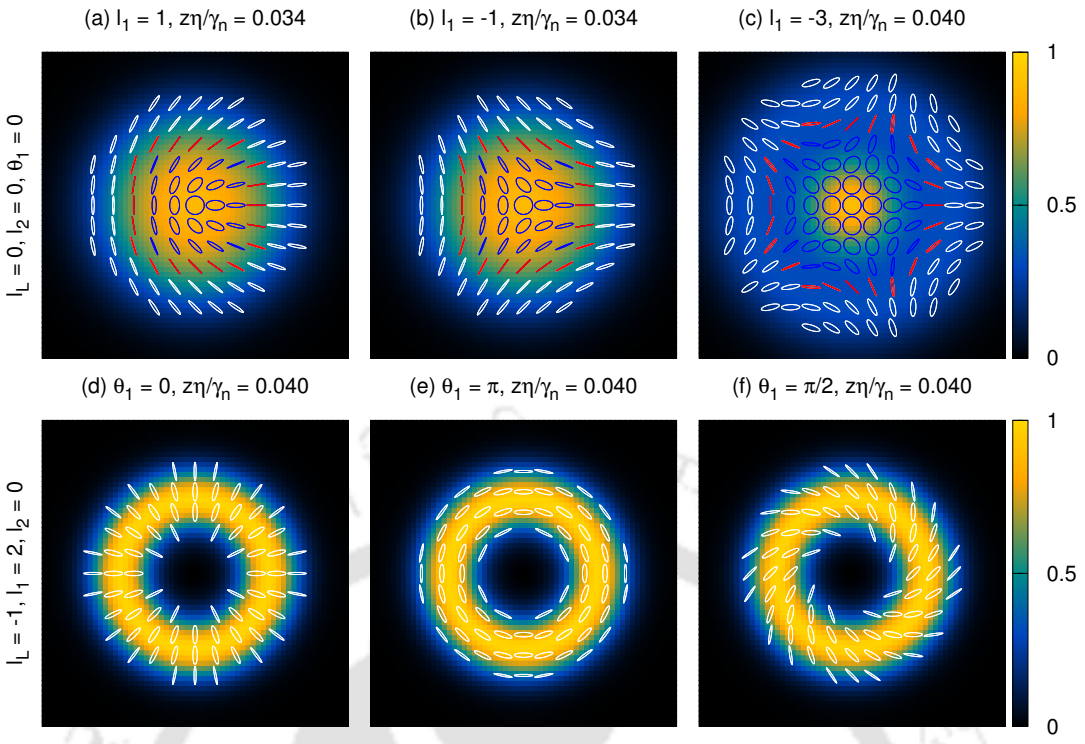

Figure 3.3: This figure illustrates the intensity and polarisation distribution for various generated VB in a transverse plane. The blue, white, and red color ellipse/circle/line corresponds to the left and right elliptic/circular and linear polarisation. All other parameters are the same as Fig. 3.2 except the beam waist for (a)-(c) $w_L = 1.0w$ and $w_1 = w_2 = 1.7w$ and (d)-(f) $w_L = 0.8w$ and $w_1 = w_2 = 1.0w$. In the first row, we have changed the orbital angular momentum of the first control field l_1 to match the correct combination for the (a) lemon, (b) star, and (c) web vector beam generation. For subplot (a)-(b), the propagation length is the same, which provides a correct intensity ratio of roughly 3:1 for the mentioned VB generation. On the contrary, (c) requires an intensity ratio of 5:1, which is achieved by increasing the propagation length. In the second row, we only vary the first control field phase θ_1 with all other parameters fixed and get the various cylindrical vector beams (d) radial, (e) azimuthal, and (f) spiral. This control field phase produces a relative phase between the two components of the VB, resulting in such cylindrical VB generation.

intensity between the two components is an essential requirement in producing VB. For a lemon VB, the required peak intensity of the two components is roughly 3:1. We observed that the applied intensity decreases rapidly for three different propagation distances, but the generated field becomes constant. Among all the three distances, $z\eta/\gamma_n = 0.034$ best fit with the actual lemon VB component distribution. Thus, our scheme can produce a lemon VB by applying three fields through a QD medium of width $z\eta/\gamma_n = 0.034$.

From the previous study, it is clear that all the controlling parameters of the general VB in Eq.(3.14) are accessible in this scheme. We can choose any arbitrary OAM of l_L, l_1 and l_2 for the applied and control fields to generate a field carrying OAM $l_R = l_L + l_1 - l_2$. Thus, any required OAM for the two components of a VB is achievable by considering a suitable combination of the three fields. The relative intensity between two VB components depends on α could be controlled by the propagation distance in our system. Further, the relative phase θ between two VB components can be

regulated by changing the constant relative phase $\theta_1 - \theta_2$ between two control fields. Fig. 3.3 showcases the generated VB intensity and polarisation on a transverse plane with color plot and ellipse calculated from various stokes parameters. Therefore, each panel exhibits the distribution on the xy plane for a specific propagation distance with different sets of parameters. Some of the most popular full Poincare VBs are presented in Fig. 3.3(a)-(c). For all the full Poincare VBs, we have only changed the OAM of the first control field by setting all other OAM and phase $l_L = l_2 = 0$, $\theta_1 = \theta_2 = 0$. In Fig. 3.3(a), we observe a well-known lemon VB pattern for the first control field OAM l_1=1 and a propagation distance of $z\eta/\gamma_n = 0.034$. This result is consistent with the previous analysis made on the lemon VB generation. The first panel of Fig. 3.3 shows flat-top Gaussian-like background intensity distribution because of the resultant intensity defined by the Stokes parameter S_0 of two VB components by looking at Fig. 3.2(c). The left circular polarisation components of the generated VB do not carry any OAM exhibit Gaussian distribution peaking at the center. In contrast, the generated right circular polarisation component is zero near the center because of OAM l_R =1. Noticeably, the center of the VB shows a clear signature of the left circular polarisation denoted by blue ellipses. Further, going towards the edges, the Gaussian intensity decreases, but the doughnut intensity increases, resulting in linear polarisation and right circular polarisation. Overall, the inhomogeneous polarisation distribution looks like a lemon, and the total OAM is 1, named lemon VB under the FP VB category. In Fig. 3.3(b), we have considered everything similar to the previous panel except the first control field OAM $l_1 = -1$, which transferred to the generated field OAM as $l_R = -1$ satisfy the star VB configuration. In star VB, the inhomogeneous polarisation distribution shows symmetry around three equally separated lines meeting at the center. The propagation distance is precisely the same as lemon vector beams because we have only changed the sign of the OAM, which does not affect the intensity distribution. In Fig. 3.3(c), we have displayed generated web VB by considering the control field OAM $l_1 = -3$ with proper propagation distance $z\eta/\gamma_n$ = 0.040. This configuration differs entirely from the previous two, as we now consider the higher OAM to produce $l_R = -3$. For LG beams, the normalization factor contains $\sqrt{|l_i|!}$ on the denominator is now effective for $|l_i| > 1$. Therefore, the relative intensity between the web VB's left and right circular components has to obey an approximate ratio of 5:1 to produce the desired VB. The condition for the web VB is satisfied by taking a longer propagation distance in the QD medium compared to the others. The intensity distribution depicts a clear Gaussian peak at the center surrounded by the much lower-intensity doughnut distribution. Subsequently, the polarisation distribution shows a web-like structure popularly known as web VB. Now, we move on to the other class of the VB, which has equal and opposite OAM-carrying components known as cylindrical VB. Fig. 3.3(d)-(f) presents three well-known cylindrical VBs generated from this scheme at a propagation distance $z\eta/\gamma_n = 0.040$. Unlike the previous case, all the parameters are fixed here $l_L = -1, l_1 = 2, l_2 = 0, \theta_2 = 0$ except the first control field phase θ_1. Therefore, the cylindrical VB can be produced by only changing the θ_1. One important thing to notice here is that the applied field OAM $l_L = -1$ and the first control field OAM $l_1 = 2$ produces a resultant OAM $l_R = 1$ satisfy the condition for CVB. Fig. 3.3(d)-(f) depicts the radial, azimuthal, spiral symmetry in polarization distribution on a transverse plane for $\theta_1 = 0, \pi, \pi/2$, named radial azimuthal, spiral CVB. These CVBs have various applications in modern science and technology. For all three CVBs, we notice that the center dark spot is bigger than the

conventional CVB. This behavior comes from the first control field OAM $l_1 = 2$ because the resultant field is the product of the Ω_L and Ω_1, which left the signature of $l_1 = 2$ in the intensity distribution. Also, the eccentricity of the polarisation ellipse changes from higher to lower intensity region of the bright ring because of the nonidentical intensity distribution between the Ω_L and Ω_R. Therefore, we could generate any arbitrary VB in this configuration by changing the controlling parameters.

3.4 Polarization rotation

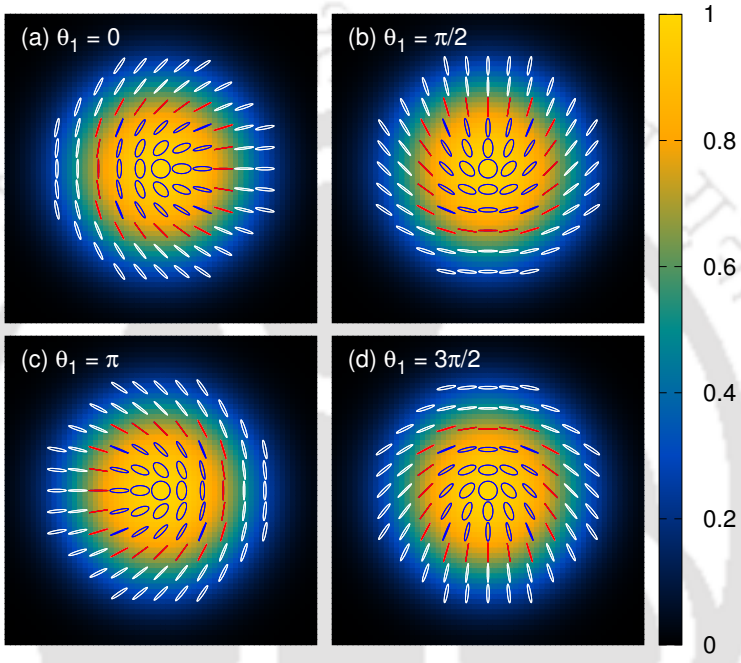

Figure 3.4: Controllable polarisation rotation of generated lemon VB by changing the first control field phase θ_1. All other parameters are the same as Fig. 3.2. This figure illustrates control field phase-induced polarisation rotation phenomena in a lemon VB. The first control field phase introduces an additional rotational angle θ_1 to the existing phase structure of the angular momentum-carrying beam, resulting in the rotation of the polarisation structure.

Fig. 3.4 displays the polarization distribution rotation of the generated lemon VB for four different values of the first control field phase angle θ_1. For a lemon VB, the OAM of the left and right circular polarization components are $l_L = 0$ and $l_R = 1$. Therefore, the generated field creates a spatially dependent structured transparency in the QD medium's susceptibility, having one absorption and one gain peak. These peaks are identical and placed side by side with a common zero line passing through the center. The control field relative phases are defined by setting the reference point at the applied field Ω_L phase. Therefore, the second control phase $\theta_2 = 0$ indicates the transfer of θ_1 phase to the generated field Ω_R. For Fig. 3.4(a), the relative phase between two components of the VB is zero, resulting in a lemon polarisation distribution pointing to the right side. By changing the phase $\theta_1 = \pi/2$, the gain and absorption peak of the QD medium rotates ninety degrees clockwise in the transverse plane. This spatially dependent transparency rotation is responsible for the polarisation rotation of the lemon VB pointing upward, as shown in Fig. 3.4(b). Similarly, we can observe

that the polarisation rotates accordingly for $\theta_1 = \pi, 3\pi/2$.Therefore, the scheme is capable of any arbitrary polarisation rotation of a VB by tuning the first control field phase θ_1.

3.5 Effect of temperature on VB generation

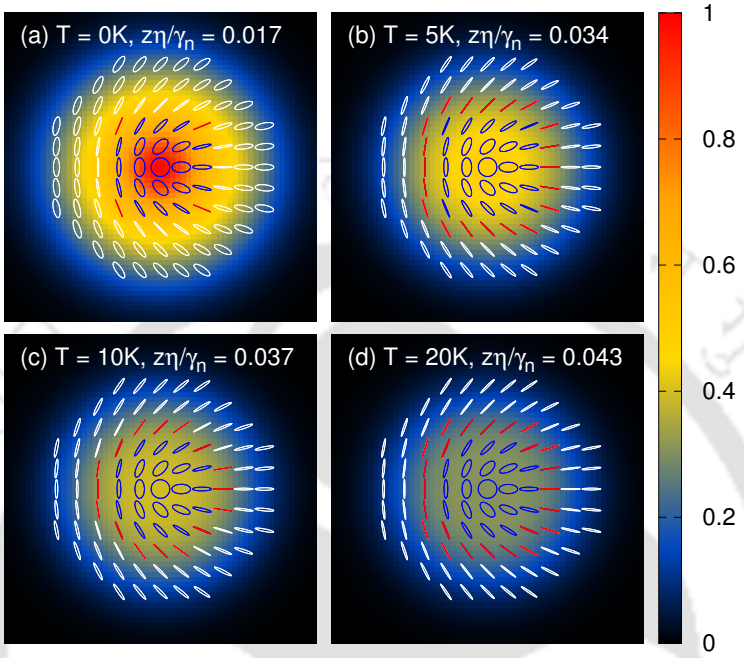

Figure 3.5: The figure illustrates the variation of transverse intensity and polarization distribution of a generated lemon VB for various phonon bath temperatures. All other parameters are the same as Fig.3.2. The temperature always affects quantum light generation as the QD emitter's emission property dramatically depends on temperature variation. This figure explores that lower temperatures produce a higher intensity and higher temperatures produce a low-intensity VB. We also notice that the VB generation requires a longer propagation length through the medium for higher temperatures.

Fig. 3.5 displays the phonon bath temperature dependence on the VB generation. As mentioned earlier, the bath temperature of the system plays a vital role in the system dynamics. For increasing temperature, the renormalized Rabi frequency $\Omega_i\langle B\rangle$ gets reduced due to a smaller value of $\langle B\rangle$. Higher temperatures also introduce more dephasing in the system, which leads to the reduction of quantum coherence. As a result, phonon-induced decay rates get enhanced, resulting in low-intensity right circular polarisation component generation. Fig. 3.5 (a) shows the lemon VB generation without phonon bath contribution in the Hamiltonian. We notice that the intensity of the generated beam is higher than all other temperatures. The ratio between the two components satisfies the lemon VB configuration for a small propagation distance. In the case of nonzero temperatures, the intensity of the generated VB diminished with increasing temperatures T = 5, 10, 20 K as depicted in Fig. 3.5 (b)-(d). Accordingly, the system requires a longer propagation distance to satisfy the correct ratio between the VB components. From this analysis, it is clear that high temperatures reduce the output intensity of the generated VB and demand a long medium propagation length to produce it.

3.6 Conclusions

We have demonstrated a simple and compact system for generating arbitrary vector beams in a QD medium. This system incorporates the phonon interaction in the system Hamiltonian to provide a more realistic result. To deal with the phonon interaction, we make a polaron transformation on the total Hamiltonian and then find the master equation for the system density matrix. In this scheme, we can generate any arbitrary VB because of the access of the controlling parameters. We have shown that one can regulate the polarisation rotation of the generated VB by changing the first control field phase. We have also explicitly studied the effect of the temperature on the VB generation. This scheme could potentially be applied to chip-based photonic circuits and free-space optical satellite communication.

Chapter 4

Nondegenerate two-photon laser

4.1 Introduction

In the previous two chapters, we have considered quantum emitters up to four energy levels and solved the problem semiclassically. However, this chapter discusses the full quantum mechanical theory of the further complex problem of a four-level system interacting with a two-mode cavity. This configuration is suitable for micro or nanolaser generation. The quantum theory of maser was established in the late 20th century [19, 168], in which the gain medium was modelled as a quantum emitters interacting with the quantized cavity field. The experimental demonstration of the single atom maser using Rydberg atoms, was reported by Meschede *et al.* [169]. Since then, with the developments of quantum optics, single-atom lasers have been realized using several other quantum emitters coupled with different high-quality cavities, including trapped ions [170], trapped single atom [171], superconducting qubits [172, 173], and quantum dots [174–176]. Scalable “on-chip" single emitter laser with ultra-low threshold power has wide application in modern quantum technology such as quantum information processing, quantum computing, quantum metrology, and analysis of complex quantum network [177–179].

Semiconductor Quantum Dots (QDs) have emerged as a potential candidate for the generation of “on-chip" quantum light sources. Owing to recent developments, different types of high finesse low mode volume structures like toroidal, micropillar, and photonic crystal cavities have also been fabricated. Existing technology can also supports the growth of a QD inside a microcavity at a predetermined location [180–183]. Various single emitter microlasers using QDs embedded in a photonic crystal cavity [176, 184–187] and QDs coupled with coplanar microwave cavity have been recently realized [175, 188, 189]. In solid-state semiconductor systems, lattice vibrations are inevitable due to the finite ambient temperature. Particularly, longitudinal acoustic phonon interactions with the QD exciton states significantly modify the system dynamics. The interactions between phonon modes and exciton lead to dephasing in coupled dynamics of exciton-photon interaction as well as off-resonant cavity mode feeding [93, 94, 190–192]. Therefore, the generation efficiency of highly indistinguishable single photons [193, 194] and a pair of entangled photons [195] from a single QD depends on the phonon bath temperature. As a result, the microlaser dynamics are significantly modified. Phonon-assisted population inversion in QDs using an incoherent and coherent pump has also been observed [196, 197].

In the single-emitter single-photon laser, the lasing action occurs due to the stimulated emission of a single-photon in cavity mode. Similar to single-photon lasers, it has been predicted that the stimulated two-photon emission could also be used for two-photon lasing when single-photon emission is negligible in the gain medium [198]. In this context, a theoretical study predicted that the phonon bath could lead to a correlated two-photon emission from a single QD [199]. Successively, the two-photon laser has been demonstrated by Gauthier *et al.* [200]. They have used strongly driven two-level atoms as the gain medium and a weak field having frequency resonant to one of the sidebands as probe. The degenerate two-photon lasing in a single QD using an effective Hamiltonian approach has recently been proposed [201, 202].

A degenerate two-photon maser can be achieved by using Rydberg atoms passing through a cavity [203]. In a separate development, the theory of a nondegenerate two-mode two-photon laser has been proposed for inverted atoms passing through a cavity [204]. It has been predicted that in such a laser, one mode can enhance or reduce gain in the second mode. Further, such a laser can display entanglement between a large number of two-mode photons [205]. In recent years, there has been some experimental success in the construction of a two-mode microlaser [206], where two orthogonal polarized modes in a micropillar cavity are coupled with exciton states having angular momenta ± 1. A strong correlation between the two modes and a superthermal photon bunching has been predicted in such two-mode lasers [207]. Though some success has been accomplished for two-photon and two-mode lasers, the nondegenerate two-photon laser has not yet been investigated in the QD-cavity system. In this chapter, we propose a scheme for a nondegenerate two-photon laser using a single QD embedded in a two-mode microcavity.

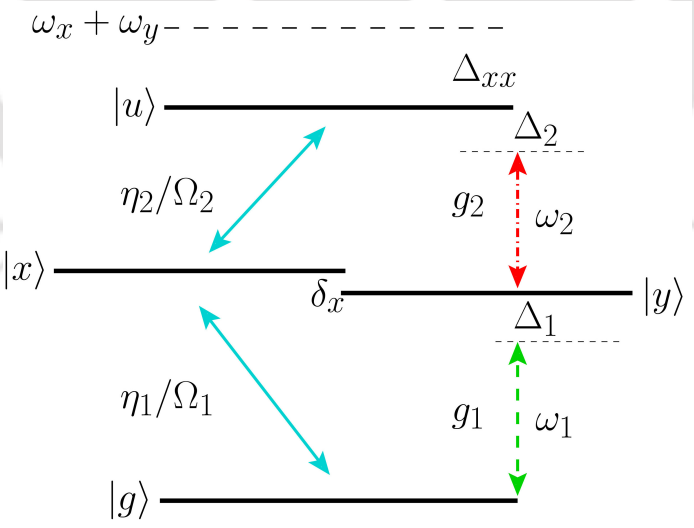

Figure 4.1: The schematic energy level diagram for the QD-cavity model. Left solid blue arrows indicating incoherent (coherent) pumping from $|g\rangle \rightarrow |u\rangle$ with pumping rates η_1 (Ω_1) and η_2 (Ω_2). Right dashed green and dashed dot red arrows indicating cavity coupling with $|y\rangle \rightarrow |g\rangle$ and $|u\rangle \rightarrow |y\rangle$ with coupling constant g_1 and g_2 and frequencies ω_1 and ω_2. Here Δ_{xx} and δ_x stand for the biexciton binding energy and fine structure splitting energy between two exciton states. The Δ_1 and Δ_2 are the effective detunings for the first and second cavity modes.

4.2 Model system

This work investigates the feasibility of two-mode two-photon microlaser and entanglement generation in a semiconductor microcavity within the framework of cavity quantum electrodynamics. We consider a system composed of a single QD embedded in a two-mode high-quality photonic microcavity. In the neutral QD, the bound state of the electron-hole pair produces discrete energy levels. The relevant energy levels of the QD consist of a biexciton state $|u\rangle$, two single exciton states $|x\rangle$, $|y\rangle$, and a ground state $|g\rangle$, respectively, as shown in Fig. 4.1. The frequencies of the excited states $|u\rangle, |x\rangle$ and $|y\rangle$ are denoted by ω_u, ω_x and ω_y, respectively. The energy difference between two exciton states is denoted by fine-structure splitting $\delta_x = \omega_x - \omega_y$ and biexciton binding energy is defined by $\Delta_{xx} = \omega_x + \omega_y - \omega_u$. The QD energy levels form a diamond-like structure due to an optically forbidden transition between two bright exciton states.

It is clear from Fig. 4.1 that two transition pathways exist between $|u\rangle$ and $|g\rangle$: one path is described by $|u\rangle \leftrightarrow |x\rangle \leftrightarrow |g\rangle$ and another represented by $|u\rangle \leftrightarrow |y\rangle \leftrightarrow |g\rangle$. We choose the quantum path $|u\rangle \leftrightarrow |x\rangle \leftrightarrow |g\rangle$ for pumping by H-polarized fields to produce population inversion in the system. For this purpose, we consider incoherent pumping for $|g\rangle \rightarrow |x\rangle$ and $|x\rangle \rightarrow |u\rangle$ transition with pumping rate η_1 and η_2, respectively. The cavity has two V-polarized non-degenerate modes with frequencies ω_1 and ω_2. We consider transitions $|y\rangle \rightarrow |g\rangle$ and $|u\rangle \rightarrow |y\rangle$ are coupled with cavity modes with coupling constant g_1 and g_2. The biexciton state may decay to the ground state through one of the two exciton states by the emission of horizontally (H) or vertically (V) polarized photons [58].

4.2.1 Master equation for Incoherent Pumping

In the rotating frame with frequency ω_y, we express the Hamiltonian for the dot-cavity system as

$$\begin{aligned} H &= \hbar\delta_x\sigma_{xx} - \hbar(\Delta_{xx} - \delta_x)\sigma_{uu} \\ &\quad - \hbar\delta_1 a_1^\dagger a_1 - \hbar(\Delta_{xx} - \delta_x + \delta_2)a_2^\dagger a_2 \\ &\quad + \hbar g_1(\sigma_{yg}a_1 + \sigma_{gy}a_1^\dagger) + \hbar g_2(\sigma_{uy}a_2 + \sigma_{yu}a_2^\dagger), \end{aligned} \tag{4.1}$$

where $\delta_1 = \omega_y - \omega_1$, $\delta_2 = \omega_u - \omega_y - \omega_2$ are cavity detunings, and a_1, a_2 are field operators of the first and second mode, respectively. The notation $\sigma_{ij} = |i\rangle\langle j|$ refers to the projection operator for QD states. In the semiconductor QD-cavity system, the interaction of the electrons with the lattice modes of vibration, *i.e.*, the longitudinal acoustic phonons, plays an important role. This phonon interaction displays several new phenomena, including strong dephasing, off-resonant cavity feeding, and the emergence of new features in Mollow triplets [101–103]. To incorporate phonon interaction into the dynamics of the QD-cavity system, we have to include the following additional terms

$$H_{ph} = \hbar\sum_k \omega_k b_k^\dagger b_k + \sum_{i=x,y,u} \lambda_{ik}\sigma_{ii}(b_k + b_k^\dagger), \tag{4.2}$$

where λ_{ik} are exciton phonon coupling constants and $b_k(b_k^\dagger)$ are annihilation(creation) operators for k^{th} phonon mode of frequency ω_k. The second term in H_{ph} represents

the interaction between excitons with the phonon reservoir. The total Hamiltonian of the QD-cavity system, including exciton-phonon interaction, becomes

$$H_T = H + H_{ph}. \tag{4.3}$$

However, it should be borne in mind that including all orders of exciton phonon interaction in the master equation of the QD-cavity system has been a very challenging task. Although many perturbative approaches have been explored in the literature, often involving the truncation of higher-order phonon interaction terms [101, 208, 209]. The most successful master equation for the QD-cavity system utilizes the polaron transformation, which considers all orders of phonon interaction [101–103]. The Hamiltonian H_T is transformed into $H^{'}$ using polaron transformation $H' = e^{P} H_T\, e^{-P}$ where

$$P = \sum_{i=x,y,u} \frac{\lambda_{ik}}{\omega_k} \sigma_{ii} \left(b_k^{\dagger} - b_k \right).$$

The transformed Hamiltonian H' contains system, bath, and their interaction Hamiltonian as $H' = H_s + H_b + H_{sb}$, where

$$\begin{aligned} H_s &= \hbar\delta_x \sigma_{xx} - \hbar(\Delta_{xx} - \delta_x)\sigma_{uu} - \hbar\Delta_1 a_1^{\dagger} a_1 \\ &\quad - \hbar(\Delta_{xx} - \delta_x + \Delta_2) a_2^{\dagger} a_2 + \langle B \rangle X_g, \end{aligned} \tag{4.4}$$

$$H_b = \hbar \sum_k \omega_k b_k^{\dagger} b_k, \tag{4.5}$$

$$H_{sb} = \xi_g X_g + \xi_u X_u. \tag{4.6}$$

Here, we redefine the cavity detunings into effective detunings Δ_1 and Δ_2 after including the polaron shifts $\sum_k \lambda_{ik}^2/\omega_k$. The system operators are defined by

$$X_g = \hbar \left(g_1 \sigma_{yg} a_1 + g_2 \sigma_{uy} a_2 \right) + H.c. \tag{4.7}$$

$$X_u = i\hbar \left(g_1 \sigma_{yg} a_1 + g_2 \sigma_{uy} a_2 \right) + H.c., \tag{4.8}$$

and the phonon bath fluctuation operators are

$$\xi_g = \frac{1}{2} \left(B_+ + B_- - 2\langle B \rangle \right), \tag{4.9}$$

$$\xi_u = \frac{1}{2i} \left(B_+ - B_- \right), \tag{4.10}$$

where B_+, B_- are the phonon displacement operator. The phonon displacement operators are defined by

$$B_{\pm} = \exp\left[\pm \sum_k \frac{\lambda_k}{\omega_k} \left(b_k^{\dagger} - b_k \right) \right].$$

The phonon displacement operator averaged over all closely spaced phonon modes at a temperature T obeys the relation $\langle B_+ \rangle = \langle B_- \rangle = \langle B \rangle$ where

$$\langle B \rangle = \exp\left[-\frac{1}{2} \int_0^{\infty} d\omega \frac{J(\omega)}{\omega^2} \coth\left(\frac{\hbar\omega}{2K_b T} \right) \right]. \tag{4.11}$$

The phonon spectral density function $J(\omega)$ is given by $J(\omega) = \alpha_p \omega^3 \exp[-\omega^2/2\omega_b^2]$ [106], where the parameters α_p and ω_b are the electron-phonon coupling and cutoff

frequency, respectively. We have chosen model parameters $\alpha_p = 1.42 \times 10^{-3}/g_1^2$ and $\omega_b = 10g_1$, which gives us the value of $\langle B\rangle = 1.0$, 0.90, and 0.73 for $T = 0K$, $5K$, and $20K$, respectively [110, 111].

Now, applying second-order Born-Markov approximation, the master equation for reduced density matrix of a QD-cavity system ρ_s can be written as [101–103]

$$\begin{aligned}\dot{\rho_s} = &-\frac{i}{\hbar}[H_s, \rho_s] - \mathcal{L}_{ph}\rho_s - \frac{\kappa_1}{2}\mathcal{L}[a_1]\rho_s - \frac{\kappa_2}{2}\mathcal{L}[a_2]\rho_s \\ &- \sum_{i=x,y}\left(\frac{\gamma_1}{2}\mathcal{L}[\sigma_{gi}] + \frac{\gamma_2}{2}\mathcal{L}[\sigma_{iu}]\right)\rho_s - \sum_{i=x,y,u}\frac{\gamma_d}{2}\mathcal{L}[\sigma_{ii}]\rho_s \\ &- \left(\frac{\eta_1}{2}\mathcal{L}[\sigma_{xg}] + \frac{\eta_2}{2}\mathcal{L}[\sigma_{ux}]\right)\rho_s, \end{aligned} \tag{4.12}$$

where we phenomenologically incorporate the photon leakage from the cavity modes with rates κ_1, κ_2, and spontaneous decay of exciton and biexciton states with rates γ_1, γ_2. In addition, we also include the pure-dephasing process with rate γ_d in the master equation (4.12). This additional dephasing term incorporates the zero-phonon line (ZPL) broadening in the QD emission spectrum[108, 109]. The last term in the master equation (4.12) is responsible for the incoherent pumping process with pumping rates η_1 and η_2. In the master equation, $\mathcal{L}$ stands for Lindblad superoperator, defined as $\mathcal{L}[\mathcal{O}]\rho_s = \mathcal{O}^\dagger\mathcal{O}\rho_s - 2\mathcal{O}\rho_s\mathcal{O}^\dagger + \rho_s\mathcal{O}^\dagger\mathcal{O}$. The term $\mathcal{L}_{ph}\rho_s$ represents the effect of phonon bath on the system dynamics. The explicit form of $\mathcal{L}_{ph}\rho_s$ in terms of previously defined system operators is written as

$$\mathcal{L}_{ph}\rho_s = \frac{1}{\hbar^2}\int_0^\infty d\tau \sum_{j=g,u} G_j(\tau)[X_j(t), X_j(t,\tau)\rho_s(t)] + H.c., \tag{4.13}$$

where $X_j(t,\tau) = e^{-iH_s\tau/\hbar}X_j(t)e^{iH_s\tau/\hbar}$, with the polaron Green functions $G_g(\tau) = \langle B\rangle^2\{\cosh[\phi(\tau)] - 1\}$ and $G_u(\tau) = \langle B\rangle^2\sinh[\phi(\tau)]$. The phonon Green's functions depend on the phonon correlation function

$$\phi(\tau) = \int_0^\infty d\omega \frac{J(\omega)}{\omega^2}\left[\coth\left(\frac{\hbar\omega}{2K_bT}\right)\cos(\omega\tau) - i\sin(\omega\tau)\right], \tag{4.14}$$

where K_b and T are the Boltzmann constant and the temperature of the phonon bath, respectively. We integrate the master equation (4.12) numerically using Quantum Optics Toolbox [165].

4.2.2 Master equation for Coherent Pumping

In this subsection, we derive the master equation for the QD-cavity system by considering a coherent field for pumping. We consider a horizontally polarised coherent field having frequency ω_p to the $|g\rangle \leftrightarrow |x\rangle$ and $|x\rangle \leftrightarrow |u\rangle$ transition with Rabi frequency Ω_1 and Ω_2, respectively. The Hamiltonian of this system in a rotating frame with frequency ω_p can be written as

$$\begin{aligned}H = &\hbar\Delta_p\sigma_{xx} + \hbar(2\Delta_p - \delta_x - \Delta_{xx})\sigma_{uu} + \hbar(\Delta_p - \delta_x)\sigma_{yy} \\ &+ \hbar(\Delta_p - \delta_x - \Delta_1)a_1^\dagger a_1 + \hbar(\Delta_p - \Delta_{xx} - \Delta_2)a_2^\dagger a_2 \\ &+ \hbar\Omega_1(\sigma_{xg} + \sigma_{gx}) + \hbar\Omega_2(\sigma_{ux} + \sigma_{xu}) + \hbar g_1(\sigma_{yg}a_1 \\ &+ \sigma_{gy}a_1^\dagger) + \hbar g_2(\sigma_{uy}a_2 + \sigma_{yu}a_2^\dagger) + H_{ph}, \end{aligned} \tag{4.15}$$

where $\Delta_p = \omega_x - \omega_p$ and all others parameters are same as previous definitions. As mentioned earlier, we make the previously defined polaron transformation. After using polaron transformation, we get the system Hamiltonian and other operators as follows:

$$H_s = \hbar\Delta_p\sigma_{xx} + \hbar(2\Delta_p - \delta_x - \Delta_{xx})\sigma_{uu} + \hbar(\Delta_p - \delta_x)\sigma_{yy} + \hbar(\Delta_p - \delta_x - \Delta_1)a_1^\dagger a_1 + \hbar(\Delta_p - \Delta_{xx} - \Delta_2)a_2^\dagger a_2 + \langle B\rangle X_g, \tag{4.16}$$

$$X_g = \hbar\left(\Omega_1\sigma_{xg} + \Omega_2\sigma_{ux} + g_1\sigma_{yg}a_1 + g_2\sigma_{uy}a_2\right) + H.c \tag{4.17}$$

$$X_u = i\hbar\left(\Omega_1\sigma_{xg} + \Omega_2\sigma_{ux} + g_1\sigma_{yg}a_1 + g_2\sigma_{uy}a_2\right) + H.c. \tag{4.18}$$

We use the defined system operators in the master equation (4.12) for coherently pumped QD by neglecting the incoherent pumping terms present in the equation.

4.3 Two-mode lasing using incoherent pumping

We thoroughly investigate incoherently pumped QD by numerically solving the master equation (4.12), followed by computations of various QD populations and cavity field parameters under steady-state conditions. Our findings, presented in Fig. 4.2-4.5, correspond to a phonon bath temperature T=5K alongside other experimentally compatible parameters. The chosen biexciton binding energy is $\Delta_{xx} = 15g_1$, while the fine structure splitting of excitons is $\delta_x = -g_1$. By applying continuous incoherent pumping, we explore the feasibility of achieving population inversion in the biexciton state. Such an incoherent pumping scheme was successfully realized experimentally via continuous excitation of the wetting layer [210], widely implemented in single QD lasers.

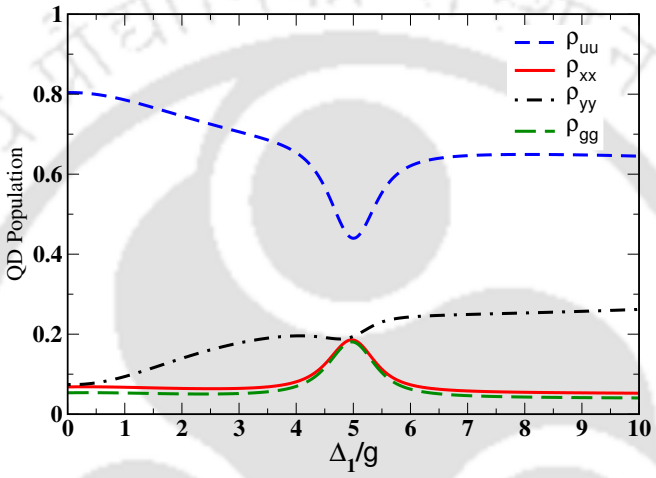

Figure 4.2: The steady state populations in QD states $|u\rangle$(blue short dash),$|x\rangle$(red solid),$|y\rangle$(black short dash dot), $|g\rangle$(green long dash) as a function of Δ_1 for phonon bath temperature T=5K. Other parameters are cavity leakage $\kappa_1 = \kappa_2 = 0.1g$, cavity field couplings $g_1 = g_2 = g$, spontaneous decay rates $\gamma_1 = \gamma_2 = 0.01g$, pure dephasing rate $\gamma_d = 0.01g$, biexciton binding energy $\Delta_{xx} = 15g$, hyperfine energy gap between excitons $\delta_x = -g$, detuning of second cavity mode $\Delta_2 = -5g$ and $\eta_1 = \eta_2 = 0.5g$. Among all the populations, the biexciton state (blue dashed line) has a higher population compared to the other populations because of the high second cavity mode detuning, which prevents $|u\rangle \rightarrow |y\rangle$ transition. But at two-photon resonance condition $\Delta_1 = 5g$, a part of the population goes to the ground state via the two-photon process and therefore reduces ρ_{uu} population and increases ρ_{gg} and ρ_{xx} population as they are driving via constant incoherent pumping.

In Fig. 4.2, we demonstrate the variation of steady state populations in various QD states with the first cavity mode detuning Δ_1. We observe that the population in the biexciton state $|u\rangle$ surpasses any other exciton states. This dominance in biexciton state population is due to the large detuning, $|\Delta_2| \gg g_2$, which prevents population transfer from $|u\rangle$ to $|y\rangle$. Thus, the system behavior is similar to the population inversion in the regular lasing action. Therefore, the population transfer from biexciton to the ground state may produce efficient two-photon lasing via the two-photon resonant transition. We notice from Fig. 4.2 that at two-photon resonance condition $\Delta_1 = -\Delta_2$, the population in $|u\rangle$ shows a dip while the population in $|g\rangle$ gets a peak due to maximum transfer of population from $|u\rangle$ to $|g\rangle$. Generally, the two-photon process is a weak nonlinear process; this can be enhanced by suppressing the single-photon process.

The single-photon transitions are minimized by maintaining a sizeable second mode detuning $|\Delta_2| \gg g_2$. Consequently, even at single photon resonance condition $\Delta_1 = 0$ for $|y\rangle \rightarrow |g\rangle$ transition, single photon emission remains insignificant due to minimal population in $|y\rangle$ state. Under this consideration, the probabilities of single-photon emission decrease significantly. The two-photon resonance condition $\Delta_1 + \Delta_2 = 0$ can be simplified as $\omega_u = \omega_1 + \omega_2$, therefore cavity induced decay of biexciton $|u\rangle$ to ground state $|g\rangle$ generates a pair of non degenerate photons of frequencies ω_1 and ω_2. Furthermore, the $|y\rangle$ state population increases monotonically with a local dip at two-photon resonance as Δ_1 increases. At the single-photon resonance condition, the population in $|y\rangle$ state readily transfers to the $|g\rangle$ state, which explains the lowest population in $|y\rangle$ state at $\Delta_1 = 0$. As Δ_1 increases, the transition $|y\rangle \rightarrow |g\rangle$ becomes off-resonant, resulting in an increasing population in $|y\rangle$ state. Fig. 4.2 also exhibit the identical variation of populations in $|x\rangle$ and $|g\rangle$ states.

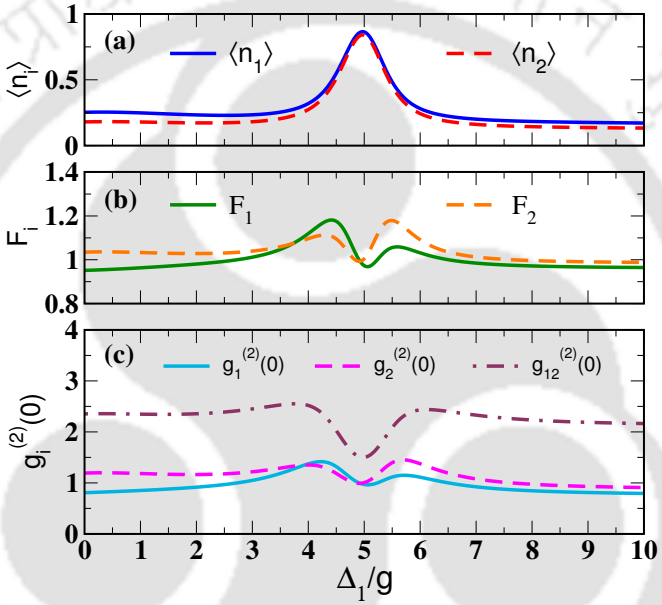

Figure 4.3: a) The average photon number of first and second mode $\langle n_1\rangle$(blue solid), $\langle n_2\rangle$(red dash), b) Fano factors F_1 (green solid), F_2 (orange dash), and c) Second order photon correlation function with zero time delay $g_1^{(2)}(0)$ (cyan solid), $g_2^{(2)}(0)$ (pink dash), $g_{12}^{(2)}(0)$(brown dash-dot) varying with first cavity mode detuning Δ_1 for temperature T=5K. All other parameters are the same as Fig.4.2. The average photon number peaks near the two-photon resonance condition, indicating the photon emission to both cavity modes. The Fano factor reaches its lowest value near two-photon resonance, indicating a coherent light generation. The second-order correlation function supports the previous observation by showing its minima near two-photon resonance. Thus, we can expect the nondegenerate two-photon laser in QD at two-photon resonance conditions.

The Fig. 4.3 depicts the statistics of the generated photons as a function of the first cavity mode detuning. In Fig. 4.3(a), we present the average photon number $\langle n_1\rangle = \langle a_1^\dagger a_1\rangle$ and $\langle n_2\rangle = \langle a_2^\dagger a_2\rangle$. Both modes exhibit identical average photon numbers, peaking at the two-photon resonance. The identical nature of the curves arises from photons being generated in a biexciton-exciton cascaded decay process. Under two-photon resonance, no individual photon emission occurs, but a photon pair is emitted simultaneously. Therefore, each photon goes to the corresponding cavity mode with an equal probability. The average number of photon peaks is consistent with the sudden

decay of the $|u\rangle$ population as shown in Fig. 4.2. The Fano factor of the cavity field is then subsequently analyzed by determining the ratio between the variance of the photon number and the average photon number for each cavity mode. In terms of the cavity mode operators, the Fano factor for the first and second cavity modes is given by:

$$F_1 = (\langle n_1^2\rangle - \langle n_1\rangle^2)/\langle n_1\rangle, \tag{4.19}$$
$$F_2 = (\langle n_2^2\rangle - \langle n_2\rangle^2)/\langle n_2\rangle. \tag{4.20}$$

Fig. 4.3(b) shows that both F_1 and F_2 have a dip near two-photon resonance. Otherwise, both have a constant value near unity. This minimum value of Fano factors indicates noise suppression in the cavity under two-photon resonance conditions. Next, we analyze the generated optical field with the help of the second-order correlation function. Following the definition of second-order photon correlation functions with zero time delay for the two-mode cavity [211], defined as

$$g_1^{(2)}(0) = \langle a_1^{\dagger 2} a_1^2\rangle/\langle a_1^\dagger a_1\rangle^2, \tag{4.21}$$
$$g_2^{(2)}(0) = \langle a_2^{\dagger 2} a_2^2\rangle/\langle a_2^\dagger a_2\rangle^2, \tag{4.22}$$
$$g_{12}^{(2)}(0) = \langle a_1^\dagger a_2^\dagger a_2 a_1\rangle/\langle a_1^\dagger a_1\rangle\langle a_2^\dagger a_2\rangle. \tag{4.23}$$

Fig. 4.3(c) shows that all the second-order correlations have a minimum value at the two-photon resonance condition. At two-photon resonance, $g_i^{(2)}(0)$ approaches unity, which implies that the generated field in each mode is nearly coherent. However, the cross-correlation $g_{12}^{(2)}(0)$ remains more than one, indicating a super-Poissonian nature.

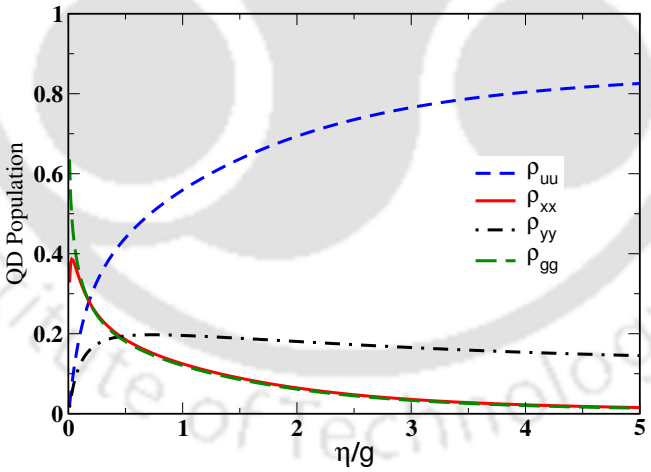

Figure 4.4: The steady-state populations in QD states $|u\rangle$(blue short dash), $|x\rangle$(red solid), $|y\rangle$(black short dash-dot), $|g\rangle$(green long dash) vs incoherent pumping rate η for phonon bath temperature T=5K. All other parameters are same as Fig. 4.2 except $\Delta_1 = 5g$ and $\eta_1 = \eta_2 = \eta$. We see that for no pumping, all the population in the $|g\rangle$ state, and then by increasing the incoherent pumping rate first $|x\rangle$ state population rapidly increases and $|u\rangle$, $|y\rangle$ slowly occupied. Later, the population goes from $|x\rangle \rightarrow |u\rangle$, increasing $|u\rangle$ state population and decreasing $|x\rangle$ population. The biexciton state population ρ_{uu} gets saturated for a very high pumping rate.

In Fig. 4.4, we demonstrate the variation of steady-state QD populations as a function of incoherent pumping rate. The population of $|u\rangle$ state increases with η and eventually saturates at a very high pumping rate. The exciton population variation in

the $|g\rangle$ and $|x\rangle$ states follow an identical trend. These exciton populations are higher for low pumping rates but become negligible as the pumping rate increases. Conversely, the $|y\rangle$ population remains nearly constant after achieving population inversion. It is evident that population inversion occurs for a low pumping rate, and it grows and saturates for higher pumping rates. In Fig. 4.5, we present the variation of previously

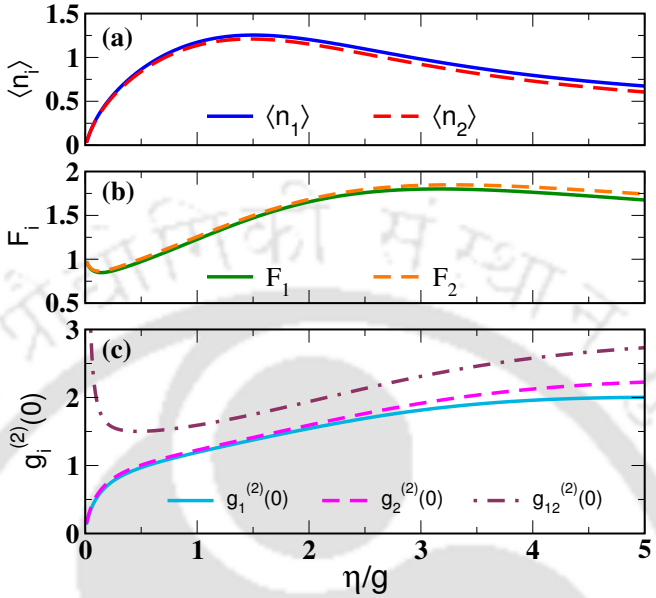

Figure 4.5: a) Average photon number for first and second mode $\langle n_1\rangle$(blue solid), $\langle n_2\rangle$(red dash), b)Fano factors F_1(green solid), F_2(orange dash), c) Second order correlations function with zero time delay $g_1^{(2)}(0)$(cyan solid), $g_2^{(2)}(0)$(pink dash), $g_{12}^{(2)}(0)$(brown dash-dot) as a function of η for temperature T=5K. All other parameters are same as Fig. 4.2 except $\Delta_1 = 5g$ and $\eta_1 = \eta_2 = \eta$. The average photon number in both cavity modes increases with the increasing incoherent pumping rate and achieves a maximum value, then reduced to a lower value due to single emitter's self-quenching effect. Fano factors have a value near unity and achieve a minimum at low pumping rates. Conversely, the Fano factor gradually increases to a very high value for high pumping rates, leading to unfavorable conditions for laser generation. The second-order correlation function $g_{12}^{(2)}(0)$ has a minimum around $\eta = 0.5g$ and other correlation function values near unity, indicating a good condition for the two-photon QD laser generation.

defined cavity parameters by changing the incoherent pumping rate. The average photon number in both cavity modes increases and acquires maximum on increasing pump rate and then decreases for further higher pumping rate, resulting from a single emitter self-quenching effect [212]. The Fano factor of the cavity modes is below one before inversion is achieved and surpasses one afterward. The second-order correlations for cavity modes $g_1^{(2)}(0)$ and $g_2^{(2)}(0)$ grow with incoherent pumping rate, approaching a value of two for high pumping rates, as depicted in Fig. 4.5(c). The generated field exhibit sub-Poissonian photon statistics ($g_i^{(2)}(0) < 1$) for low pumping rate and then become Poissonian ($g_i^{(2)}(0) = 1$) for moderate pumping rate $0.5g < \eta < 1.0g$. However, for higher pumping rates, the cavity field demonstrates thermal photon statistics ($g_i^{(2)}(0) = 2$). Henceforth, it indicates that with increasing incoherent pumping, photon emission becomes uncorrelated. The inter-modal correlation $g_{12}^{(2)}(0)$ exibits values greater than one. Further, for low pumping rate, $g_{12}^{(2)}(0)$ first decreases and attains a minimum value when stimulated emission becomes maximum, then again increases

with increasing pumping rate. This observation suggests that all the correlation gets diminished by increasing the pumping rate beyond a certain limit.

Next, we formulate the laser rate equation using quantum laser theory developed by Scully and Lamb [19, 213]. For that we simplify $\mathcal{L}_{ph}\rho_s$ term in master equation under off resonant condition $|\Delta_1| \gg g_1$ and $|\Delta_2| \gg g_2$ [214]. By considering appropriate approximation, we derived the analytical form of the master equation with various phonon-modified decay rates as detailed in Appendix A.

The two-photon laser rate equation is given by

$$\begin{aligned}\dot{P}_{n,m} = &-\alpha_{n,m}P_{n,m} + G^{11}_{n-1,m-1}P_{n-1,m-1} \\ &+ G^{10}_{n-1,m}P_{n-1,m} + G^{01}_{n,m-1}P_{n,m-1} \\ &+ A^{11}_{n+1,m+1}P_{n+1,m+1} + A^{10}_{n+1,m}P_{n+1,m} \\ &+ A^{01}_{n,m+1}P_{n,m+1} + \kappa_1(n+1)P_{n+1,m} \\ &- \kappa_1 n P_{n,m} + \kappa_2(m+1)P_{n,m+1} - \kappa_2 m P_{n,m},\end{aligned} \tag{4.24}$$

where

$$P_{n,m} = \sum_i \langle i,n,m|\rho_s|i,n,m\rangle, \tag{4.25}$$

$$\alpha_{n,m}P_{n,m} = \sum_i \alpha_{i,n,m}\langle i,n,m|\rho_s|i,n,m\rangle, \tag{4.26}$$

$$G^{\alpha\beta}_{n,m}P_{n,m} = \sum_i G^{\alpha\beta}_{i,n,m}\langle i,n,m|\rho_s|i,n,m\rangle, \tag{4.27}$$

$$A^{\alpha\beta}_{n,m}P_{n,m} = \sum_i A^{\alpha\beta}_{i,n,m}\langle i,n,m|\rho_s|i,n,m\rangle \tag{4.28}$$

with $i = \{g, x, y, u\}$ and $\alpha, \beta = 0, 1$.

It is worth noting that there could be some more terms in Eq.(4.24) corresponding to three-photon and four-photon emissions etc. However, their contributions remain negligible under two-photon resonance. In Eq.(4.24), the stimulated single-photon emission rates in the first mode, second mode, and two-photon emission rate when one photon is emitted in each mode are given by $\sum_{n,m} G^{10}_{n,m}P_{n,m}$, $\sum_{n,m} G^{(01)}_{n,m}P_{n,m}$ and $\sum_{n,m} G^{11}_{n,m}P_{n,m}$, respectively. Similarly, single-photon absorption from first mode, second mode, and two-photon absorption rates are given by $\sum_{n,m} A^{10}_{n,m}P_{n,m}$, $\sum_{n,m} A^{01}_{n,m}P_{n,m}$ and $\sum_{n,m} A^{11}_{n,m}P_{n,m}$. These rates are evaluated numerically. We define the net single photon emission rate in the first mode by taking the difference between single photon emission rate and single photon absorption rate $\sum_{n,m}(G^{10}_{n,m} - A^{10})P_{n,m}$, the net single photon emission rate in second mode as $\sum_{n,m}(G^{01}_{n,m} - A^{01}_{n,m})P_{n,m}$. Similarly, the net emission rate of two-photon when one photon is emitted in each mode is defined as $\sum_{n,m}(G^{11}_{n,m} - A^{11}_{n,m})P_{n,m}$.

We plot net single-photon emission rates in the first mode, second mode, and net two-photon emission rates in Fig. 4.6 at different temperatures. In Fig. 4.6(a), the stimulated two-photon emission rate dominates over single-photon emission rates in both modes and achieves maximum value for low pumping rate ($\eta \approx g$) at phonon bath temperature T=5K. However, on increasing incoherent pumps, the correlation in photon emission decreases. As a result, two-photon emission decreases, and the single-photon emission in each mode starts dominating. The single-photon emission rate of the second mode is higher than the first mode for a higher pumping rate. The

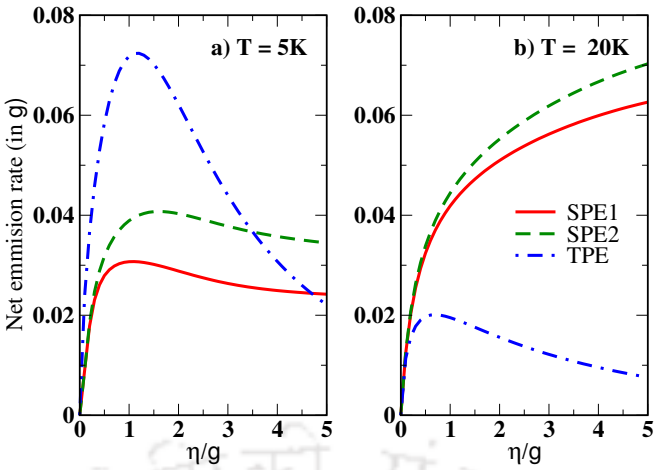

Figure 4.6: First mode single-photon emission rate(SPE1, red solid), Second mode single-photon emission rate(SPE2, green dash) and two-photon stimulated emission rate(TPE, blue dash dot) dependency on incoherent pumping rate using $\Delta_1 = 5g_1$, $\eta_1 = \eta_2 = \eta$ for a)T=5K and b) T=20K with all other parameters same as Fig. 4.2. In subplot (a) at low-temperature T = 5K, the two-photon emission dominates the single-photon emission for both modes. This is because the phonon contribution to the system is much less. In subplot (b) at higher temperature T = 20K, the system reacts oppositely as the single photon emission dominates over the two-photon correlated emission. The high-temperature scenario allows the light emission through the virtual phonon sideband to achieve single photon emission.

higher two-photon emission rate at a low pump indicates that the system acts like a two-photon gain medium. In Fig. 4.6(b), we plot net emission rates at higher phonon bath temperature T=20K. The correlated two-photon emission decreases significantly, and the independent single-photon emission rates in both modes increase. This effect occurs due to the phonon-mediated process at higher temperatures. The two-photon process becomes negligible at a higher temperature, and the single-photon process gets enhanced due to phonon-induced dephasing in the system. Comparing these two-photon and single-photon emissions, we conclude that the system shows higher two-photon gain for low pump ($\eta \approx g$) at low temperatures.

4.4 Two-mode two-photon lasing using coherent pumping

In this proposed scheme, a coherent laser field resonantly excites the transition from the ground state $|g\rangle$ to the exciton state $|x\rangle$. This resonance ensures that the biexciton to exciton transition should be highly detuned because of the large biexciton binding energy. In this scenario, a very efficient biexciton generation is possible with the phonon-assisted transitions [196]. A similar approach has been successfully demonstrated for the generation of biexciton states in QD with high-fidelity [197].

We numerically solve the master equation (4.12) by employing Eqs.4.16-4.18 to get the steady-state populations in different QD states under various cavity field parameters with coherent pumping. Fig. 4.7 illustrates how the population in different QD

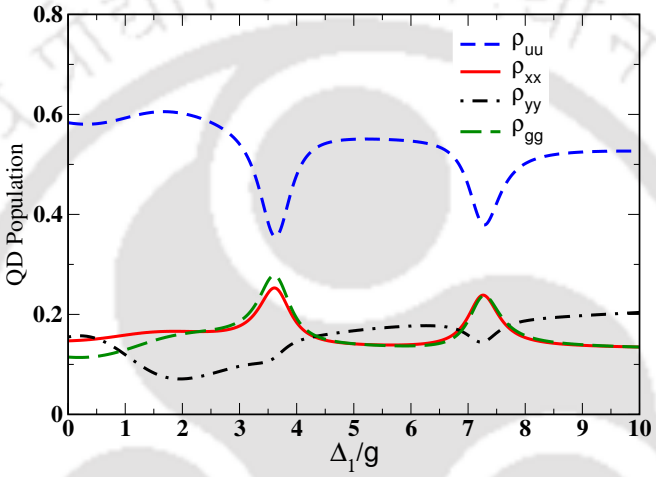

Figure 4.7: The steady-state populations in the various quantum dot energy states $|u\rangle$(blue short dash), $|x\rangle$(red solid), $|y\rangle$(black short dash-dot), $|g\rangle$(green long dash) plotted against first cavity mode detuning Δ_1 for phonon bath temperature T=5K. Other parameters are same as Fig. 4.2 except $\Delta_p = 0$ and $\Omega_1 = \Omega_2 = 2g$. For the coherent pumping case, the biexciton state population (blue dashed line) remains in high value compared to all other populations similar to the incoherent pumping case. However, now we see two different minima around the $\Delta_1 = 5g$, which can be explained by the dressed state picture of the QD for coherent pumping. The mentioned minimum indicates the two-photon emission is possible for two different detunings as the ρ_{uu} decreases and the ρ_{gg} increases.

states vary with detuning Δ_1 under coherent pumping. Remarkably, the biexciton state population consistently exceeds that of any other QD-state for typical values of system parameters, indicating population inversion in the system.

We observed that the biexciton state population has two distinct minima separated by $2\Omega_1$ when the two-photon resonance condition is satisfied. An explanation of this new feature is possible with the help of a dressed state picture. By applying a strong resonant coherent field between the $|g\rangle$ and $|x\rangle$, the dressed states $|\pm\rangle = \frac{1}{\sqrt{2}}(|x\rangle \pm |g\rangle)$ are formed with frequency separation $2\Omega_1$. Fig. 4.8 displays the equivalent dressed state picture of the system in the presence of strong coherent pumping. The population of the biexciton state $|u\rangle$ exhibits two notable dips, marking the transitions from the bare state $|u\rangle$ to the dressed states $|+\rangle$ and $|-\rangle$ via two-photon transitions in cavity modes. Consequently, the two-photon emission occurs at two different values of the first mode detuning $\Delta_1 = -\Delta_2 \pm \Omega_1$. The populations of $|g\rangle$ and $|x\rangle$ remain relatively

unchanged, reaching their maxima at these specific values of Δ_1 due to the population transfer from $|u\rangle \leftrightarrow |\pm\rangle$. Meanwhile, the population in state $|y\rangle$ remains small with the local minimum at two-photon resonances.

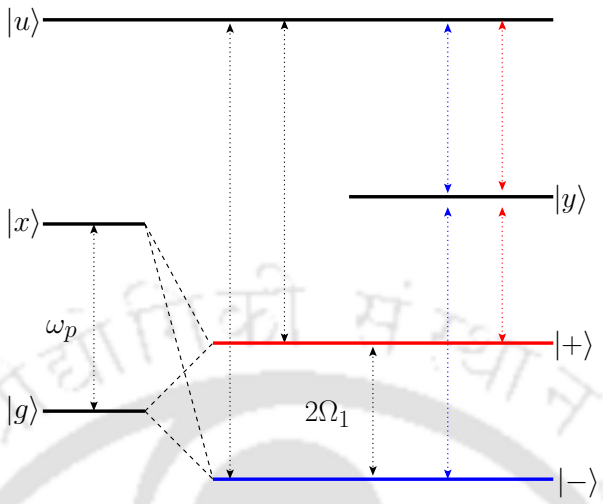

Figure 4.8: The strong field coupled with the $|g\rangle \leftrightarrow |x\rangle$ transition produces dressed states $|\pm\rangle$ with frequency separation $2\Omega_1$. These dressed states facilitate phonon-assisted pumping to the biexciton state, indicated by black dotted lines. Subsequently, two different values of Δ_1 can be obtained, satisfying the two-photon resonance condition, as illustrated by red and blue dotted lines.

The average photon numbers in the cavity modes have two prominent peaks with a separation of $2\Omega_1$ as shown in Fig. 4.9(a). These peaks arise from two nondegenerate photon emissions into the cavity modes via two-photon transition $|u\rangle \rightarrow |y\rangle \rightarrow |\pm\rangle$. We also notice that the two peaks in average photon number in each cavity mode are not identical. While their separation remains close to $2\Omega_1$, they are not symmetrically positioned around $\Delta_1 = -\Delta_2$. This asymmetry is attributed to the optical Stark shifts in the QD energy levels [215, 216], causing both peaks to shift slightly towards the higher frequency side. The Fano-factors for both cavity modes consistently hover around unity, reaching their minimum values when two-photon resonant conditions are satisfied at $\Delta_1 = -\Delta_2 \pm \Omega_1$. In Fig. 4.9(c), the second-order correlations for each cavity mode $g_i^{(2)}(0)$ have maintained values close to unity . Hence, the photons generated in each mode adhere to Poissonian statistics, signifying coherent field generation. Moreover, intermodal correlation, $g_{12}^{(2)}(0)$, exhibits values larger than two except under the circumstances that satisfy the two-photon resonance condition, where it attains a minimum value of less than two. Therefore, two-mode two-photon lasing becomes feasible within a single quantum dot upon satisfying the two-photon resonant condition.

In order to formulate the laser rate equation, it is essential to have the analytical expression of the master equation for coherent pumping. Appendix B provides a comprehensive overview of this master equation. We derive the laser rate equation (4.24) for coherently pumped QD using the method discussed in the preceding section. Recalling previously defined net emission rates, we plot it against first-mode detuning for two different temperatures in Fig. 4.10. From Fig. 4.10(a), we notice that the net stimulated single photon emission rate in the first and second modes show a positive peak when the single-photon transition $|y\rangle \rightarrow |\pm\rangle$ becomes resonant. These transi-

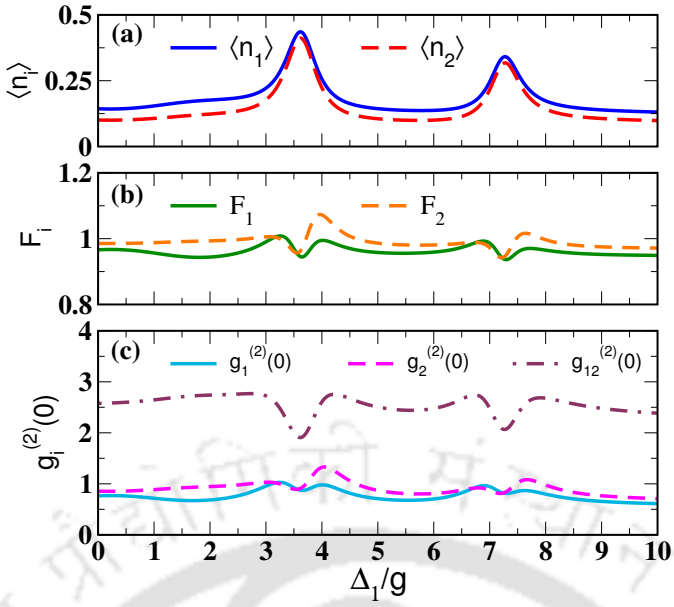

Figure 4.9: The variation of a) average photon number $\langle n_1 \rangle$(blue solid), $\langle n_2 \rangle$(red dash), b) Fano factors F_1(green solid), F_2(orange dash), and c) Second order correlation $g_1^{(2)}(0)$(cyan solid), $g_2^{(2)}(0)$(pink dash), $g_{12}^{(2)}(0)$(brown dash dot) with respect to Δ_1 at a phonon bath temperature T=5K. All other parameters are the same as Fig. 4.7. The new feature of the coherent pumping case is that all the cavity parameters show two-photon lasing at two different detuning values, which gives us more options for the chosen parameters. All other behaviors are almost the same as incoherent pumping.

tions decrease population in $|y\rangle$, thus resulting in population inversion between $|u\rangle$ and $|y\rangle$. Therefore, similar peaks are visible in net single-photon stimulated emission in the second mode. Conversely, the two-mode two-photon net emission rate displays negative dips around single-photon resonance, indicating significant two-mode two-photon absorption. Thus, no appreciable change occurs in the average photon number in cavity modes. However, this scenario shifts drastically around the two-photon resonance condition, where the two-mode two-photon net emission rate dominates over the single-photon emission rate. Under two-photon resonant condition $\Delta_1 \approx -\Delta_2 \pm \Omega_1$, the single-photon processes are highly detuned, and net single-photon stimulated emission in both modes become very small. In contrast the two-mode two-photon emission peaks becomes prominent.

Moreover, for $\Delta_1 \approx -\Delta_2 - \Omega_1$, single-photon net stimulated emission rates approach zero, thereby establishing more favorable conditions for two-mode two-photon lasing. In Fig. 4.10(b), we plot net stimulated emission rates for higher temperature T = 20K. This figure reveals a suppression of the two-mode two-photon emission, accompanied by an enhancement of the single-photon emission. This outcome is due to the domination of the phonon process at a higher temperature, which hinders correlated two-photon emission in two modes. In conclusion, these findings suggest that the two-mode, two-photon lasing for coherent pumping is possible at low temperatures.

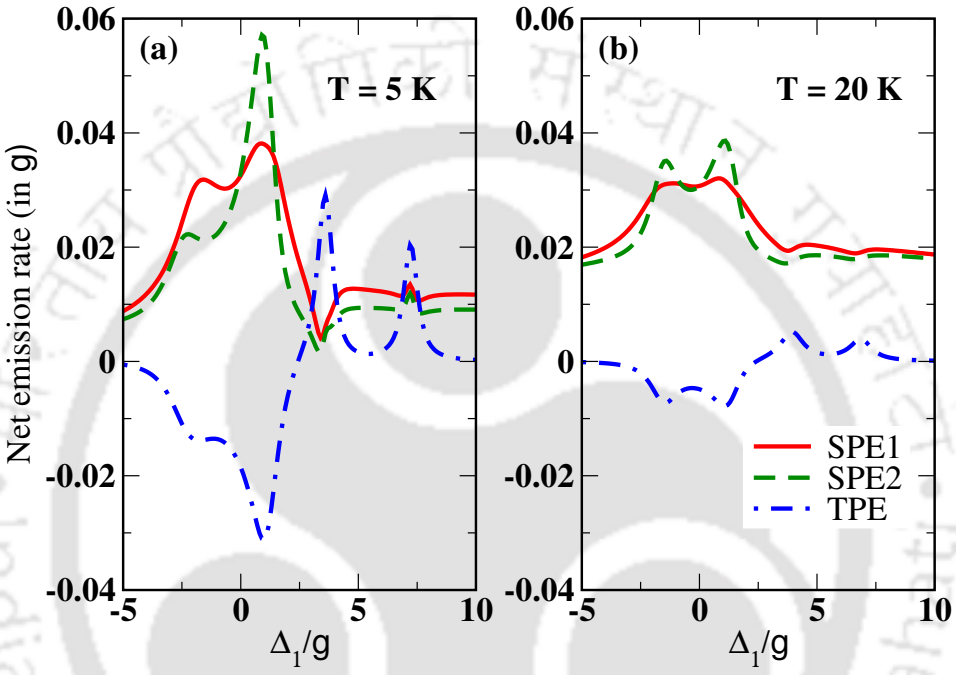

Figure 4.10: The figure illustrates the single-photon emission rate of the first (SPE1, red solid) and second mode (SPE2, green dash), as well as the two-mode two-photon stimulated emission rate (TPE, blue dash-dot) versus the first mode detuning Δ_1 by considering $\Omega_1 = \Omega_2 = 2g_1$, for a)T=5K and b) T=20K with all other parameters same as Fig. 4.7. From sub-figure (a), we understand that the single photon emission is dominated over two-photon emission near single photon resonance condition $\Delta_1 = 0$ oppositely, two-photon emission dominated near the two-photon resonance condition $\Delta_1 = -5g$. We notice that for $\Delta_1 = -\Delta_2 - \Omega_1$ the single photon emission becomes almost zero, but the two-photon emission is prominent, which is favorable for the two-photon laser generation. For higher temperatures, sub-figure (b) is not favorable for laser generation as single photon emission dominates due to the phonon-assisted process.

4.5 Generation of steady state two-mode entangled state

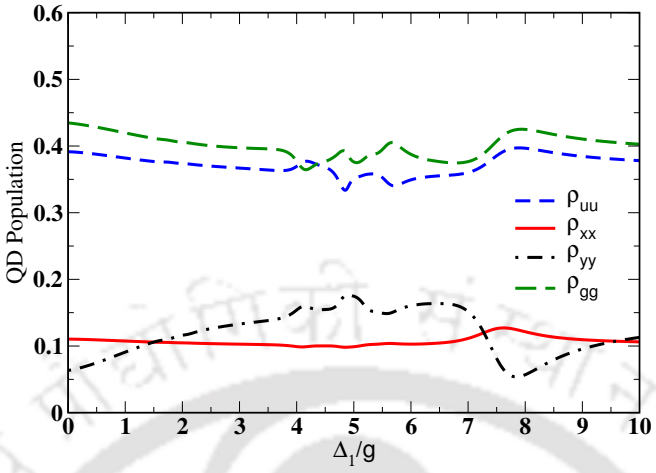

Figure 4.11: The two-photon resonantly pumped steady-state populations variation with Δ_1 in quantum dot energy states $|u\rangle$(blue short dash), $|x\rangle$(red solid), $|y\rangle$(black short dash-dot), $|g\rangle$(green long dash) for same parameters as Fig. 4.7 except $\Delta_p = 7g$. In the case of the two-photon pumping process, the biexciton state $|u\rangle$ and ground state $|g\rangle$ get populated equally without populating the intermediate state $|x\rangle$ because of the large detuning $\Delta_p = 7g$. The system also shows no population inversion, as the populations are almost similar. The intermediate states $|x\rangle$ and $|y\rangle$ remain less populated as the population mainly revolves around $|u\rangle$ and $|g\rangle$.

This section discusses the effect of two-photon coherent resonant pumping in $|g\rangle \rightarrow |x\rangle \rightarrow |u\rangle$ transition. We choose detuning of the exciton pump such that the two-photon resonant condition $\omega_u = 2\omega_p$, i.e., $\Delta_p = (\Delta_{xx} + \delta_x)/2$ is satisfied.

In Fig. 4.11, we present the steady-state populations of various energy states in a QD. The populations in ground state $|g\rangle$ and biexciton state $|u\rangle$ remain nearly equal and significantly larger than those in $|x\rangle$ and $|y\rangle$. Additionally, due to the spontaneous decay of the biexciton state, the population in the ground state $|g\rangle$ becomes slightly higher than that in the biexciton state $|u\rangle$. Therefore, there is no population inversion in the system. During the two-photon resonant pumping process, the simultaneous absorption of two pump photons results in $|g\rangle \leftrightarrow |u\rangle$ transition, leading to a low population in the exciton state $|x\rangle$. The biexciton state $|u\rangle$ decays to ground state $|g\rangle$ through cavity modes via a two-mode, two-photon resonant transition $|u\rangle \rightarrow |y\rangle \rightarrow |g\rangle$ when the two-photon resonance condition $\Delta_1 + \Delta_2 = 0$ is satisfied. The average number of photons in the cavity modes reaches a maximum at two-photon resonance conditions(shown in Fig. 4.12(a)). The Fano-factors demonstrate a value greater than one near the two-photon resonance, implying that the fields generated in both modes have higher noise than coherent states. All second-order correlations exhibit similar behavior as the previous case, except for minor oscillations.

Let us discuss the steady-state entanglement between the two non-degenerate cavity modes. We will use the Duan-Giedke-Cirac-Zoller (DGCZ) criterion [84, 217] to measure the continuous variable entanglement. This criterion necessitates defining two EPR-like variables for the two-mode cavity fields, such as

$$u = x_1 + x_2, v = p_1 - p_2, \tag{4.29}$$

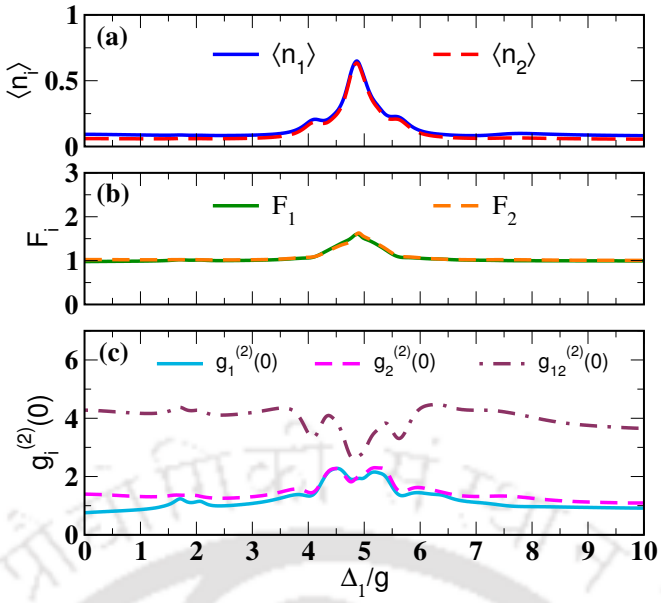

Figure 4.12: The graph displays the variation of a) average photon number $\langle n_1\rangle$(blue solid), $\langle n_2\rangle$(red dash) b) Fano factors F_1(green solid), F_2(orange dash) c) second order correlations $g_1^{(2)}(0)$(cyan solid), $g_2^{(2)}(0)$(pink dash), $g_{12}^{(2)}(0)$(brown dash-dot) as a function of Δ_1 for same parameters as Fig. 4.9 except $\Delta_p = 7g$.

where x_j, p_j for jth cavity mode are written in terms of the cavity operators

$$x_j = \frac{1}{\sqrt{2}}(a_j^\dagger e^{-i\phi_j} + a_j e^{i\phi_j}), \tag{4.30}$$

$$p_j = \frac{i}{\sqrt{2}}(a_j^\dagger e^{-i\phi_j} - a_j e^{i\phi_j}), j = \{1, 2\}. \tag{4.31}$$

According to the DGCZ criterion, two quantized modes of cavity radiation are entangled if the quantum fluctuations of the operators u and v satisfy the inequality

$$\Delta u^2 + \Delta v^2 = \langle (u - \langle u\rangle)^2 + (v - \langle v\rangle)^2\rangle < 2. \tag{4.32}$$

The left-hand side of the inequality is expressed in terms of experimentally measurable quantities as

$$\begin{aligned}\Delta u^2 + \Delta v^2 = 2(1 &+ \langle a_1^\dagger a_1\rangle + \langle a_2^\dagger a_2\rangle + \langle a_1^\dagger a_2^\dagger\rangle e^{-i(\phi_1+\phi_2)} \\ &+ \langle a_1 a_2\rangle e^{i(\phi_1+\phi_2)} - \langle a_1^\dagger\rangle\langle a_1\rangle - \langle a_2^\dagger\rangle\langle a_2\rangle \\ &- \langle a_1^\dagger\rangle\langle a_2^\dagger\rangle e^{-i(\phi_1+\phi_2)} - \langle a_1\rangle\langle a_2\rangle e^{i(\phi_1+\phi_2)}).\end{aligned} \tag{4.33}$$

The Fig. 4.13 depicts the sum of the variance of two EPR-like variables $\Delta u^2 + \Delta v^2$ with Δ_1 for different temperatures using typical values of system parameters. We use pump strength smaller than cavity mode coupling ($\Omega_1 = \Omega_2 = 0.5g$) in Fig. 4.13(a) and larger than cavity mode coupling ($\Omega_1 = \Omega_2 = 2.0g$) in Fig. 4.13(b). According to the DGCZ criterion, two cavity modes become entangled if $\Delta u^2 + \Delta v^2 < 2$, the critical value is shown by the black dotted line. It is clear that for two-photon pump strength smaller than cavity coupling ($\Omega_1 = \Omega_2 < g$) and at low temperature ($T < 10K$), two modes are entangled.

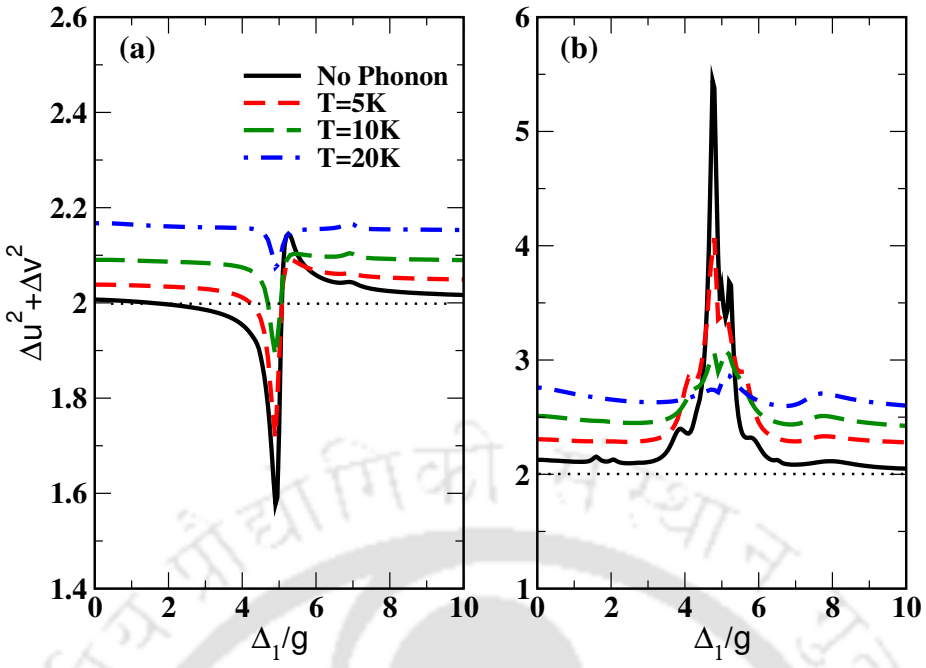

Figure 4.13: The total variance of an EPR-like variable pair plotted with first mode single photon detuning Δ_1 for different bath temperatures. The Black dotted line indicates the margin for entanglement phenomenon according to the DGCZ criterion. All the parameters are the same as Fig. 4.11 except $\phi_1 = \phi_2 = -0.5$ with coherent pumping Rabi frequencies a)$\Omega_1 = \Omega_2 = 0.5g$ and b)$\Omega_1 = \Omega_2 = 2g$. This figure concludes that the low pumping rate and low temperatures are optimal for two-mode continuous variable entanglement generation.

4.6 Conclusions

In conclusion, we have predicted the feasibility of two-mode two-photon lasing in a single quantum dot embedded in the two-mode microcavity system. We have considered the effect of exciton-phonon interaction using the polaron master equation formalism. The stimulated two-mode two-photon emission rate dominates at low pump strength and temperature $T = 5K$ under incoherently pumped QD. For a coherently pumped, one can achieve large two-mode two-photon stimulated emission with negligible single-photon stimulated emission, which provides better conditions for practical nondegenerate two-photon lasing in a single quantum dot. We have also predicted that the two-photon resonant pumping scheme could generate steady-state two-mode entangled states. The two-mode, two-photon laser scheme may have potential applications in scalable quantum photonic technology in quantum computation, quantum information, and large quantum networks. The two-mode continuous-variable entanglement scheme can offer an advantage in some situations in quantum information science.

Chapter 5

Conclusion and Future Plans

In recent times, semiconductor-integrated photonics have gained a lot of research interest for making reliable quantum photonic circuits required to make a quantum computer. These photonic circuits include optical elements, such as photon sources, quantum communication channels, beam splitters, quantum gates, etc. To fit all these elements into a chip, they have to be very tiny in dimension. Additionally, the power consumption of each optical component must be minimized to reduce the circuit's overall power requirement. This thesis addressed some of the above-mentioned optical elements in quantum dots, satisfying the tiny footprint and low power requirement criteria. In this thesis, we have addressed three problems in optical pulse propagation and quantum light generation. These problems are presented in the thesis according to their complexity order. We start with a two-level system, then move on to a four-level system, and finally consider a four-level system interacting with a two-mode cavity. The flow of the thesis is as follows: Chapter 2 discussed the optical pulse propagation in a QD medium, Chapter 3 presented the vector beam generation followed by light propagation, and Chapter 4 proposed a QD-cavity system for nondegenerate two-photon laser and two-mode entanglement. These schemes can have potential applications for building quantum communication channels and quantum light sources.

In Chapter 2, we have demonstrated self-induced transparency in an inhomogeneously broadened semiconductor quantum dots at ultracold temperatures. In this process, an optical pulse can propagate through the absorbing two-level medium at resonance conditions without changing any intensity or shape of the pulse. We considered a realistic model system of inhomogeneously broadened QD medium with phonon interaction due to the lattice vibration. We have considered all orders of phonon interaction in the calculation by applying polaron transformation and modified polaron master equation. We analyzed the additional phonon-induced pumping and decay rates and their low-temperature asymmetry. The pulse area theorem has been revisited as a function of the environmental temperatures. Observation suggests a slightly higher pulse area is required for stable pulse propagation at higher temperatures. The susceptibility of the medium is also presented to understand the SIT dynamics. The excited state population shows minimum values near the integer multiple of 2π, indirectly indicating the generated transparency in the medium and cross-verifying the earlier results. We observed that the SIT phenomena occurred in the QD medium with minimal absorption and distortion in pulse shape at $T = 5K$ temperature. Increasing propagation distance produces more pulse shape distortion and diminishes peak inten-

sity. We discussed the effect of QD spectral broadening and observed that the higher inhomogeneous broadening causes a lower time delay of the output pulse. We have also studied the effect of phonon bath parameters on the SIT dynamics. Increasing temperature and the phonon coupling strength destroy the QD coherence and hence distort the output pulse shape. Finally, we show the pulse breakup phenomena for a 4π input pulse in a QD medium.

In Chapter 3, we proposed a model for arbitrary vector beam generation in a thin disk-shaped semiconductor QD medium. The QD consists of a four-level diamond-like system with contributions from first- and third-order nonlinearity susceptibility. Therefore, we have applied one weak probe and two strong control OAM-carrying fields to the respective QD transition and generated a new field via the FWM process. This process transfers the control field OAM to the generated field. The medium absorbs the applied probe field due to first-order susceptibility. We have vectorially superposed the remaining applied probe field with the generated field having orthogonal polarisation to create a vector beam. We have presented how left-circular polarisation components get absorbed by the medium and the right-circular component's generation with transferred OAM. We have also compared these two components to find the proper propagation distance for fulfilling the condition for a lemon vector beam. Then, we generated three FP beams by changing the OAM of the right-circular polarisation component. Subsequently, we also generated three cylindrical vector beams by changing the relative phase. This generation technique is robust because we can generate arbitrary VB by playing with all the controlling parameters. We have also demonstrated the VB polarisation rotation technique of the generated VB by changing the relative control field phase. Finally, we have emphasized the effect of temperature on the VB generation. The result explained that the intensity of the VB diminishes with the increasing temperatures.

In Chapter 4, we have presented the generation of a nondegenerate two-photon laser and two-mode entanglement in a single QD embedded in a two-mode microcavity. The system consists of a QD with a four-level diamond-like level system with two vertically polarised biexciton-to-ground state transitions coupled to a two-mode microcavity. In this system, we have applied the incoherent/coherent pumping to the other two horizontally polarised transitions to produce population inversion. We have analyzed the scheme regarding various QD populations and cavity parameters. For incoherent pumping, the biexciton population transferred to the ground state with the rise in the average photon number at two-photon resonance conditions. The Fano factor and the second-order correlation also show a minimum value, indicating the laser generation. We have also discussed the dependence of the pumping rate on laser generation and found that a moderate pumping rate is most suitable for this scheme. We compared the single and two-photon emission rates at two different temperatures. We noticed that two-photon emission dominated at low temperatures, making it ideal for two-photon laser generation. The system shows similar behavior for coherent pumping except for the two lasing conditions. We have explained the origin of these two lasing conditions by introducing the dressed state analysis of the QD-light interaction. We have also found a more favorable condition for the two-photon process from the emission rate plot for coherent pumping. We have also analyzed two-mode continuous variable entanglement conditions for two-photon resonant pumping. The observation suggested that a lower temperature and pumping rate are suitable for such entanglement generation.

In the future, we will continue our research by completing previous unfinished work and some possible extensions of our current work. During my thesis, we started working on a research problem based on the storage and retrieval of an optical pulse in a QD medium. In this problem, we have considered a lambda-type three-level system by selecting the upper half of the four-level QD diamond system. Though we have some interesting results after proper calculations, the few nanoseconds lifetime of the exciton states makes this model ineffective as we want to store the optical pulse for a very long time. We are looking for a new level system in QD, considering the dark exciton states to implement this problem. We hope to solve this problem in the future. We also thought of one possible extension of the VB generation scheme. This scheme has much potential to create new and exciting physics because of third-order nonlinear susceptibility. Next, we will study the VB propagation in this QD medium. According to our predictions, we may see the self-focusing effect of the VB due to the nonlinearity. We will carry out this work shortly.

Appendix A

Simplified master equation for incoherent pumping

In this section, we derive the approximate analytical form of the complete master equation Eq.(4.12) to develop the laser rate equation. Therefore, Liouville's term corresponds to the phonon term $\mathcal{L}_{ph}\rho_s$ is expanded using commutator brackets. The exact expression of the total Hamiltonian leads to mathematical challenges to perform the similarity transformation *i.e.*, $X_j(t,\tau) = e^{-iH_s\tau/\hbar}X_j(t)e^{iH_s\tau/\hbar}$ for constructing the general master equation. To avoid such complications, we use the Hamiltonian H_s, which drops $\langle B\rangle X_g$ term, to perform the similarity transformation. This approximation is consistent since we are interested in the enhanced two-photon emission where the single-photon emission is almost negligible. Therefore, the cavity coupling constants chosen are significantly small compared to the single photon detunings ($g_1, g_2 \ll |\Delta_1|, |\Delta_2|$) and satisfy the two-photon resonance condition $\Delta_1 + \Delta_2 = 0$. Under such consideration, the interaction part of the system Hamiltonian can be neglected, resulting in

$$\begin{aligned} H_s = {} & \hbar\delta_x\sigma_{xx} - \hbar(\Delta_{xx} - \delta_x)\sigma_{uu} - \hbar\Delta_1 a_1^\dagger a_1 \\ & - \hbar(\Delta_{xx} - \delta_x + \Delta_2)a_2^\dagger a_2. \end{aligned} \tag{A.1}$$

Consequently, $\mathcal{L}_{ph}\rho_s$ is expanded with the help of simplified $X_j(t,\tau)$ operator and the master equation Eq.(4.12) takes the form

$$\begin{aligned} \dot{\rho_s} = {} & -\frac{i}{\hbar}[H_{eff}, \rho_s] - \sum_{i=x,y}\left(\frac{\gamma_1}{2}\mathcal{L}[\sigma_{gi}] + \frac{\gamma_2}{2}\mathcal{L}[\sigma_{iu}]\right)\rho_s \\ & - \frac{\kappa_1}{2}\mathcal{L}[a_1]\rho_s - \frac{\kappa_2}{2}\mathcal{L}[a_2]\rho_s - \sum_{i=x,y,u}\frac{\gamma_d}{2}\mathcal{L}[\sigma_{ii}]\rho_s \\ & - \left(\frac{\eta_1}{2}\mathcal{L}[\sigma_{xg}] + \frac{\eta_2}{2}\mathcal{L}[\sigma_{ux}]\right)\rho_s - \frac{1}{2}(\Gamma_2^+\mathcal{L}[\sigma_{yu}a_2^\dagger] \\ & + \Gamma_2^-\mathcal{L}[\sigma_{uy}a_2] + \Gamma_1^+\mathcal{L}[\sigma_{gy}a_1^\dagger] + \Gamma_1^-\mathcal{L}[\sigma_{yg}a_1]) \\ & - \frac{\Gamma_{ug}}{2}(\sigma_{ug}a_1a_2\rho_s - 2\sigma_{yg}a_1\rho_s a_2\sigma_{uy} + \rho_s\sigma_{ug}a_1a_2) \\ & - \frac{\Gamma_{gu}}{2}(\sigma_{gu}a_1^\dagger a_2^\dagger\rho_s - 2\sigma_{yu}a_2^\dagger\rho_s a_1^\dagger\sigma_{gy} + \rho_s\sigma_{gu}a_1^\dagger a_2^\dagger) \end{aligned} \tag{A.2}$$

where the effective Hamiltonian

$$H_{eff} = H_s + \hbar(\delta_2^+ \sigma_{uu} a_2 a_2^\dagger + \delta_2^- \sigma_{yy} a_2^\dagger a_2 + \delta_1^+ \sigma_{yy} a_1 a_1^\dagger + \delta_1^- \sigma_{gg} a_1^\dagger a_1) + \hbar\Omega_{12}(\sigma_{ug} a_1 a_2 + \sigma_{gu} a_1^\dagger a_2^\dagger), \tag{A.3}$$

and various additional detunings, effective coupling, phonon-induced rates

$$\begin{aligned}
\delta_i^\pm &= g_i^2 \langle B \rangle^2 Im \left[\int_0^\infty d\tau (e^{\phi(\tau)} - 1) e^{\pm i\Delta_i \tau} \right] \\
\Gamma_i^\pm &= 2 g_i^2 \langle B \rangle^2 Re \left[\int_0^\infty d\tau (e^{\phi(\tau)} - 1) e^{\pm i\Delta_i \tau} \right] \\
\Omega_{12} &= -\frac{i}{2} g_1 g_2 \langle B \rangle^2 [\alpha_1 - \alpha_2^*] \\
\Gamma_{ug} &= g_1 g_2 \langle B \rangle^2 [\alpha_1 + \alpha_2^*] \\
\Gamma_{gu} &= g_1 g_2 \langle B \rangle^2 [\alpha_1^* + \alpha_2] \\
\alpha_1 &= \int_0^\infty d\tau (e^{-\phi(\tau)} - 1) e^{-i\Delta_1 \tau} \\
\alpha_2 &= \int_0^\infty d\tau (e^{-\phi(\tau)} - 1) e^{i\Delta_2 \tau}.
\end{aligned} \tag{A.4}$$

Appendix B

Simplified master equation for coherent pumping

In the case of coherent pumping, we do a similar treatment described in Appendix A resulting in an effective master equation,

$$\begin{aligned}
\dot{\rho_s} = &-\frac{i}{\hbar}[H_{eff}, \rho_s] - \sum_{i=x,y}\left(\frac{\gamma_1}{2}\mathcal{L}[\sigma_{gi}] + \frac{\gamma_2}{2}\mathcal{L}[\sigma_{iu}]\right)\rho_s \\
&- \frac{\kappa_1}{2}\mathcal{L}[a_1]\rho_s - \frac{\kappa_2}{2}\mathcal{L}[a_2]\rho_s - \sum_{i=x,y,u}\frac{\gamma_d}{2}\mathcal{L}[\sigma_{ii}]\rho_s \\
&- \frac{1}{2}(\Gamma_2^+\mathcal{L}[\sigma_{yu}a_2^\dagger] + \Gamma_2^-\mathcal{L}[\sigma_{uy}a_2] \\
&+ \Gamma_1^+\mathcal{L}[\sigma_{gy}a_1^\dagger] + \Gamma_1^-\mathcal{L}[\sigma_{yg}a_1]) \\
&- \frac{\Gamma_{ug}}{2}(\sigma_{ug}a_1a_2\rho_s - 2\sigma_{yg}a_1\rho_s a_2\sigma_{uy} + \rho_s\sigma_{ug}a_1a_2) \\
&- \frac{\Gamma_{gu}}{2}(\sigma_{gu}a_1^\dagger a_2^\dagger\rho_s - 2\sigma_{yu}a_2^\dagger\rho_s a_1^\dagger\sigma_{gy} + \rho_s\sigma_{gu}a_1^\dagger a_2^\dagger) \\
&- \frac{1}{2}(\Gamma_2^{p+}\mathcal{L}[\sigma_{xu}] + \Gamma_2^{p-}\mathcal{L}[\sigma_{ux}] + \Gamma_1^{p+}\mathcal{L}[\sigma_{gx}] + \Gamma_1^{p-}\mathcal{L}[\sigma_{xg}]) \\
&- \frac{\Gamma_{ug}^p}{2}(\sigma_{ug}\rho_s - 2\sigma_{xg}\rho_s\sigma_{ux} + \rho_s\sigma_{ug}) \\
&- \frac{\Gamma_{gu}^p}{2}(\sigma_{gu}\rho_s - 2\sigma_{xu}\rho_s\sigma_{gx} + \rho_s\sigma_{gu})
\end{aligned} \tag{B.1}$$

where the effective Hamiltonian with coherent pumping

$$\begin{aligned}
H_{eff} = &H_s + \hbar(\delta_2^{p+}\sigma_{uu} + (\delta_2^{p-} + \delta_1^{p+})\sigma_{xx} + \delta_1^{p-}\sigma_{gg} \\
&+ \delta_2^+\sigma_{uu}a_2a_2^\dagger + \delta_2^-\sigma_{yy}a_2^\dagger a_2 + \delta_1^+\sigma_{yy}a_1a_1^\dagger \\
&+ \delta_1^-\sigma_{gg}a_1^\dagger a_1) + \hbar\Omega_{12}(\sigma_{ug}a_1a_2 + \sigma_{gu}a_1^\dagger a_2^\dagger) \\
&+ \hbar\Omega^p(\sigma_{ug} + \sigma_{gu}),
\end{aligned} \tag{B.2}$$

and new symbols are defined as

$$
\begin{aligned}
\delta_2^{p\pm} &= \Omega_2^2\langle B\rangle^2 Im\left[\int_0^\infty d\tau(e^{\phi(\tau)}-1)e^{\pm i\Delta_p^{'}\tau}\right]\\
\delta_1^{p\pm} &= \Omega_1^2\langle B\rangle^2 Im\left[\int_0^\infty d\tau(e^{\phi(\tau)}-1)e^{\pm i\Delta_p\tau}\right]\\
\Gamma_2^{p\pm} &= 2\Omega_2^2\langle B\rangle^2 Re\left[\int_0^\infty d\tau(e^{\phi(\tau)}-1)e^{\pm i\Delta_p^{'}\tau}\right]\\
\Gamma_1^{p\pm} &= 2\Omega_1^2\langle B\rangle^2 Re\left[\int_0^\infty d\tau(e^{\phi(\tau)}-1)e^{\pm i\Delta_p\tau}\right]\\
\Omega^p &= -\frac{i}{2}\omega_1\omega_2\langle B\rangle^2\left[\beta_1-\beta_2^*\right]\\
\Gamma_{ug}^p &= \Omega_1\Omega_2\langle B\rangle^2\left[\beta_1+\beta_2^*\right]\\
\Gamma_{gu}^p &= \Omega_1\Omega_2\langle B\rangle^2\left[\beta_1^*+\beta_2\right]\\
\beta_1 &= \int_0^\infty d\tau(e^{-\phi(\tau)}-1)e^{-i\Delta_p\tau}\\
\beta_2 &= \int_0^\infty d\tau(e^{-\phi(\tau)}-1)e^{i\Delta_p^{'}\tau},\ \Delta_p^{'}=\omega_u-\omega_x-\omega_p.
\end{aligned}
\tag{B.3}
$$

Bibliography

[1] J. O'Connor and E. Robertson, "Light through the ages: ancient greece to maxwell", Internet Archive Wayback Machine **1**, 6 (2002).

[2] A. M. Smith et al., *Ptolemy's theory of visual perception: an english translation of the optics*, Vol. 82 (American Philosophical Society, 1996).

[3] J. Kepler, "Astronomiae pars optica [the optical part of astronomy]", Francofurti: Claudium Marnium (1996).

[4] J. A. Vollgraff, "Snellius' notes on the reflection and refraction of rays", Osiris **1**, 718 (1936).

[5] C. Huygens, *Traité de la lumière* (Chez Pierre vander Aa, marchand libraire, A Leide, 1960).

[6] I. Newton, *Opticks, or, a treatise of the reflections, refractions, inflections & colours of light* (Courier Corporation, 1952).

[7] T. Young, "I. the bakerian lecture. experiments and calculations relative to physical optics", Philosophical Transactions of the Royal Society of London **94**, 1 (1804).

[8] M. Born and E. Wolf, *Principles of optics: electromagnetic theory of propagation, interference and diffraction of light* (Elsevier, 2013).

[9] F. A. Jenkins and H. E. White, "Fundamentals of optics", Indian Journal of Physics **25**, 265 (1957).

[10] J. D. Jackson, *Classical electrodynamics* (John Wiley & Sons, 2021).

[11] M. Planck, *The theory of heat radiation* (Blakiston, 1914).

[12] A. Einstein, "Über einen die erzeugung und verwandlung des lichtes betreffenden heuristischen gesichtspunkt", Annalen der Physik **322**, 132 (1905).

[13] W. E. Lamb and R. C. Retherford, "Fine structure of the hydrogen atom by a microwave method", Phys. Rev. **72**, 241 (1947).

[14] V. F. Weisskopf and E. P. Wigner, "Calculation of the natural brightness of spectral lines on the basis of dirac's theory", Z. Phys. **63**, 54 (1930).

[15] R. H. Brown and R. Twiss, "Lxxiv. a new type of interferometer for use in radio astronomy", The London, Edinburgh, and Dublin Philosophical Magazine and Journal of Science **45**, 663 (1954).

[16] R. H. Brown and R. Q. Twiss, "Correlation between photons in two coherent beams of light", Nature **177**, 27 (1956).

[17] A. L. Schawlow and C. H. Townes, "Infrared and optical masers", Phys. Rev. **112**, 1940 (1958).

[18] T. H. Maiman, "Stimulated optical radiation in ruby", Nature **187**, 493 (1960).

[19] M. O. Scully and W. E. Lamb, "Quantum theory of an optical maser. I. general theory", Phys. Rev. **159**, 208 (1967).

[20] S. L. McCall and E. L. Hahn, "Self-induced transparency by pulsed coherent light", Phys. Rev. Lett. **18**, 908 (1967).

[21] S. L. McCall and E. L. Hahn, "Self-induced transparency", Phys. Rev. **183**, 457 (1969).

[22] S. E. Harris, J. E. Field, and A. Imamo ğlu, "Nonlinear optical processes using electromagnetically induced transparency", Phys. Rev. Lett. **64**, 1107 (1990).

[23] E. Arimondo and G. Orriols, "Nonabsorbing atomic coherences by coherent two-photon transitions in a three-level optical pumping", Nuovo Cimento Lettere **17**, 333 (1976).

[24] S. E. Harris, "Lasers without inversion: interference of lifetime-broadened resonances", Phys. Rev. Lett. **62**, 1033 (1989).

[25] A. Kasapi, M. Jain, G. Y. Yin, and S. E. Harris, "Electromagnetically induced transparency: propagation dynamics", Phys. Rev. Lett. **74**, 2447 (1995).

[26] D. F. Phillips, A. Fleischhauer, A. Mair, R. L. Walsworth, and M. D. Lukin, "Storage of light in atomic vapor", Phys. Rev. Lett. **86**, 783 (2001).

[27] P. A. Franken, A. E. Hill, C. W. Peters, and G. Weinreich, "Generation of optical harmonics", Phys. Rev. Lett. **7**, 118 (1961).

[28] S. A. Akhmanov, A. Kovrigin, A. Piskarskas, V. Fadeev, and R. Khokhlov, "Observation of parametric amplification in the optical range", Jetp Lett **2**, 191 (1965).

[29] D. C. Burnham and D. L. Weinberg, "Observation of simultaneity in parametric production of optical photon pairs", Phys. Rev. Lett. **25**, 84 (1970).

[30] P. Verkerk, M. Pinard, and G. Grynberg, "Backward saturation in four-wave mixing in neon: case of parallel pump polarizations", Physical Review A **34**, 4008 (1986).

[31] R. H. Stolen and C. Lin, "Self-phase-modulation in silica optical fibers", Phys. Rev. A **17**, 1448 (1978).

[32] E. Cumberbatch, "Self-focusing in non-linear optics", IMA Journal of Applied Mathematics **6**, 250 (1970).

[33] D. J. Griffiths, *Introduction to electrodynamics* (Cambridge University Press, 2023).

[34] Johnn.27, *Electromagnetic fields and electromagnetic wave boundaries*, Physics Stack Exchange, URL:https://physics.stackexchange.com/q/519950 (2019).

[35] M. O. Scully and M. S. Zubairy, *Quantum optics* (Cambridge university press, 1997).

[36] C. C. Gerry and P. L. Knight, *Introductory quantum optics* (Cambridge university press, 2023).

[37] L. De Broglie, "Recherches sur la théorie des quanta", PhD thesis (Migration-université en cours d'affectation, 1924).

[38] N. Bohr, "I. on the constitution of atoms and molecules", The London, Edinburgh, and Dublin Philosophical Magazine and Journal of Science **26**, 1 (1913).

[39] A. Sommerfeld, *Atombau und spektrallinien*, Vol. 1 (F. Vieweg & sohn akt.-ges., 1924).

[40] W. Heisenberg, "Über den anschaulichen inhalt der quantentheoretischen kinematik und mechanik", Zeitschrift für Physik **43**, 172 (1927).

[41] E. Schrödinger, "An undulatory theory of the mechanics of atoms and molecules", Phys. Rev. **28**, 1049 (1926).

[42] P. A. M. Dirac, "The quantum theory of the electron", Proceedings of the Royal Society of London. Series A, Containing Papers of a Mathematical and Physical Character **117**, 610 (1928).

[43] M. Born, "Statistical interpretation of quantum mechanics", Science **122**, 675 (1955).

[44] M. Born, W. Heisenberg, and P. Jordan, "Zur quantenmechanik. II.", Zeitschrift für Physik **35**, 557 (1926).

[45] J. R. Rydberg, "Xxxiv. on the structure of the line-spectra of the chemical elements", The London, Edinburgh, and Dublin philosophical magazine and journal of science **29**, 331 (1890).

[46] B. H. Bransden and C. J. Joachain, *Physics of atoms and molecules* (Pearson Education India, 2003).

[47] N. Zettili, *Quantum mechanics: concepts and applications* (John Wiley & Sons, 2009).

[48] G. G. Hall and J. E. Lennard-Jones, "The molecular orbital theory of chemical valency. vi. properties of equivalent orbitals", Proceedings of the Royal Society of London. Series A. Mathematical and Physical Sciences **202**, 336 (1950).

[49] E. G. Barbagiovanni, D. J. Lockwood, P. J. Simpson, and L. V. Goncharova, "Quantum confinement in si and ge nanostructures: theory and experiment", Applied Physics Reviews **1**, 011302 (2014).

[50] M. R. P. I. Jayawardhana and K. A. I. L. Wijewardena Gamalath, "Electronic structures of cdse quantum dots embedded in znse", World Scientific News **86**, 205 (2017).

[51] F. P. García de Arquer, D. V. Talapin, V. I. Klimov, Y. Arakawa, M. Bayer, and E. H. Sargent, "Semiconductor quantum dots: technological progress and future challenges", Science **373**, eaaz8541 (2021).

[52] B. J. Riel, "An introduction to self-assembled quantum dots", American Journal of Physics **76**, 750 (2008).

[53] M. Liu, N. Yazdani, M. Yarema, M. Jansen, V. Wood, and E. H. Sargent, "Colloidal quantum dot electronics", Nature Electronics **4**, 548 (2021).

[54] S. J. Angus, A. J. Ferguson, A. S. Dzurak, and R. G. Clark, "Gate-defined quantum dots in intrinsic silicon", Nano Letters **7**, 2051 (2007).

[55] Z. M. Wang, *Self-assembled quantum dots*, Vol. 1 (Springer Science & Business Media, 2007).

[56] K. Y. K. Yamaguchi, K. Y. K. Yujobo, and T. K. T. Kaizu, "Stranski-krastanov growth of inas quantum dots with narrow size distribution", Japanese journal of applied physics **39**, L1245 (2000).

[57] S. F. C. da Silva, G. Undeutsch, B. Lehner, S. Manna, T. M. Krieger, M. Reindl, C. Schimpf, R. Trotta, and A. Rastelli, "Gaas quantum dots grown by droplet etching epitaxy as quantum light sources", Applied Physics Letters **119** (2021).

[58] P. Lodahl, S. Mahmoodian, and S. Stobbe, "Interfacing single photons and single quantum dots with photonic nanostructures", Rev. Mod. Phys. **87**, 347 (2015).

[59] G. D. Mahan, *Many-particle physics* (Springer Science & Business Media, 2013).

[60] C. Kittel and P. McEuen, *Introduction to solid state physics* (John Wiley & Sons, 2018).

[61] J. Bardeen and W. Shockley, "Deformation potentials and mobilities in non-polar crystals", Phys. Rev. **80**, 72 (1950).

[62] C. Herring and E. Vogt, "Transport and deformation-potential theory for many-valley semiconductors with anisotropic scattering", Phys. Rev. **101**, 944 (1956).

[63] G. L. Bir and G. E. Pikus, "Symmetry and strain-induced effects in semiconductors", (No Title) (1974).

[64] A. Nazir and D. P. S. McCutcheon, "Modelling exciton–phonon interactions in optically driven quantum dots", Journal of Physics: Condensed Matter **28**, 103002 (2016).

[65] P. Kaer, T. R. Nielsen, P. Lodahl, A.-P. Jauho, and J. Mørk, "Microscopic theory of phonon-induced effects on semiconductor quantum dot decay dynamics in cavity qed", Phys. Rev. B **86**, 085302 (2012).

[66] I. I. Rabi, "Space quantization in a gyrating magnetic field", Physical Review **51**, 652 (1937).

[67] P. Meystre and M. Sargent, *Elements of quantum optics* (Springer Science & Business Media, 2007).

[68] C. Cohen-Tannoudji, *Atoms in electromagnetic fields*, Vol. 1 (World scientific, 1994).

[69] Y.-R. Shen, *Principles of nonlinear optics* (Wiley-Interscience, New York, USA, 1984).

[70] L. Allen and J. H. Eberly, *Optical resonance and two-level atoms*, Vol. 28 (Courier Corporation, 1987).

[71] R. W. Boyd, A. L. Gaeta, and E. Giese, "Nonlinear optics", in *Springer handbook of atomic, molecular, and optical physics* (Springer, 2008), pp. 1097–1110.

[72] R. Carman, R. Chiao, and P. Kelley, "Observation of degenerate stimulated four-photon interaction and four-wave parametric amplification", Physical Review Letters **17**, 1281 (1966).

[73] R. Stolen, "Phase-matched-stimulated four-photon mixing in silica-fiber waveguides", IEEE Journal of Quantum Electronics **11**, 100 (1975).

[74] F. A. de Oliveira, C. B. de Araújo, and J. R. R. Leite, "Four-wave mixing in strongly driven four-level systems", Physical Review A **38**, 5688 (1988).

[75] N. Bloembergen, "Conservation laws in nonlinear optics", JOSA **70**, 1429 (1980).

[76] P. W. Milonni and J. H. Eberly, *Laser physics* (John Wiley & Sons, Inc., 1986).

[77] Ruchi, P. Senthilkumaran, and S. K. Pal, "Phase singularities to polarization singularities", International Journal of Optics **2020**, 2812803 (2020).

[78] L. Allen, M. W. Beijersbergen, R. Spreeuw, and J. Woerdman, "Orbital angular momentum of light and the transformation of laguerre-gaussian laser modes", Physical review A **45**, 8185 (1992).

[79] A. M. Yao and M. J. Padgett, "Orbital angular momentum: origins, behavior and applications", Advances in optics and photonics **3**, 161 (2011).

[80] A. M. Beckley, T. G. Brown, and M. A. Alonso, "Full poincaré beams", Optics express **18**, 10777 (2010).

[81] Q. Zhan, "Cylindrical vector beams: from mathematical concepts to applications", Advances in Optics and Photonics **1**, 1 (2009).

[82] E. T. Jaynes and F. W. Cummings, "Comparison of quantum and semiclassical radiation theories with application to the beam maser", Proceedings of the IEEE **51**, 89 (1963).

[83] A. Einstein, B. Podolsky, and N. Rosen, "Einsteinpodolskyrosen", Phys. Rev. **47**, 777 (1935).

[84] L.-M. Duan, G. Giedke, J. I. Cirac, and P. Zoller, "Inseparability criterion for continuous variable systems", Phys. Rev. Lett. **84**, 2722 (2000).

[85] R. E. Slusher and H. M. Gibbs, "Self-induced transparency in atomic rubidium", Phys. Rev. A **5**, 1634 (1972).

[86] J. GL LAMB, "Analytical descriptions of ultrashort optical pulse propagation in a resonant medium", Reviews of Modern Physics **43**, 99 (1971).

[87] J. Eilbeck, J. Gibbon, P. Caudrey, and R. Bullough, "Solitons in nonlinear optics. i. a more accurate description of the 2π pulse in self-induced transparency", Journal of Physics A: Mathematical, Nuclear and General **6**, 1337 (1973).

[88] S. W. Koch, A. Knorr, R. Binder, and M. Lindberg, "Microscopic theory of rabi flopping, photon echo, and resonant pulse propagation in semiconductors", physica status solidi (b) **173**, 177 (1992).

[89] H. Giessen, A. Knorr, S. Haas, S. W. Koch, S. Linden, J. Kuhl, M. Hetterich, M. Grün, and C. Klingshirn, "Self-induced transmission on a free exciton resonance in a semiconductor", Phys. Rev. Lett. **81**, 4260 (1998).

[90] A. Schülzgen, R. Binder, M. E. Donovan, M. Lindberg, K. Wundke, H. M. Gibbs, G. Khitrova, and N. Peyghambarian, "Direct observation of excitonic rabi oscillations in semiconductors", Phys. Rev. Lett. **82**, 2346 (1999).

[91] G. Panzarini, U. Hohenester, and E. Molinari, "Self-induced transparency in semiconductor quantum dots", Physical Review B **65**, 165322 (2002).

[92] P. Borri, W. Langbein, S. Schneider, U. Woggon, R. L. Sellin, D. Ouyang, and D. Bimberg, "Ultralong dephasing time in ingaas quantum dots", Phys. Rev. Lett. **87**, 157401 (2001).

[93] Z. Chen, Y. Zhou, and J.-T. Shen, "Exact dissipation model for arbitrary photonic fock state transport in waveguide qed systems", Opt. Lett. **42**, 887 (2017).

[94] Z. Chen, Y. Zhou, and J.-T. Shen, "Entanglement-preserving approach for reservoir-induced photonic dissipation in waveguide qed systems", Phys. Rev. A **98**, 053830 (2018).

[95] Q. Xu, D. Yao, X. Liu, Q. Zhou, and G. Xiong, "Adiabatic self-induced transparency in gan/aln inhomogeneously broadened quantum-dot ensemble", Optics & Laser Technology **45**, 768 (2013).

[96] X. Xu, Z. Zhen, S. Jin, and J. Ren, "Study of ultrafast rabi flopping in colloidal quantum dots at room temperature", Communications Physics **4**, 222 (2021).

[97] S. Schneider, P. Borri, W. Langbein, U. Woggon, J. Förstner, A. Knorr, R. L. Sellin, D. Ouyang, and D. Bimberg, "Self-induced transparency in ingaas quantum-dot waveguides", Applied Physics Letters **83**, 3668 (2003).

[98] A. Mandilara, Z. Ivić, D. Čevizović, and Ž. Pržulj, "Self-induced transparency of the optical phonons", Chaos, Solitons & Fractals **105**, 14 (2017).

[99] R. M. Arkhipov, M. V. Arkhipov, I. Babushkin, and N. N. Rosanov, "Self-induced transparency mode locking, and area theorem", Opt. Lett. **41**, 737 (2016).

[100] M. V. Arkhipov, A. A. Shimko, N. N. Rosanov, I. Babushkin, and R. M. Arkhipov, "Self-induced-transparency mode locking in a ti:sapphire laser with an intracavity rubidium cell", Phys. Rev. A **101**, 013803 (2020).

[101] D. P. S. McCutcheon and A. Nazir, "Quantum dot rabi rotations beyond the weak exciton–phonon coupling regime", New Journal of Physics **12**, 113042 (2010).

[102] C. Roy and S. Hughes, "Influence of electron–acoustic-phonon scattering on intensity power broadening in a coherently driven quantum-dot–cavity system", Phys. Rev. X **1**, 021009 (2011).

[103] C. Roy and S. Hughes, "Polaron master equation theory of the quantum-dot mollow triplet in a semiconductor cavity-qed system", Phys. Rev. B **85**, 115309 (2012).

[104] A. Bhardwaj, A. Hreibi, W. W. Yu, C. Liu, J. Heo, J.-L. Auguste, J.-M. Blondy, and F. Gérôme, "Optical fibers doped by semiconductor quantum dots: avenue for new fiber laser sources", in 2012 14th international conference on transparent optical networks (icton) (2012), pp. 1–5.

[105] D. A. Vajner, L. Rickert, T. Gao, K. Kaymazlar, and T. Heindel, "Quantum communication using semiconductor quantum dots", Advanced Quantum Technologies **5**, 2100116 (2022).

[106] A. Nazir, "Photon statistics from a resonantly driven quantum dot", Phys. Rev. B **78**, 153309 (2008).

[107] G. S. Agarwal, *Quantum optics* (Cambridge University Press, 2012).

[108] G. Ortner, D. R. Yakovlev, M. Bayer, S. Rudin, T. L. Reinecke, S. Fafard, Z. Wasilewski, and A. Forchel, "Temperature dependence of the zero-phonon linewidth in InAs/GaAs quantum dots", Phys. Rev. B **70**, 201301 (2004).

[109] S. Rudin, T. L. Reinecke, and M. Bayer, "Temperature dependence of optical linewidth in single inas quantum dots", Phys. Rev. B **74**, 161305 (2006).

[110] J. H. Quilter, A. J. Brash, F. Liu, M. Glässl, A. M. Barth, V. M. Axt, A. J. Ramsay, M. S. Skolnick, and A. M. Fox, "Phonon-assisted population inversion of a single InGaAs/GaAs quantum dot by pulsed laser excitation", Phys. Rev. Lett. **114**, 137401 (2015).

[111] R. Manson, K. Roy-Choudhury, and S. Hughes, "Polaron master equation theory of pulse-driven phonon-assisted population inversion and single-photon emission from quantum-dot excitons", Phys. Rev. B **93**, 155423 (2016).

[112] R. W. Boyd, "Chapter 3 - quantum-mechanical theory of the nonlinear optical susceptibility", in *Nonlinear optics (third edition)*, edited by R. W. Boyd, Third Edition (Academic Press, Burlington, 2008), pp. 135–206.

[113] A. Rahman and J. H. Eberly, "Theory of shape-preserving short pulses in inhomogeneously broadened three-level media", Phys. Rev. A **58**, R805 (1998).

[114] E. J. Galvez, S. Khadka, W. H. Schubert, and S. Nomoto, "Poincaré-beam patterns produced by nonseparable superpositions of laguerre–gauss and polarization modes of light", Appl. Opt. **51**, 2925 (2012).

[115] M. S. Soskin, V. N. Gorshkov, M. V. Vasnetsov, J. T. Malos, and N. R. Heckenberg, "Topological charge and angular momentum of light beams carrying optical vortices", Phys. Rev. A **56**, 4064 (1997).

[116] K. S. Youngworth and T. G. Brown, "Focusing of high numerical aperture cylindrical-vector beams", Opt. Express **7**, 77 (2000).

[117] Q. Zhan and J. R. Leger, "Focus shaping using cylindrical vector beams", Opt. Express **10**, 324 (2002).

[118] R. Dorn, S. Quabis, and G. Leuchs, "Sharper focus for a radially polarized light beam", Phys. Rev. Lett. **91**, 233901 (2003).

[119] M. Michihata, T. Hayashi, and Y. Takaya, "Measurement of axial and transverse trapping stiffness of optical tweezers in air using a radially polarized beam", Applied Optics **48**, 6143 (2009).

[120] Y. Kozawa and S. Sato, "Optical trapping of micrometer-sized dielectric particles by cylindrical vector beams", Optics Express **18**, 10828 (2010).

[121] B. J. Roxworthy and K. C. Toussaint, "Optical trapping with π-phase cylindrical vector beams", New Journal of Physics **12**, 073012 (2010).

[122] Y. Kozawa, D. Matsunaga, and S. Sato, "Superresolution imaging via superoscillation focusing of a radially polarized beam", Optica **5**, 86 (2018).

[123] P. Török and P. R. T. Munro, "The use of gauss-laguerre vector beams in sted microscopy", Optics Express **12**, 3605 (2004).

[124] J. Liu, S.-M. Li, L. Zhu, A.-D. Wang, S. Chen, C. Klitis, C. Du, Q. Mo, M. Sorel, S.-Y. Yu, X.-L. Cai, and J. Wang, "Direct fiber vector eigenmode multiplexing transmission seeded by integrated optical vortex emitters", Light: Science & Applications **7**, 17148 (2018).

[125] A. E. Willner, "Vector-mode multiplexing brings an additional approach for capacity growth in optical fibers", Light: Science & Applications **7**, 18002 (2018).

[126] D. P. Biss and T. G. Brown, "Polarization-vortex-driven second-harmonic generation", Optics Letters **28**, 923 (2003).

[127] G. Bautista, M. J. Huttunen, J. Mäkitalo, J. M. Kontio, J. Simonen, and M. Kauranen, "Second-harmonic generation imaging of metal nano-objects with cylindrical vector beams", Nano Letters **12**, 3207 (2012).

[128] G. Bautista, M. J. Huttunen, J. M. Kontio, J. Simonen, and M. Kauranen, "Third- and second-harmonic generation microscopy of individual metal nanocones using cylindrical vector beams", Optics Express **21**, 21918 (2013).

[129] W. Cheng, J. W. Haus, and Q. Zhan, "Propagation of vector vortex beams through a turbulent atmosphere", Optics Express **17**, 17829 (2009).

[130] Y. Gu, O. Korotkova, and G. Gbur, "Scintillation of nonuniformly polarized beams in atmospheric turbulence", Optics Letters **34**, 2261 (2009).

[131] M. A. Cox, C. Rosales-Guzmán, M. P. J. Lavery, D. J. Versfeld, and A. Forbes, "On the resilience of scalar and vector vortex modes in turbulence", Optics Express **24**, 18105 (2016).

[132] C. Wei, D. Wu, C. Liang, F. Wang, and Y. Cai, "Experimental verification of significant reduction of turbulence-induced scintillation in a full poincaré beam", Optics Express **23**, 24331 (2015).

[133] G. Milione, T. A. Nguyen, J. Leach, D. A. Nolan, and R. R. Alfano, "Using the nonseparability of vector beams to encode information for optical communication", Optics Letters **40**, 4887 (2015).

[134] V. D'Ambrosio, G. Carvacho, F. Graffitti, C. Vitelli, B. Piccirillo, L. Marrucci, and F. Sciarrino, "Entangled vector vortex beams", Phys. Rev. A **94**, 030304(R) (2016).

[135] D. Chen, S.-H. Zhao, L. Shi, and Y. Liu, "Measurement-device-independent quantum key distribution with pairs of vector vortex beams", Phys. Rev. A **93**, 032320 (2016).

[136] A. Sit, F. Bouchard, R. Fickler, J. Gagnon-Bischoff, H. Larocque, K. Heshami, D. Elser, C. Peuntinger, K. Günthner, B. Heim, C. Marquardt, G. Leuchs, R. W. Boyd, and E. Karimi, "High-dimensional intracity quantum cryptography with structured photons", Optica **4**, 1006 (2017).

[137] C. Maurer, A. Jesacher, S. Fürhapter, S. Bernet, and M. Ritsch-Marte, "Tailoring of arbitrary optical vector beams", New Journal of Physics **9**, 78 (2007).

[138] R. Kalita, M. Gaffar, and B. R. Boruah, "The generation of arbitrary vector beams using a division of a wavefront-based setup", Journal of Optics **18**, 075604 (2016).

[139] D. J. Armstrong, M. C. Phillips, and A. V. Smith, "Generation of radially polarized beams with an image-rotating resonator", Applied Optics **42**, 3550 (2003).

[140] S. C. Tidwell, G. H. Kim, and W. D. Kimura, "Efficient radially polarized laser beam generation with a double interferometer", Applied Optics **32**, 5222 (1993).

[141] T. Wang, S. Fu, S. Zhang, C. Gao, and F. He, "A sagnac-like interferometer for the generation of vector beams", Applied Physics B **122**, 231 (2016).

[142] S. Fu, C. Gao, Y. Shi, K. Dai, L. Zhong, and S. Zhang, "Generating polarization vortices by using helical beams and a twyman green interferometer", Optics Letters **40**, 1775 (2015).

[143] J. Xin, C. Gao, C. Li, and Z. Wang, "Generation of polarization vortices with a wollaston prism and an interferometric arrangement", Applied Optics **51**, 7094 (2012).

[144] M. Sakamoto, Y. Nakamoto, K. Kawai, K. Noda, T. Sasaki, N. Kawatsuki, and H. Ono, "Polarization grating fabricated by recording a vector hologram between two orthogonally polarized vector vortex beams", Journal of the Optical Society of America B **34**, 263 (2017).

[145] N. K. Viswanathan and V. V. G. Inavalli, "Generation of optical vector beams using a two-mode fiber", Optics Letters **34**, 1189 (2009).

[146] S. A. Schulz, T. Machula, E. Karimi, and R. W. Boyd, "Integrated multi vector vortex beam generator", Optics Express **21**, 16130 (2013).

[147] C. Rosales-Guzmán, N. Bhebhe, and A. Forbes, "Simultaneous generation of multiple vector beams on a single slm", Optics Express **25**, 25697 (2017).

[148] L. Gong, Y. Ren, W. Liu, M. Wang, M. Zhong, Z. Wang, and Y. Li, "Generation of cylindrically polarized vector vortex beams with digital micromirror device", Journal of Applied Physics **116**, 183105 (2014).

[149] M. Vergara and C. Iemmi, "Generalized q-plates and alternative kinds of vector and vortex beams", Phys. Rev. A **100**, 053812 (2019).

[150] C.-W. Qiu and Y. Yang, "Vortex generation reaches a new plateau", Science **357**, 645 (2017).

[151] Y. Toda, A. Moriya, K. Yamane, R. Morita, K. Shigematsu, and Y. Awaji, "Single orbital angular mode emission from externally feed-backed vertical cavity surface emitting laser", Applied Physics Letters **111**, 101102 (2017).

[152] X. Cai, J. Wang, M. J. Strain, B. Johnson-Morris, J. Zhu, M. Sorel, J. L. O'Brien, M. G. Thompson, and S. Yu, "Integrated compact optical vortex beam emitters", Science **338**, 363 (2012).

[153] P. Miao, Z. Zhang, J. Sun, W. Walasik, S. Longhi, N. M. Litchinitser, and L. Feng, "Orbital angular momentum microlaser", Science **353**, 464 (2016).

[154] J. Wang, "Metasurfaces enabling structured light manipulation: advances and perspectives [invited]", Chinese Optics Letters **16**, 050006 (2018).

[155] Y.-Z. Sun, R. Bachelot, S. Blaize, Z.-Y. Li, and W. Ding, "Vector beam generation via micrometer-scale photonic integrated circuits and plasmonic nanoantennae", Journal of the Optical Society of America B **33**, 360 (2016).

[156] P. Chen, L.-L. Ma, W. Duan, J. Chen, S.-J. Ge, Z.-H. Zhu, M.-J. Tang, R. Xu, W. Gao, T. Li, W. Hu, and Y.-Q. Lu, "Digitalizing self-assembled chiral superstructures for optical vortex processing", Advanced Materials **30**, 1705865 (2018).

[157] F. Gindele, K. Hild, W. Langbein, and U. Woggon, "Phonon interaction of single excitons and biexcitons", Phys. Rev. B **60**, R2157 (1999).

[158] S. Hughes, P. Yao, F. Milde, A. Knorr, D. Dalacu, K. Mnaymneh, V. Sazonova, P. J. Poole, G. C. Aers, J. Lapointe, R. Cheriton, and R. L. Williams, "Influence of electron-acoustic phonon scattering on off-resonant cavity feeding within a strongly coupled quantum-dot cavity system", Phys. Rev. B **83**, 165313 (2011).

[159] C. Roy and S. Hughes, "Phonon-dressed mollow triplet in the regime of cavity quantum electrodynamics: excitation-induced dephasing and nonperturbative cavity feeding effects", Phys. Rev. Lett. **106**, 247403 (2011).

[160] P. S. Hsu, G. R. Welch, J. R. Gord, and A. K. Patnaik, "Propagation dynamics of controlled cross-talk via interplay between $\chi^{(1)}$ and $\chi^{(3)}$ processes", Phys. Rev. A **83**, 053819 (2011).

[161] Rahmatullah, M. Abbas, Ziauddin, and S. Qamar, "Spatially structured transparency and transfer of optical vortices via four-wave mixing in a quantum-dot nanostructure", Phys. Rev. A **101**, 023821 (2020).

[162] T. Sugaya, O. Numakami, R. Oshima, S. Furue, H. Komaki, T. Amano, K. Matsubara, Y. Okano, and S. Niki, "Ultra-high stacks of InGaAs/GaAs quantum dots for high efficiency solar cells", Energy & Environmental Science **5**, 6233 (2012).

[163] J. D. Plumhof, R. Trotta, A. Rastelli, and O. G. Schmidt, "Experimental methods of post-growth tuning of the excitonic fine structure splitting in semiconductor quantum dots", Nanoscale Research Letters **7**, 336 (2012).

[164] M. Gong, W. Zhang, G.-C. Guo, and L. He, "Exciton polarization, fine-structure splitting, and the asymmetry of quantum dots under uniaxial stress", Phys. Rev. Lett. **106**, 227401 (2011).

[165] S. M. Tan, "A computational toolbox for quantum and atomic optics", J. Opt. B: Quantum Semiclass. Opt. **1**, 424 (1999).

[166] M. C. Stowe, A. Pe'er, and J. Ye, "Control of four-level quantum coherence via discrete spectral shaping of an optical frequency comb", Phys. Rev. Lett. **100**, 203001 (2008).

[167] N. S. Mallick and T. N. Dey, "Four-wave mixing-based orbital angular momentum translation", Journal of the Optical Society of America B **37**, 1857 (2020).

[168] M. Lax and W. H. Louisell, "Quantum noise. xii. density-operator treatment of field and population fluctuations", Phys. Rev. **185**, 568 (1969).

[169] D. Meschede, H. Walther, and G. Müller, "One-atom maser", Phys. Rev. Lett. **54**, 551 (1985).

[170] F. Dubin, C. Russo, H. G. Barros, A. Stute, C. Becher, P. O. Schmidt, and R. Blatt, "Quantum to classical transition in a single-ion laser", Nature Physics **6**, 350 (2010).

[171] J. McKeever, A. Boca, A. D. Boozer, J. R. Buck, and H. J. Kimble, "Experimental realization of a one-atom laser in the regime of strong coupling", Nature **425**, 268 (2003).

[172] O. Astafiev, K. Inomata, A. O. Niskanen, T. Yamamoto, Y. A. Pashkin, Y. Nakamura, and J. S. Tsai, "Single artificial-atom lasing", Nature **449**, 588 (2007).

[173] D. A. Rodrigues, J. Imbers, and A. D. Armour, "Quantum dynamics of a resonator driven by a superconducting single-electron transistor: a solid-state analogue of the micromaser", Phys. Rev. Lett. **98**, 067204 (2007).

[174] N. Lambert, F. Nori, and C. Flindt, "Bistable photon emission from a solid-state single-atom laser", Phys. Rev. Lett. **115**, 216803 (2015).

[175] Y.-Y. Liu, J. Stehlik, C. Eichler, X. Mi, T. R. Hartke, M. J. Gullans, J. M. Taylor, and J. R. Petta, "Threshold dynamics of a semiconductor single atom maser", Phys. Rev. Lett. **119**, 097702 (2017).

[176] M. Nomura, N. Kumagai, S. Iwamoto, Y. Ota, and Y. Arakawa, "Laser oscillation in a strongly coupled single-quantum-dot–nanocavity system", Nature Physics **6**, 279 (2010).

[177] J. L. O'Brien, A. Furusawa, and J. Vučković, "Photonic quantum technologies", Nature Photonics **3**, 687 (2009).

[178] T. D. Ladd, F. Jelezko, R. Laflamme, Y. Nakamura, C. Monroe, and J. L. O'Brien, "Quantum computers", Nature **464**, 45 (2010).

[179] O. Benson, "Assembly of hybrid photonic architectures from nanophotonic constituents", Nature **480**, 193 (2011).

[180] K. Hennessy, A. Badolato, M. Winger, D. Gerace, M. Atatüre, S. Gulde, S. Fält, E. L. Hu, and A. Imamoğlu, "Quantum nature of a strongly coupled single quantum dot–cavity system", Nature **445**, 896 (2007).

[181] K. Hennessy, A. Badolato, P. Petroff, and E. Hu, "Positioning photonic crystal cavities to single inas quantum dots", Photonics and Nanostructures - Fundamentals and Applications **2**, 65 (2004).

[182] L. Sapienza, M. Davanço, A. Badolato, and K. Srinivasan, "Nanoscale optical positioning of single quantum dots for bright and pure single-photon emission", Nature Communications **6**, 7833 (2015).

[183] S. M. Thon, M. T. Rakher, H. Kim, J. Gudat, W. T. M. Irvine, P. M. Petroff, and D. Bouwmeester, "Strong coupling through optical positioning of a quantum dot in a photonic crystal cavity", Applied Physics Letters **94**, 111115 (2009).

[184] M. Mantovani, A. D. Armour, W. Belzig, and G. Rastelli, "Dynamical multistability in a quantum-dot laser", Phys. Rev. B **99**, 045442 (2019).

[185] O. Benson and Y. Yamamoto, "Master-equation model of a single-quantum-dot microsphere laser", Phys. Rev. A **59**, 4756 (1999).

[186] S. Strauf and F. Jahnke, "Single quantum dot nanolaser", Laser & Photonics Reviews **5**, 607 (2011).

[187] C. Gies, M. Florian, P. Gartner, and F. Jahnke, "The single quantum dot-laser: lasing and strong coupling in the high-excitation regime", Opt. Express **19**, 14370 (2011).

[188] G. Rastelli and M. Governale, "Single atom laser in normal-superconductor quantum dots", Phys. Rev. B **100**, 085435 (2019).

[189] M. J. Gullans, Y.-Y. Liu, J. Stehlik, J. R. Petta, and J. M. Taylor, "Phonon-assisted gain in a semiconductor double quantum dot maser", Phys. Rev. Lett. **114**, 196802 (2015).

[190] M. Calic, P. Gallo, M. Felici, K. A. Atlasov, B. Dwir, A. Rudra, G. Biasiol, L. Sorba, G. Tarel, V. Savona, and E. Kapon, "Phonon-mediated coupling of InGaAs/GaAs quantum-dot excitons to photonic crystal cavities", Phys. Rev. Lett. **106**, 227402 (2011).

[191] M. Winger, T. Volz, G. Tarel, S. Portolan, A. Badolato, K. J. Hennessy, E. L. Hu, A. Beveratos, J. Finley, V. Savona, and A. Imamoglu, "Explanation of photon correlations in the far-off-resonance optical emission from a quantum-dot–cavity system", Phys. Rev. Lett. **103**, 207403 (2009).

[192] M. Florian, P. Gartner, C. Gies, and F. Jahnke, "Phonon-mediated off-resonant coupling effects in semiconductor quantum-dot lasers", New Journal of Physics **15**, 035019 (2013).

[193] S. Unsleber, D. P. S. McCutcheon, M. Dambach, M. Lermer, N. Gregersen, S. Höfling, J. Mørk, C. Schneider, and M. Kamp, "Two-photon interference from a quantum dot microcavity: persistent pure dephasing and suppression of time jitter", Phys. Rev. B **91**, 075413 (2015).

[194] A. Reigue, J. Iles-Smith, F. Lux, L. Monniello, M. Bernard, F. Margaillan, A. Lemaitre, A. Martinez, D. P. S. McCutcheon, J. Mørk, R. Hostein, and V. Voliotis, "Probing electron-phonon interaction through two-photon interference in resonantly driven semiconductor quantum dots", Phys. Rev. Lett. **118**, 233602 (2017).

[195] R. Johne, N. A. Gippius, G. Pavlovic, D. D. Solnyshkov, I. A. Shelykh, and G. Malpuech, "Entangled photon pairs produced by a quantum dot strongly coupled to a microcavity", Phys. Rev. Lett. **100**, 240404 (2008).

[196] F. Findeis, A. Zrenner, G. Böhm, and G. Abstreiter, "Phonon-assisted biexciton generation in a single quantum dot", Phys. Rev. B **61**, R10579 (2000).

[197] M. Glässl, A. M. Barth, and V. M. Axt, "Proposed robust and high-fidelity preparation of excitons and biexcitons in semiconductor quantum dots making active use of phonons", Phys. Rev. Lett. **110**, 147401 (2013).

[198] S.-Y. Zhu and X.-S. Li, "Quantum theory of a two-photon laser", Phys. Rev. A **36**, 3889 (1987).

[199] H. Huang, G.-x. Li, W.-j. Gu, and Z. Ficek, "Establishment of correlated states in a quantum dot interacting with an acoustic-phonon reservoir", Phys. Rev. A **90**, 023815 (2014).

[200] D. J. Gauthier, Q. Wu, S. E. Morin, and T. W. Mossberg, "Realization of a continuous-wave, two-photon optical laser", Phys. Rev. Lett. **68**, 464 (1992).

[201] E. del Valle, S. Zippilli, F. P. Laussy, A. Gonzalez-Tudela, G. Morigi, and C. Tejedor, "Two-photon lasing by a single quantum dot in a high-Q microcavity", Phys. Rev. B **81**, 035302 (2010).

[202] H. Singh, M. Das, and P. K. Pathak, "Continuous two-photon source using a single quantum dot in a photonic crystal cavity", Journal of Physics B: Atomic, Molecular and Optical Physics **53**, 155503 (2020).

[203] M. Brune, J. M. Raimond, P. Goy, L. Davidovich, and S. Haroche, "Realization of a two-photon maser oscillator", Phys. Rev. Lett. **59**, 1899 (1987).

[204] S. Y. Zhu and M. O. Scully, "Theoretical study of a two-photon double-beam laser", Phys. Rev. A **38**, 5433 (1988).

[205] H. Xiong, M. O. Scully, and M. S. Zubairy, "Correlated spontaneous emission laser as an entanglement amplifier", Phys. Rev. Lett. **94**, 023601 (2005).

[206] E. Schlottmann, M. von Helversen, H. A. M. Leymann, T. Lettau, F. Krüger, M. Schmidt, C. Schneider, M. Kamp, S. Höfling, J. Beyer, J. Wiersig, and S. Reitzenstein, "Exploring the photon-number distribution of bimodal microlasers with a transition edge sensor", Phys. Rev. Applied **9**, 064030 (2018).

[207] H. A. M. Leymann, A. Foerster, M. Khanbekyan, and J. Wiersig, "Strong photon bunching in a quantum-dot-based two-mode microcavity laser", physica status solidi (b) **250**, 1777 (2013).

[208] A. J. Ramsay, A. V. Gopal, E. M. Gauger, A. Nazir, B. W. Lovett, A. M. Fox, and M. S. Skolnick, "Damping of exciton rabi rotations by acoustic phonons in optically excited InGaAs/GaAs quantum dots", Phys. Rev. Lett. **104**, 017402 (2010).

[209] A. J. Ramsay, T. M. Godden, S. J. Boyle, E. M. Gauger, A. Nazir, B. W. Lovett, A. M. Fox, and M. S. Skolnick, "Phonon-induced rabi-frequency renormalization of optically driven single InGaAs/GaAs quantum dots", Phys. Rev. Lett. **105**, 177402 (2010).

[210] Y. Ota, S. Iwamoto, N. Kumagai, and Y. Arakawa, "Spontaneous two-photon emission from a single quantum dot", Phys. Rev. Lett. **107**, 233602 (2011).

[211] D. Walls and G. J. Milburn, *Quantum optics* (Springer, Berlin, Heidelberg, 2007).

[212] Y. Mu and C. M. Savage, "One-atom lasers", Phys. Rev. A **46**, 5944 (1992).

[213] M. Sargent, M. Scully, and W. Lamb, *Laser physics* (Addison-Wesley, 1974).

[214] J. K. Verma, H. Singh, P. K. Pathak, and S. Hughes, "Phonon-induced interactions and entanglement formation between two microcavity modes mediated by two semiconductor quantum dots", Phys. Rev. A **102**, 063701 (2020).

[215] P. D. Cunningham, A. T. Hanbicki, T. L. Reinecke, K. M. McCreary, and B. T. Jonker, "Resonant optical stark effect in monolayer ws2", Nature Communications **10**, 5539 (2019).

[216] S. Banerjee and K. A. Shore, "Biexcitonic blue stark shift in semiconductor quantum dots", Journal of Applied Physics **97**, 123101 (2005).

[217] S. Tesfa, "Entanglement amplification in a nondegenerate three-level cascade laser", Phys. Rev. A **74**, 043816 (2006).